



ISSN 1028-8546

Volume XXI, Number 2

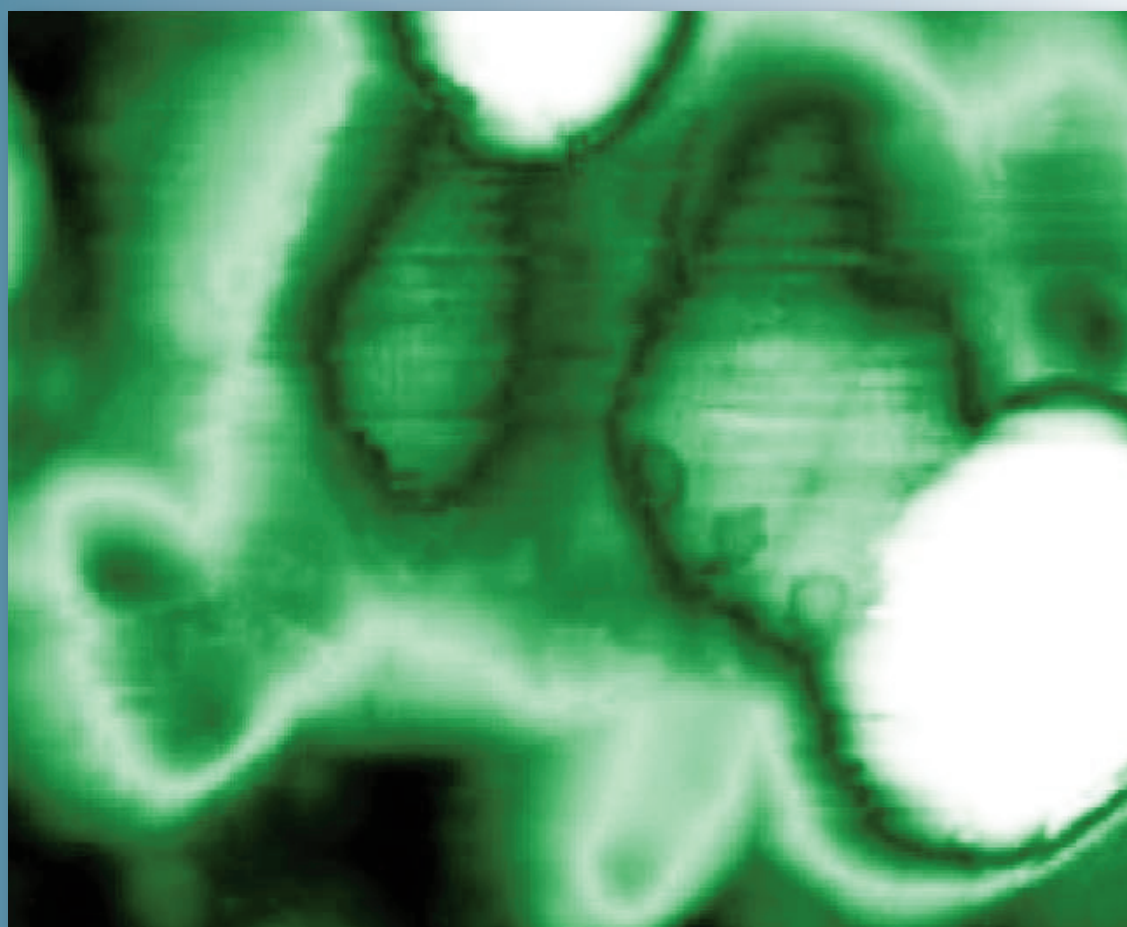
Section: En

July, 2015

Azerbaijan Journal of Physics

Fizika

www.physics.gov.az



G.M. Abdullayev Institute of Physics
Azerbaijan National Academy of Sciences
Department of Physical, Mathematical and Technical Sciences

Published from 1995
Ministry of Press and Information
of Azerbaijan Republic,
Registration number 402, 16.04.1997

ISSN 1028-8546
vol. XXI, Number 02, 2015
Series: En

Azerbaijan Journal of Physics

FIZIKA

*G.M.Abdullayev Institute of Physics
Azerbaijan National Academy of Sciences
Department of Physical, Mathematical and Technical Sciences*

HONORARY EDITORS

Arif PASHAYEV

EDITORS-IN-CHIEF

Nazim MAMEDOV

Chingiz QAJAR

SENIOR EDITOR

Talat MEHDIYEV

INTERNATIONAL REVIEW BOARD

Ivan Scherbakov, Russia
Kerim Allahverdiyev, Azerbaijan
Mehmet Öndr Yetiş, Turkey
Gennadii Jablonskii, Buelorussia
Rafael Imamov, Russia
Vladimir Man'ko, Russia
Eldar Salayev, Azerbaijan
Dieter Hochheimer, USA
Victor L'vov, Israel
Vyacheslav Tuzlukov, South Korea
Majid Ebrahim-Zadeh, Spain

Firudin Hashimzadeh, Azerbaijan
Anatoly Boreysho, Russia
Mikhail Khalin, Russia
Hasan Bidadi, Tebriz, East Azerbaijan, Iran
Natiq Atakishiyev, Mexico
Maksud Aliyev, Azerbaijan
Arif Hashimov, Azerbaijan
Vali Huseynov, Azerbaijan
Javad Abidinov, Azerbaijan
Bagadur Tagiyev, Azerbaijan

Tayar Djafarov, Azerbaijan
Talat Mehdiyev, Azerbaijan
Emil Guseynov, Azerbaijan
Ayaz Baramov, Azerbaijan
Tofiq Mammadov, Azerbaijan
Salima Mehdiyeva, Azerbaijan
Shakir Nagiyev, Azerbaijan
Rauf Guseynov, Azerbaijan
Almuk Abbasov, Azerbaijan
Yusif Asadov, Azerbaijan

TECHNICAL EDITORIAL BOARD

Senior secretary Elmira Akhundova, Nazli Guseynova, Sakina Aliyeva,
Nigar Akhundova, Elshana Aleskerova

PUBLISHING OFFICE

131 H.Javid ave, AZ-1143, Baku
ANAS, G.M.Abdullayev Institute of Physics

Tel.: (99412) 439-51-63, 439-32-23

Fax: (99412) 447-04-56

E-mail: jophphysics@gmail.com

Internet: www.physics.gov.az

It is authorized for printing:

Published at "SƏRQ-QƏRB"
17 Ashug Alessger str., Baku
Typographer : Aziz Gulaliyev

Sent for printing on: _____. 201_
Printing approved on: _____. 201_
Physical binding: _____
Number of copies: _____ 200
Order: _____

INFLUENCE OF HIGH PRESSURES ON ELECTRICAL AND THERMOELECTRIC PROPERTIES OF Cu-Ge-As-Se GLASSES

N.V. MELNIKOVA¹, A.Yu. MOLLAEV², O.L. KHEIFETS¹, L.A. SAYPULAEVA²,
P.P. HOHLACHEV², A.G. ALIBEKOV², A.L. FILIPPOV¹,
A.N. BABUSHKIN¹, K.V. KUROCHKA¹

Ural Federal University¹, Ekaterinburg 620000, Russia
*Amirkhanov Institute of physics of Dagestan Scientific centre of RAS²,
Makhachkala 367003, Russia*

e-mail: nvm.melnikova@gmail.com, ph: +79221105853, fax: +73432616885

We report the results on the high pressure effect (up to 50 GPa) upon the electrical resistivity, thermoelectric power, the tangent of dielectric loss angle and impedance of glassy chalcogenides (GeSe)_{1-x}(CuAsSe₂)_x.

Keywords: electrical resistivity, thermoelectric power, tangent of dielectric loss angle, chalcogenides

PACS: 61.10

INTRODUCTION

Multicomponent crystalline and amorphous materials of Cu-, Ag-, Ge-, In-, As-, Sb-based chalcogenides reveal interesting combination of electrical, optical, magnetic, mechanical, and other physical properties [1-10].

In particular, some of them as well the materials of Cu-Ge-As-Se system exhibit thermistor properties, some glasses display a memory switching, transit from a high impedance to low impedance state at high current densities and temperature increasing. Despite of variety of models proposed for a switching effect in chalcogenide glass semiconductors, a nature of these transitions is imperfectly understood [11, 12].

The aim of present work is the study of high pressure influence on electrical and thermoelectrical properties of (GeSe)_{1-x}(CuAsSe₂)_x materials and the evaluation the ability to control a transition from high impedance to low impedance state under high pressures. The ability of transition from high impedance to low impedance state and the changes in a structure under pressures up to 50 GPa are studied using the electrical resistance, the tangent of dielectric loss angle, complex impedance, thermoelectric force.

The work reports the experimental results obtained for two glassy materials: CuAsSe₂ ($x=1$) and (GeSe)_{0.05}(CuAsSe₂)_{0.95} ($x=0.95$).

1. Materials: synthesis, structure, and properties at atmospheric pressure

Glass materials were synthesized by the melt-quench from $T=800\text{K}$. Original components (at least of ACS quality) were alloyed in silica containers evacuated up to 10^{-4} Pa and filled with ultrapure argon to 0.5×10^5 Pa. The synthesized compounds were tested on Shimadzu XRD 6000 and Shimadzu XRD 7000 diffractometers and scanning electron microscopes. The materials were studied using the confocal Raman spectroscopy and atomic force microscopy Alpha300R (Witec). The diode-pumped solid-state laser of wavelength 488 nm and He-Ne laser of wavelength 633 nm served as the coherent light source. The density of samples was measured using helium pycnometer AccuPyc II 1340 (Micromeritics) providing high-accuracy estimation of a true solid density. Vickers microhardness tests was carried out with HVS-1000A Micro Hardness Tester which is equipped with automatic turret and digital display. It has been established that atomic structure of glasses is specified by a short-range order peculiar to crystalline compound CuAsSe₂. The powder diffraction patterns of studied materials (with $\text{CuK}\alpha$ monochromatic radiation) exhibit a few halos (Fig.1) typical to glassy materials of Cu-Ag-Ge-As-Se and Ag-Ge-As-S [13, 14]. The experimental atom radial distribution function of glasses (RDFA) was constructed by using the data on X-ray scattering in a wide angular range (Shimadzu XRD 7000, $\text{Cu-K}\alpha$, $8-140^\circ$ on 2θ).

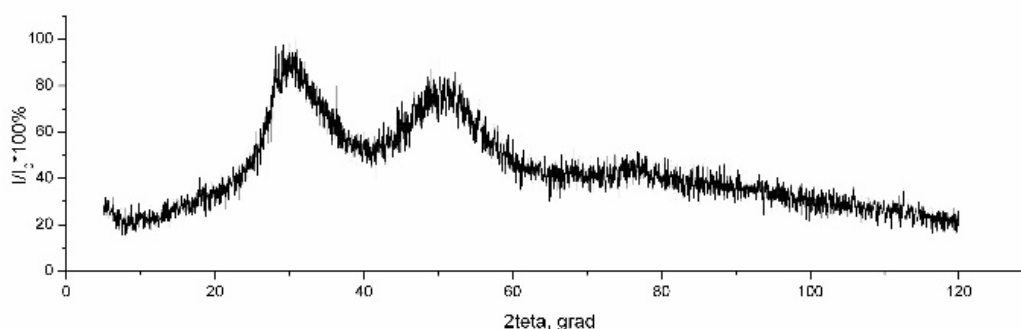


Fig. 1. Diffractogram of (GeSe)_{1-x}(CuAsSe₂)_x, $x=0.95$.

Fig. 2 presents the RDFA for $(\text{GeSe})_{1-x}(\text{CuAsSe}_2)_x$, $x=0.95$ plotted on experimental data and the RDFA for crystalline and glassy on the data derived from [15]. The radius of first coordination sphere estimated from the RDFA curve for glassy $(\text{GeSe})_{1-x}(\text{CuAsSe}_2)_x$, $x=0.95$ is ~ 2.4 Å. Interatomic bond distances of Cu and Se as well Cu and As contribute to the first coordination shell. Radius 2.4 Å corresponds to Poling sum radii of Cu and Se. The radius of a second shell 3.8 Å conforms to distances between Se-Cu-Se atoms in the bases of tetrahedrons. Since the crystalline $(\text{GeSe})_{1-x}(\text{CuAsSe}_2)_x$, $x=0.95$, as well as CuAsSe_2 has a cubic structure, based on the proximity of RDFA for both glasses we may suggest that glassy $(\text{GeSe})_{1-x}(\text{CuAsSe}_2)_x$, $x=0.95$, reveals the same structural 3-dimensional units conforming to crystalline CuAsSe_2 with sphalerite structure. These 3-dimensional units form the base of glassy CuAsSe_2 . Statistically Ge atoms may occupy the positions of As and Cu atoms in sphalerite-type structure. These data agree with data of work [15]. Thus, 3-dimensional unites of CuAsSe_2 the short-range ordering preserving within 1 nm make the lattice base of studied glasses. The short-range ordering is a distance in a coordination polyhedron (a local coordination of atoms). The packing of coordination polyhedral in various structures characterizes a medium-range order (4, 5, 6 coordination spheres). The Cu atoms in glassy CuAsSe_2 are ionized and an ionic formula $\text{Cu}^{1+}\text{As}^{3+}\text{Se}_2^{2-}$ is valid.

The analysis of Raman spectra (the confocal microscope Alpha300R, He-Ne laser of wavelength $\lambda = 633$ nm and power 30 mW) confirms that 3-dimensional units CuAsSe_2 make the atomic structure base of glassy $(\text{GeSe})_{1-x}(\text{CuAsSe}_2)_x$, $x=0.95$. Fig. 3 depicts the Raman spectrum of glassy $(\text{GeSe})_{1-x}(\text{CuAsSe}_2)_x$, $x=0.95$. The most intense band of the spectrum is in the range of $200 \text{ cm}^{-1} - 250 \text{ cm}^{-1}$. In this range, a maximum becomes well-marked at 230 cm^{-1} . Also the spectrum involves wide bands with a maximum at 140 cm^{-1} . Principal bands of chalcogenide spectra are broad under the influence of a phonon state density. Such a broadening is characteristic for amorphous materials and associated with a lack of a long-range order, the deformation of glass structural units in a disordered amorphous lattice.

In this case the short-range order is of importance in explaining the optical activity of modes. A Raman spectrum curve is failed to be clearly drawn in the sum of Gaussian curves, which conform to vibrations in potential interatomic bonds, because of a large number of potential vibrational modes contributing to the general spectrum and due to near values of atomic radii and atomic weights of Cu-Ge-As-Se system components. Nevertheless, we can point out some features of Raman spectrum for glassy system Cu-Ge-As-Se.

First, the mostly expressed peak in the Raman spectrum (that as well is observed for glassy materials As-Se and Cu-As-Se with slight Ge content) on a frequency of 230 cm^{-1} is associated with vibrations of As- and Se-atoms in tetrahedral unites $[\text{AsSe}_3]$ that characterizes the 3-dimensional structure of the glass. An As-atom is on a top of the tetrahedron; on other three tops are Se-atoms. The presence of this peak indicates to the predominance of As-Se bonds over others such as Cu-Se, Ge-As, and Ge-Se.

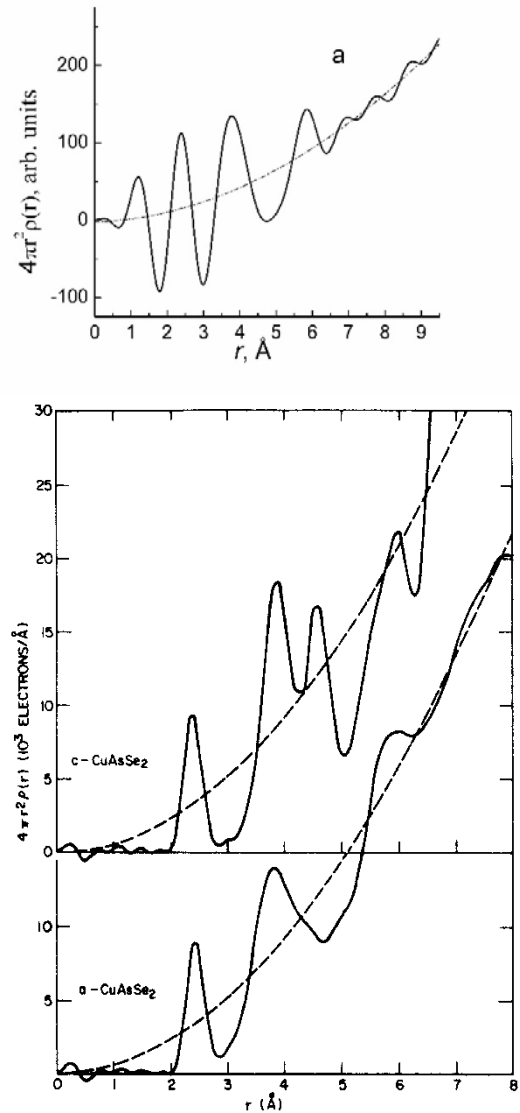


Fig. 2. Radial distribution function of atoms: a – for $(\text{GeSe})_{1-x}(\text{CuAsSe}_2)_x$, $x=0.95$ (derived in the present work); b – for crystalline CuAsSe_2 (up) and glassy CuAsSe_2 (down) (derived in work [15]).

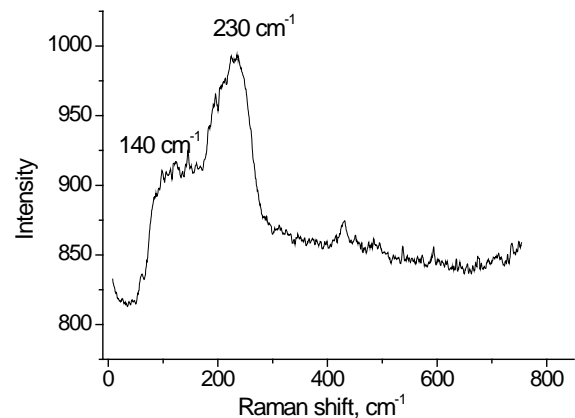


Fig. 3. Raman spectrum of glass material.

The wide band on frequencies 120-140 cm^{-1} is associated with the vibrations of Cu-Se and probably with Ge-As. All abovementioned is in agreement with our modeling of atomic structure of studied glasses. So, the analysis of data on X-ray diffraction, the radial distribution function, and the Raman spectra allows for the conclusion that 3-dimensional units of CuAsSe_2 form the base of the atomic structure for glassy CuAsSe_2 and $(\text{GeSe})_{1-x}(\text{CuAsSe}_2)_x$, $x=0.95$. Microhardness of $(\text{GeSe})_{1-x}(\text{CuAsSe}_2)_x$, $x=0.95$ sample is 185 HV at load of 0.1 kg and delay time corresponds to 1 second. The comparison of this value with the microhardness of glassy $\text{Cu-AsSe}_{1.5}$ [16] reveals that the existence of structural 3-dimensional units in such materials with more than 10-15 atomic percentage of Cu provides like values of the microhardness.

All materials researched under atmospheric pressure demonstrate semiconducting electrical properties at $T = (10-460) \text{ K}$. In CuAsSe_2 , a sharp increase in the conductivity and a transition from high impedance state (0.2 $\text{Ohm}\cdot\text{m}$) to low-impedance state ($3\cdot 10^{-5} \text{ Ohm}\cdot\text{m}$) with change of semiconducting conductivity to metallic occur when increasing the temperature above 460 K and rising the stress, $(\text{GeSe})_{0.05}(\text{CuAsSe}_2)_{0.95}$ attains thermistor properties. Still, a nature of transition switching effect in chalcogenides remains unexplored. One of reason for this effect is suggested to be the formation of a crystalline channel with low electrical resistivity by virtue of undergoing the reaction $3\text{CuAsSe}_2 \rightarrow \text{Cu}_3\text{AsSe}_4 + 2\text{AsSe}$ and the occurrence of low impedance crystalline phase Cu_3AsSe_4 . In glassy $(\text{GeSe})_{0.05}(\text{CuAsSe}_2)_{0.95}$, in which the base of glass network is of CuAsSe_2 3-dimensional units as well and Ge-atoms occupy the positions of Cu and As statistically, germanium prevents crystallization. And the effect of transition from low impedance to high impedance state, which was observed in CuAsSe_2 , changes to the thermistor behavior in material with Ge content, i.e. the glassy $(\text{GeSe})_{0.05}(\text{CuAsSe}_2)_{0.95}$ is heating without crystallization while passing the current through the sample, and the conductivity increases.

2. EXPERIMENTAL METHOD

Methods of research of material properties under high pressures

The direct-current measurements of the electrical resistivity of the samples was carried out in the toroid high-pressure apparatus in the range of 0-7 GPa at pressure rise and release. A detail description of the method was reported in works [17, 18]. The contacts to the surfaces of samples were indium-deposited. In order to achieve high pressures from 10 to 50 GPa, we used a high-pressure chamber (HPC) with rounded cone-plane diamond anvils. Artificial carbonado diamonds are good electrical conductors what allows the estimation of electrical properties of samples placed into the HPC [19-20]. To create the temperature gradient one of anvils was heated, the temperature of anvils at the points of contacts were measured by two copper thermocouples. Seebeck coefficient or absolute thermoelectric power S were calculated by measuring the potential difference (thermoelectric power) induced in the sample through copper branches

$$S = S_{Cu} + \frac{U_{12}}{T_1 - T_2}$$

where S_{Cu} is the copper absolute thermoelectric power (1.8 $\mu\text{V/K}$), U_{12} is the measured thermoelectric power, T_1 and T_2 are the temperatures of heated and cooled ends of the sample. The electrical properties in the range of pressures from 10 to 50 GPa were measured by the impedance spectroscopy technique using Solartron and RCL-2000 impedance meter-analyzer in the range of frequencies from 10 Hz to 1 MHz.

3. RESULTS AND DISCUSSION

The measurements of the electrical resistivity in $(\text{GeSe})_{0.05}(\text{CuAsSe}_2)_{0.95}$ in the dc field reveals a hysteresis (Fig.4). An increase in pressure from atmospheric to 6.4 GPa reduces the electrical resistivity by two orders and pressure drop recovers that to initial value.

In studied samples, the thermoelectric power is positive in a whole range of pressures and the conductivity is of p-type (Fig. 5). Thermoelectric power values are large which are typical for semiconductors (30 mV/K and 6 mV/K for $(\text{GeSe})_{0.05}(\text{CuAsSe}_2)_{0.95}$ and CuAsSe_2 , respectively). When pressure increasing from 12 to 50 GPa the thermoelectric power value reduces three-fold in CuAsSe_2 and twenty-folds in $(\text{GeSe})_{0.05}(\text{CuAsSe}_2)_{0.95}$, and respectively ten-folds and fifty times when pressure increasing from normal to 50 GPa. By reducing pressure from maximum (50 GPa) to atmospheric the thermoemf of studied chalcogenides varies slightly, and at normal pressure the thermoemf was of the order the same as at the maximum pressure. So the pressure processing of studied compounds can be considered as a technique to obtain the materials of high thermoelectric power value unalterable in a wide baric range from 10 to 50 GPa. The thermoelectric power in studied materials depends on the time during that the applied pressure operates. In the vicinity of some pressures, a character of the thermoelectric power-time dependence is different at pressure increase and decrease: the thermoelectric power rises with time under a pressure at a sample loading and increases under the same pressure after unloading.

The baric dependences for the thermoelectric power, real impedance, and the tangent of dielectric loss angle of $(\text{GeSe})_{0.05}(\text{CuAsSe}_2)_{0.95}$ (Fig.6) exhibit peculiarities of a behavior (a change in a decreasing or increasing rate of parameters and a local minimum on the thermoelectric power baric dependences for studied compounds) in one and the same pressure areas. Thermoelectric power values sharply decrease with an increase in pressure up to 27 GPa in glassy compound of $(\text{GeSe})_{0.05}(\text{CuAsSe}_2)_{0.95}$. A behavior of the tangent of dielectric loss angle and the electrical resistivity - the former slightly grows, the latter weakly reduces with a rise in pressure up to 27 GPa - testifies to glassy state to be preserved. With further increase in pressure the thermoelectric power dependence on pressure changes in the range of 27-30 GPa accompanied with a fast fall of the resistivity and rise of the dielectric dissipation factor.

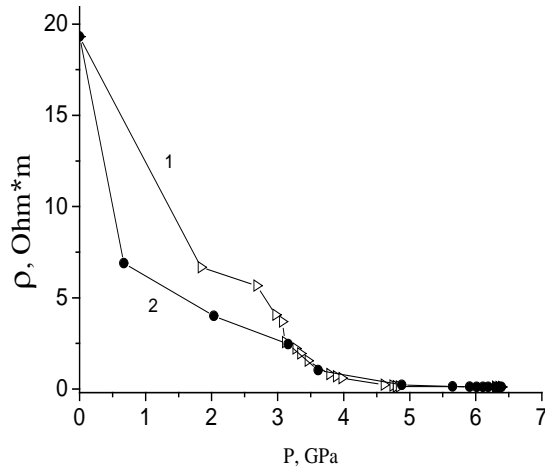


Fig. 4. Baric dependences of resistivity for glassy $(\text{GeSe})_{0.05}(\text{CuAsSe}_2)_{0.95}$ at pressure rise (curve 1) and drop (curve 2).

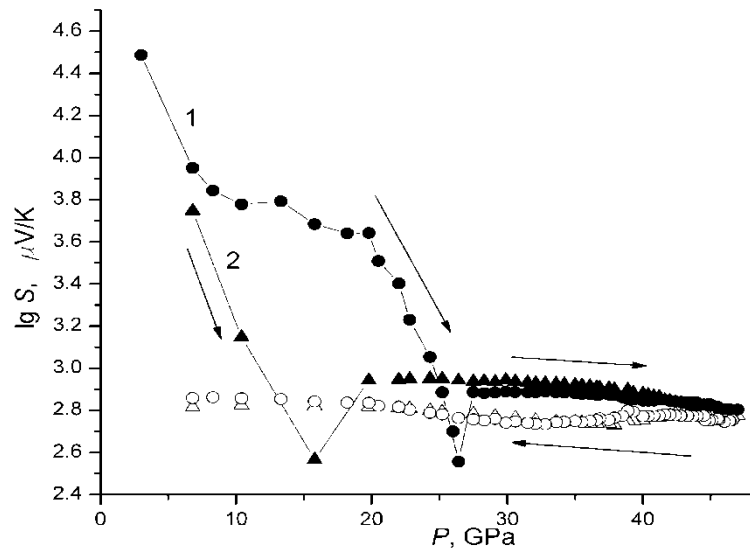


Fig. 5. Baric dependences of decimal logarithm of thermoelectric power in glassy $(\text{GeSe})_{0.05}(\text{CuAsSe}_2)_{0.95}$ (curve 1) and CuAsSe_2 (curve 2) at pressure increase (painted signs) and decrease (counter signs). Arrows indicate the direction of pressure variation.

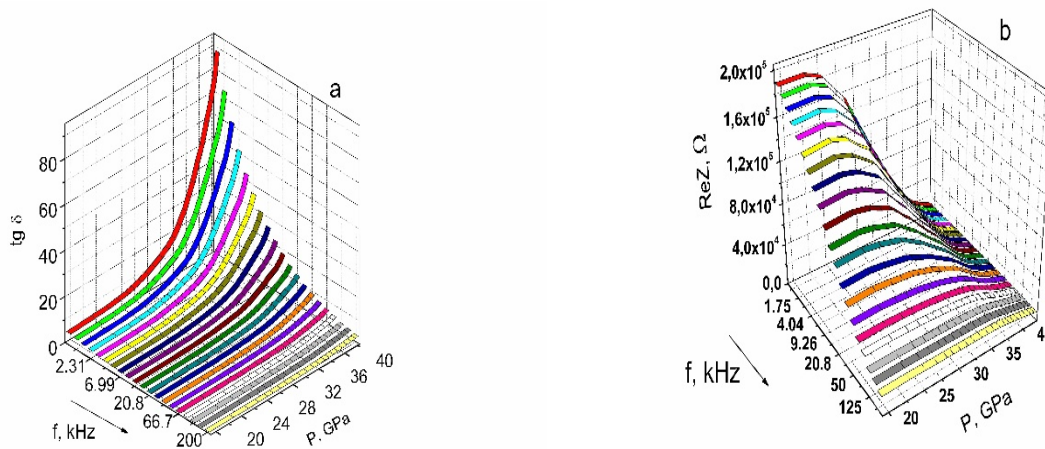


Fig. 6. Frequency-baric dependences of the tangent of dielectric loss angle (a) and real part of impedance (b) of glassy $(\text{GeSe})_{0.05}(\text{CuAsSe}_2)_{0.95}$.

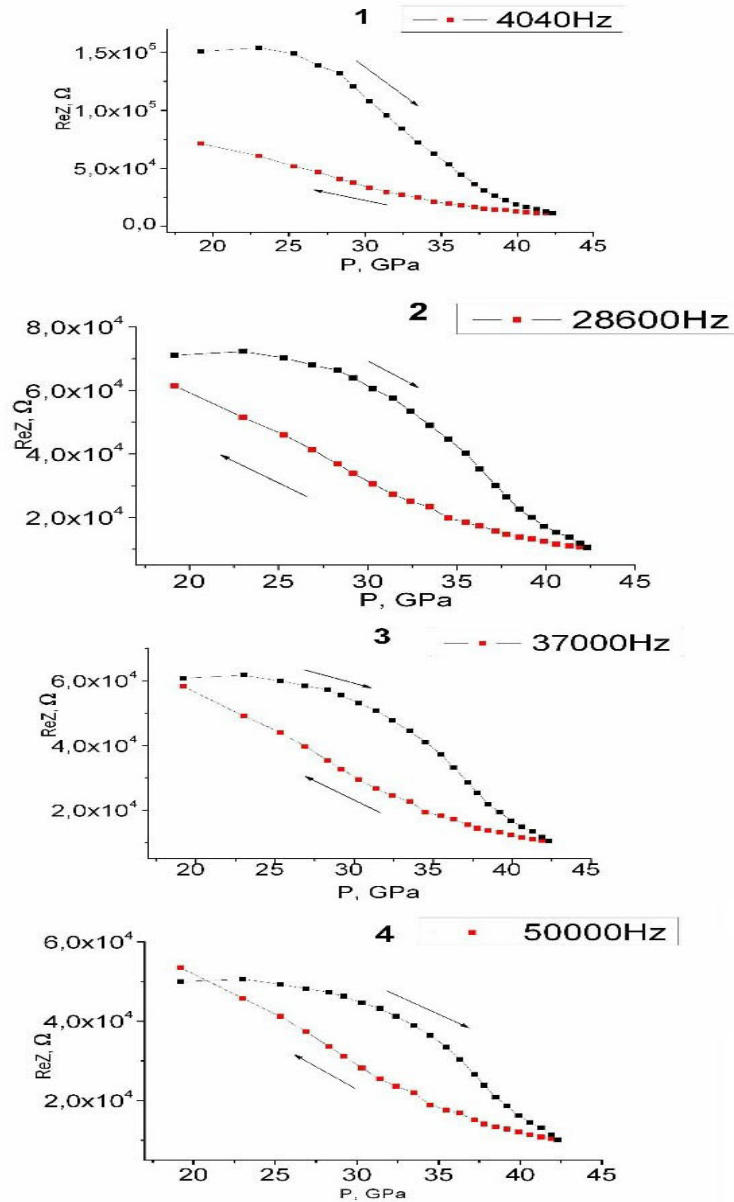


Fig.7. Baric dependencies of the real part of the impedance $(\text{GeSe})_{0.05}(\text{CuAsSe}_2)_{0.95}$ when pressure increases and decreases on different frequencies. Arrows indicate the direction of pressure variation.

The lower a frequency, the faster increase in the dielectric dissipation factor at lower pressures and the more influence of the active conductance and lesser of the reactive conductance. All curves corresponded to the measurements on constant frequencies are practically merge in the field of 38-47 GPa after decrease in the resistivity several-fold. Such a behavior of the resistivity with a rise in pressure on different frequencies can be explained by a change in parameters of glass units at packing, further increase in a number of carriers, and drop of activation energy.

The behavior of thermoelectric power with a pressure drop can be stemmed from the excess carriers of defects and impurities.

If the increase of pressure triggered the crystallization of explored glassy materials then, first of all, Cu_3AsSe_4 phase would stand out the resistivity of

which is several orders less than the resistivity observed in a whole range of pressures studied. In favor of crystallization failure speaks the fact that the alternating current measurements of electrical properties in a baric interval from 10 to 50 GPa reveal the hysteresis of electrical parameters with return to values measured before pressure increasing (Fig. 7).

4. CONCLUSION

In our investigation, we establish the pressure regions of strong changes in a behavior of the thermoelectric power and electrical properties of $(\text{GeSe})_{1-x}(\text{CuAsSe}_2)_x$ chalcogenides: about 19 GPa, about 36 GPa, and 43-44 GPa – in glassy CuAsSe_2 , about 27 GPa, and 38-43 GPa – in glassy $(\text{GeSe})_{0.05}(\text{CuAsSe}_2)_{0.95}$.

A decrease in the electrical resistivity by several orders with an increase in pressure up to 50 GPa and the return to an initial value indicate the changes in the electronic structure, increase of a number of carriers, variations of parameters of structural units of glass materials.

ACKNOWLEDGMENTS

The researches were supported in part by RFBR grants №13-02-00633-а и 13-02-96033 p_ural_a. Authors acknowledges UCCU “Modern Nanotechnology” for Raman spectra measurements.

- [1] *Keiji Tanaka, Koichi Shimakawa.* Amorphous Chalcogenide Semiconductors and Related Materials. Springer, 27.06.2011. 243 c.
- [2] *N. Melnikova, A. Mollaev, O. Kheifets, L. Saypulaeva, F. Gabibov, A. Alibekov, A. Babushkin, K. Kurochka.* AJP “Fizika”, 2010, 12, 42-45.
- [3] *E.R. Baranova, V.L. Kobelev, O.L. Kobeleva, N.V. Melnikova, V.B. Zlokazov, L.Ya. Kobelev, M.V. Perflyev.* Solid State Ionics, 1999. v.124, № 3-4, p. 255-261.
- [4] *O. Kheifets, L. Kobelev, N. Melnikova, L. Nugaeva.* Journal of Applied Physics, 2007, v. 77, № 1, p. 90-96.
- [5] *N.V. Melnikova, A.G. Alibekov, L.A. Saypulaeva, O.L. Kheifets, A.N. Babushkin, A.Yu. Mollaev, S.N. Kallaev, R.M. Ferzaliyev.* Phys. Solid State, 2011, v.53, №12, pp. 2352-2355.
- [6] *K.V. Kurochka, N.V. Melnikova, V.E. Zaikova, Ya.Yu. Volkova.* Study of temperature and pressure dependences of electric properties of amorphous Ag-Ge-As-S chalcogenides with content of carbon nanotubes. Institute of Physics (UK) AJP “Fizika”: Conference Series 2015, 586, 012011. p. 1-6.
- [7] *N.V. Melnikova, O.L. Kheifets, A.N. Babushkin, K.V. Kurochka.* Sensor electronics and microsystem technologies (SEMST), 2010, v.1, (7), №4, p. 52-56, 89-90.
- [8] *O. Kheifets, N. Melnikova, L. Saipulaeva, A. Alibekov, A. Mollaev, A. Babushkin, G. Tikhomirova.* High Pressure Research, v. 29, №2, June, 2009, p. 261-266.
- [9] *Nina Melnikova, Ahmedbek Mollaev, Olga Kheifets, Luiza Saypulaeva, Peter Hohlachev, Abdulabek Alibekov, Alexey Filippov, Alexey Babushkin and Kirill Kurochka.* AJP “Fizika”, 2010, №1,2, p.37-41.
- [10] *F.S. Gabibov, E.M. Zobov, L.A. Saypulaeva, A.G. Alibekov, N.V. Melnikova, O.L. Kheifets.* Phys. Solid State. 2015, v.57, №6. p. 1172-1176.
- [11] *I.A. Chaban.* Phys. Solid State. 2007. v.49, №3. p. 405.
- [12] *N.A. Bogoslovskiy, K.D. Candin.* Semiconductors. 2012, v.46, №5. p. 577.
- [13] *V.E. Zaikova, N.V. Melnikova, K.V. Kurochka, O.L. Kheifets.* Relaxation of conductivity in amorphous multi-component chalcogenides of copper and silver. Institute of Physics (UK) AJP “Fizika”, Conference Series. 2014, 541,012104, p. 1-4.
- [14] *K.V. Kurochka, N.V. Melnikova, I.S. Ustinova, Ya.Yu. Volkova and D.O. Alikin.* Electric properties of amorphous silver chalcogenides with content of carbon nanotubes at pressures up to 50 GPa. Institute of Physics (UK) AJP “Fizika”, Conference Series, 2014, v.500, Part 19, 192007. p. 1-6.
- [15] *K.S. Liang.* Structural studies of glassy CuAsSe₂ and Cu-As₂Se₃ alloys. 1974. v.10, №4. p. 1528-1538.
- [16] *I.A. Sokolov, Z.U. Borisova.* Glass phys. Chem., 1984, v.10, №1, p. 80-83.
- [17] *L.G. Khvostantsev, L.P. Vereshchagin, A.P. Novikov.* High Temperatures - High Pressures, 9(6), 637 (1977).
- [18] *A.Yu. Mollaev, L.A. Saypulaeva, R.K. Arslanov, S.F. Marenkin.* Inorg. Mater., 2001, 37(4), 405
- [19] *L.F. Vereshchagin, E.N. Yakovlev, B.V. Vinogradov, et al.* High Temperatures - High Pressures. 1974, 6, 499.
- [20] *G. K. Solanki, P. D. Patel M. K. Agarwal et al.* High Pressure Research. 2001, 21, 15.

Received: 11.02.2015

TEMPERATURE DEPENDENCES OF ELECTRIC CONDUCTION AND THERMO-EMF IN CuFeS_2 AND $(\text{CuFeS}_2)_{0.7}(\text{CuGaS}_2)_{0.3}$ SOLID SOLUTIONS

S.S. RAGIMOV¹, S.G. ASADULLAYEVA¹, T. Sh. IBRAGIMOVA¹, K.O. TAGIYEV²

Institute of Physics of Azerbaijan National Academy of Sciences¹,

AZ1143, G.Javid ave.,33,Baku, Azerbaijan

Baker Hughes Peregrine road, Westhill Business Park UK²

e-mail:sadiyar@mail.ru

e-mail:oktay58@mail.ru

The temperature dependences of electric conduction and thermo-emf of CuFeS_2 and solid solution $(\text{CuFeS}_2)_{0.7}(\text{CuGaS}_2)_{0.3}$ in temperature interval 80-320K are investigated. The jump correlating with temperature dependence of thermo-emf is observed in σ - $f(T)$ dependence at 125K in CuFeS_2 .

Keywords: solid solutions, thermo-emf, phase transition, electric conduction.

PACS: 61.66, 65.90.

INTRODUCTION

The development of semiconductor instrumentation technology requires the widening of compound class with given parameters allowing us to control their physical characteristics.

The semiconductor compounds with impurities of magnetic elements or compounds containing Mn, Fe at alias take the especial place. Such compounds are of interest for creation of functional elements on their base, which are controlled by magnetic field. That's why the comprehensive research of their physical properties is the one of the important tasks of solid state physics.

The measurement results of electric conduction and thermo-emf in interval 80-320K of polycrystalline samples CuFeS_2 and $(\text{CuFeS}_2)_{0.7}(\text{CuGaS}_2)_{0.3}$ are given in present work.

The investigations of structural properties CuFeS_2 [1] show that crystal lattice symmetry strongly depends on technology for its production. This compound crystallizes in several modifications:

1) cubic β -phase (lattice parameter $a=5.328\text{\AA}$) crystallizes in sphalerite structure. Besides cubic β -phase the compound CuFeS_2 crystallizes in two tetragonal structures with different sizes of elementary cell.

2) tetragonal α -phase has chalcopyrite structure and following lattice parameters ($a=5.292\text{\AA}$, $c=10.407\text{\AA}$). This phase is observed in stoichiometric compositions. Besides α -phase there is one more tetragonal γ -phase ($a=10.598\text{\AA}$ and $c=5.380\text{\AA}$). In this phase Cu and Fe atoms take ordered positions in cation sublattice.

In $\text{A}^{\text{I}}\text{B}^{\text{II}}\text{C}^{\text{VI}}$ compounds the forbidden band width changes in limits 0.8-3.5 eV. However, at replacement of trivalent cations in CuGaS_2 by Fe atom the obtained new compound becomes zero-gap semiconductor because additional d-band forms in forbidden one [2,3].

In CuFeS_2 at $T=50\text{K}$ the magnetic phase transition, which is connected with antiferromagnetic ordering of Cu atom magnetic moments, is revealed [4]. In the same temperature region the anomalies of temperature dependence of kinetic parameters are also revealed.

The magnetic and thermal properties of CuFeS_2 at low temperatures are investigated in [5]. The observable

anomalous increase of magnetic moment and magnetic susceptibility authors connect with formation of non-interacting magnetic clusters. The formation of such clusters is connected with disordering of Cu and Fe atoms in cation sublattice.

$(\text{CuFeS}_2)_{0.7}(\text{CuGaS}_2)_{0.3}$ is investigated with the aim to study the influence on electrophysical properties at replacement of Fe magnetic element by Ga one.

THE SYNTHESIS OF POLYCRYSTALLINE SAMPLES AND EXPERIMENT TECHNIQUE

CuFeS_2 polycrystalline samples are synthesized by melting of initial components Cu, Fe and S in stoichiometric ratio. The temperature is increased with rate 3K/min up to temperature, which exceeds the melting point of CuFeS_2 on 30-50K (1148 K) and then the isothermal endurance during 2 hours is carried out. After finishing of this procedure the cooling up to room temperature with rate 3-5K/min is carried out. The isothermal annealing is carried out at 1073K during 550 hours.

The investigations of temperature dependences of electric conduction and thermo-emf of CuFeS_2 and $(\text{CuFeS}_2)_{0.7}(\text{CuGaS}_2)_{0.3}$ in temperature interval 80-320K are carried out.

The measurements are carried out by four-point probe method on direct current. The thermo-emf is measured by method of stationary heat flow. The observable samples have parallelepiped form with $18 \times 2,5 \times 1,5\text{ mm}^3$ and $16 \times 2,3 \times 1,4\text{ mm}^3$ sizes. The heating furnace in the form of diminutive cooper reel with size $\Phi=1,5\text{mm}$ and height 2mm is glued by silver paste on sample butt. The thin constantan wire bifilarly wound on reel serves as heater. The temperature registration in interval 77-300K is carried out with the help of cuprum-constantan thermo-couple.

The thermo-couples are glued by silver paste on sample edge on distance 8mm from each other. The signal registration from thermo-couples is carried out with the help of voltage comparator that allows us to totally compensate the background emf.

The type of conductivity in both samples corresponds to electron one. The obtained experimental results are shown in fig.1 and fig. 2.

As it is seen from fig.1 for CuFeS_2 the electric conduction value in interval 80-125K increases with temperature increasing. Further, the strong decrease of electric conduction value in narrow temperature interval $\Delta T=5-6\text{K}$ in 6-7 times is observed around 125K. The electric conduction increases with further temperature increasing. These peculiarities (fig.2) are also observed on temperature dependences of thermo-emf and electric conduction of solid solution $(\text{CuFeS}_2)_{0.7}(\text{CuGaS}_2)_{0.3}$ at 125K. Such behavior of electric conduction and thermo-emf can be explained by two approaches:

1. existence of structural-phase transition in this compound in given temperature region;
2. existence of additional phase in main composition.

According to first approach, we can note as follows. The kinetic coefficients unevenly change at structural phase transition because of lattice parameter changes and band parameters correspondingly. The observed temperature dependences of kinetic coefficients σ and S confirm on phase transitions in these samples. It is followed to suppose that phase transition in CuFeS_2 takes place in temperature interval 120-125K. It is possible that it is connected with disordering of Cu and Fe atoms in CuFeS_2 cation sublattice.

By other hand we note that such dependences aren't observed on temperature dependences of CuFeS_2 at electric property investigations by other authors [6-8]. The different dependences of magnetic susceptibility inverse value on temperature dependence above and below $T=130\text{K}$ are observed in work [5]. The authors explains this peculiarity by revealing of cluster ferromagnetism at low temperatures. According to work [9] the peak at 120K is observed on temperature dependence of magnetic susceptibility. One can suppose that these changes are the result of magnetic structure changes of this material at this temperature. However, such strong influence of magnetic structure on electronic system is incredibly.

As it is seen from experimental data the decrease of S value correlating with of electric conduction value increasing is also observed on temperature dependence of thermo-emf in 100-150K interval. Further, the simultaneous growth of values both electric conduction and thermo-emf with temperature increasing can be explained by degeneracy elimination.

Investigation of Hall effect is carried out to find the reason of such behaviour of electric conduction and thermo-emf. These investigations show that at 80K Hall coefficient value corresponds to electron concentration of $4 \cdot 10^{16} \text{cm}^{-3}$ order. The strong magneto-field dependence at 80K (decrease of Hall coefficient value almost in 2 times) that confirms the high mobility of charge carriers. However, investigation of Hall coefficient around 300K for both compositions show the high value of charge carrier concentration of $2 \cdot 10^{20} \text{cm}^{-3}$ order. Such strong differences of concentration values at different temperatures, disagreement of sign of charge carriers obtained by Hall and thermo-emf measurements, the disagreement of temperature dependences of electric conduction and thermo-emf are observed in two-phase samples [10,11].

Indeed, it is difficult to imagine that charge carrier concentration increase on four orders in interval 200K. If it takes place then the other thermo-emf temperature dependence would observe.

Note that sulfur element including into observable sample compositions always make difficulties with obtaining of stable compositions [6,8]. It is probably, that especially this fact can lead to appearance of second phase.

Note, that if main and second phases have the different signs of charge carriers then the mutual compensation should take place and this affects on experimental data. However, the carried out roentgenostructural analyses don't reveal the tracks of any additional phases. Consequently, such temperature dependences are the result of structural phase transition in CuFeS_2 .

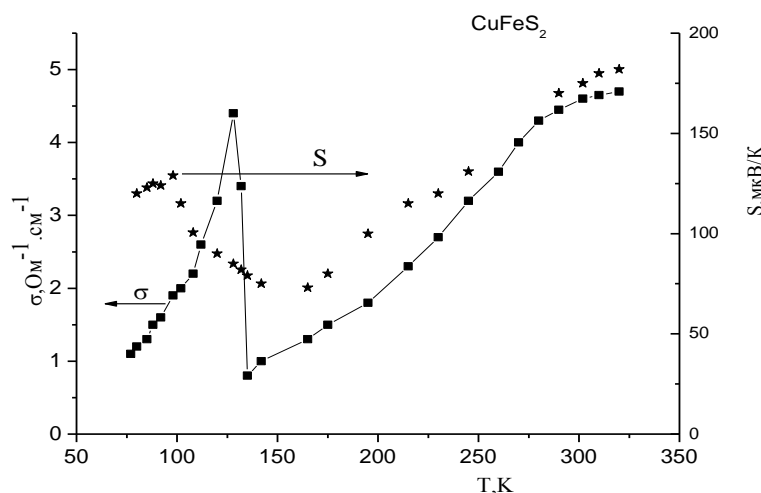


Fig.1. Temperature dependences of electric conduction and thermo-emf of CuFeS_2 .

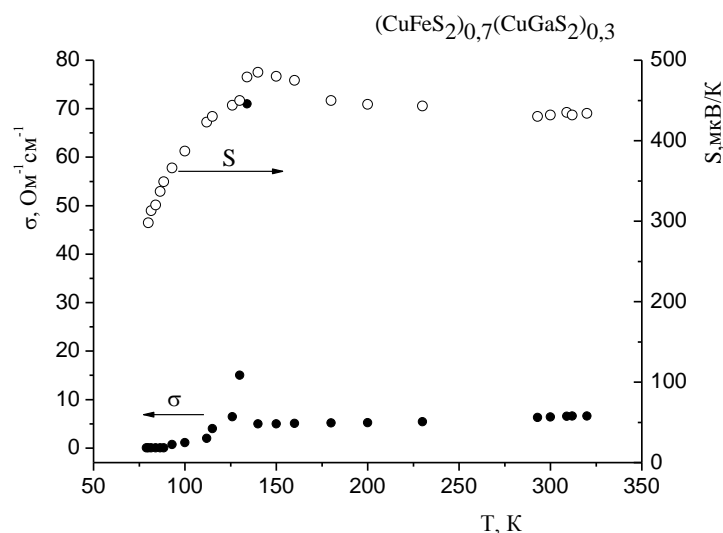


Fig.2. Temperature dependences of electric conduction and thermo-emf of $(\text{CuFeS}_2)_{0.7}(\text{CuGaS}_2)_{0.3}$.

CONCLUSION

The analysis of temperature dependences of electric conduction and thermo-emf and roentgen measurement

results allow us to conclude that CuFeS_2 and $(\text{CuFeS}_2)_{0.7}(\text{CuGaS}_2)_{0.3}$ solid solutions are two-phase systems.

-
- | | |
|--|---|
| [1] R. Adams, R. Beaulien, M. Vassiladis, A. Woid. Mater.Res.Bull, 1972, 7 ,87. | [6] V.V. Popov, P.P. Konstantinov, Yu.V. Rud. JETF 2011, 140 , 783. (In Russian). |
| [2] L.V. Kradinova, A.M. Polubotka, V.V. Popov, V.D. Prochuchan, Yu.V. Rud, V.K. Skoryutin. FTT, 1987, 29 , 2209. (In Russian). | [7] Naohito Tsujii and Takao Mori. J.Applied Physics Express, 2013, 6 , 043001. |
| [3] L.V. Kradinova, A.M. Polubotka, V.V. Popov, V.D. Prochuchan, V. Rud, V. Skorukin. Semicond. Sci. Technol. 1993, 8 , 1616,. | [8] T. Teranishi, K. Sato. J. Phys. (Paris) 36 , Coll. C3, Suppl. 1975, 9 , 149. |
| [4] Amarche, M. Quienero, J.R. Swalmason, T.M. Hobden. J. Magn. Mater. 1990, 162 , 347,. | [9] J. C. Woolley, A.-M. Lamarche, G. Lamarche at al. J. Magn. And Magn. Mater. 1996, 164 , 154 . |
| [5] V.V. Popov, S.A. Kijaev, Yu.V. Rud. FTT, 2011, 53 , 70. (In Russian). | [10] S.A. Aliev, S.S. Raqimov. Neorqanicheskie Materiali. 1992, 28 , 329. (In Russian). |
| | [11] C. Herring. J. of Applied Physics, 1960, 31 , 1939. |

Received: 25.02.2015

LEU-GALLATOSTATINE-3 NEUROPEPTIDE SPATIAL STRUCTURE

L.I. VELIYEVA, E.Z. ALIYEV

Baku State University

Lala_Veliyeva@rambler.ru

The space structure of *Leu*-gallatostatine-3 molecule is studied by theoretic conformational analysis method. The stability quantitative evaluation of possible molecule conformational states in dipolar medium conditions is carried out on the base of intramolecular conformational energy value.

Keywords: neuropeptides, structure, conformational analysis.

PACS: 87.80.-y

INTRODUCTION

The search and purposeful synthesis of compounds used for regulation of crop pest number is the one of actual problems in modern science. The neuropeptides synthesized by brain neurosecretory cells of insect different types, in particular, *Calliphora Vomitoria* are related to these compounds [1-3]. The neuropeptides inhibit the synthesis and extraction of juvenile hormones in ontogenesis insect process, take part in neurotransmission and regulation of nervous system functions. The study of mechanism molecular bases of their action and formation of effective analogues of these compounds with prolonged action effect is the important aspect in investigations of neuropeptides functional activity. The study of space structure and conformational properties of *Leu*-gallatostatine-3 is the aim of the present investigation. The neuropeptide chemical structure, designations of variable angles of rotation and calculation scheme of low-energy conformational states of gradually extensible tripeptide and pentapeptide fragments of molecule are given in fig.1 and fig.2.

CALCULATION RESULTS

*ALA*¹-*ASN*²-*ARG*³-*TYR*⁴ TETRAPEPTIDE.

N-end tetrapeptide molecule sequence includes 75 atoms and 23 dihedral angles, which are varied in main and side chains of amino-acid residuals. As the fragment consists of residuals with branched side chains having integer charges (*Asn*², *Arg*³) then the number of initial conformations chosen for minimization procedure of total conformational energy is 129. They belong to 8 shapes and 24 possible shapes of molecule valence chain. All permissible orientations of *Asn*², *Arg*³ side chains and *Tyr*⁴ aromatic ring in dependence on shape type are taken into consideration at variant construction. The conformation energy distribution of investigated fragments on shapes and contributions of interaction separate types into stabilization of most probable structures are given in tables 1 and 2.

From table 1 it is followed that conformations of *fff*, *ffe*, *efe*, *fef* four shapes with convoluted and half-convoluted shapes of fragment main chain are energetically preferable ones. They are stabilized by dispersion interactions of atoms of residual side chains *Asn*² and *Arg*³ non-bonded by valence (table 2).

*TYR*⁴-*GLY*⁵-*PHE*⁶-*GLY*⁷-*LEU*⁸-*NH*₂ PENTAPEPTIDE.

C-end pentapeptide fragment similar for all neuropeptides of allatostatine family includes the residuals *Tyr* and *Phe* with volume hydrophobic side chains, the interaction of which determine presuppositions for spatial organization formation of this region.

The number of permissible conformational states both the main and side chains of amino-acid residuals describing 16 fragment structural types is equal to 675. They are included in fragment potential energy minimization procedure the results of which are summarized in tables 3-4.

The conformation corresponding to energy global minimum of fragment (*E*_{rel.}=0.0 kcal/mol) is to structures with totally convoluted shape of main chain designated by *ffff* shape. The other conformations of this shape differ by *Tyr*, *Leu* side chain orientation and peptide frame shape of *Gly*⁵ glycine residual.

Leu-gallatostatine-3 molecule. The investigations of spatial structure of whole *Leu*-gallatostatine-3 molecule are carried out on the base of stable conformational states of *C*-end pentapeptide and *N*-end tetrapeptide overlapping by residual *Tyr*⁴. 530 structural variants covering all 82 permissible molecule shapes are constructed for total energy minimization procedure. The conformation distribution in *Leu*-gallatostatine-3 structure different types, the relative conformational energy of which doesn't exceed 5 kcal/mol, is given in fig.3. The results of calculated experiment including the conformational energy minimization procedure for representatives of all structure types are summarized in tables 5-6.

This allows us to classify the calculated conformations in correspondence with general elements of their spatial structures:

- 1) totally disordered structures (~ 20%)
- 2) structures with α -spiral *C*-end pentapeptide fragment and labile *N*-end tetrapeptide (~ 50%)
- 3) structures with two α -spiral regions connected by labile residual *Gly* in five position of linear consistency of amino-acid residuals (~30%).

The existence of a large number of disordered structures is caused by influence of surrounding water environment because of which the neuropeptides form the statistical ensembles of conformations comparable on stability divided by not high potential barriers in solution.

Ala-Asn-Arg-Tyr-Gly-Phe-Gly-Leu-NH₂

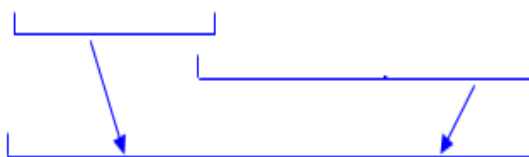


Fig.1. Calculation scheme of *Leu*-gallatostatine molecules.

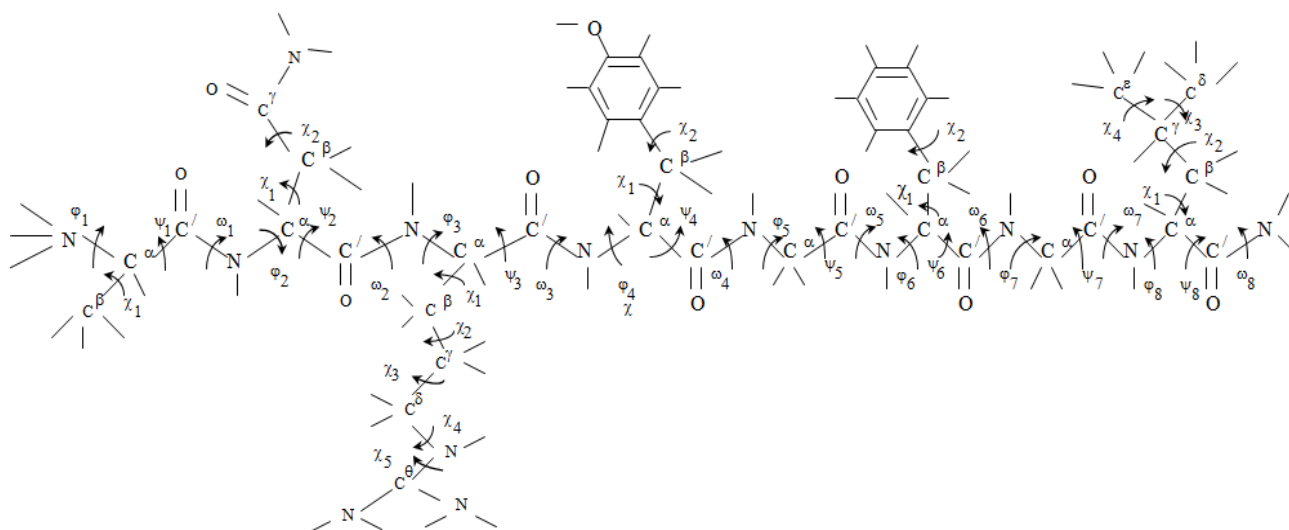


Fig.2. Calculated model of *Leu*-gallatostatine-3 molecule.

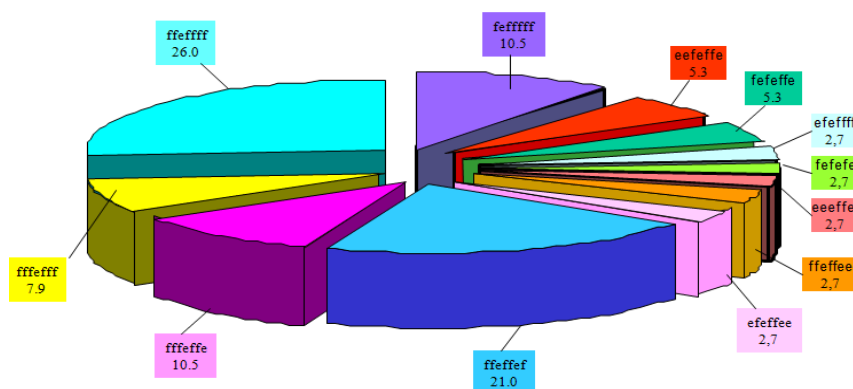


Fig.3. The percentage content of *Leu*-gallatostatine-3 molecule shape conformations ($E_{rel} = 0 \div 5$ kcal/mol)

Table 1. Conformation energy distribution (kcal/mol) on *N*-end tetrapeptide fragment of *Leu*-gallatostatine-3.

№	shape	Energy interval E_{rel} (kcal/mol)					
		0 ÷ 1	1÷2	2÷3	3÷4	4÷5	>5
1.	fff	-	1	6	1	1	1
2.	ffe	3	1	1	1	-	1
3.	fee	-	1	3	2	-	-
4.	eee	-	-	1	5	5	1
5.	eef	-	4	12	15	7	-
6.	eff	-	-	9	11	2	-
7.	efe	1	3	3	4	5	-
8.	fef	1	7	5	3	-	-

Table 2. Energy parameters of more optimal conformations of eight structural types of *N*-end tetrapeptide fragment of *Leu*-gallatostatine-3 neuropeptide

shape	Conformation	Energy contributions (kcal/mol)				
		E _{nv}	E _{el}	E _{tors}	E _{tot}	E _{rel}
fff	RR ₃₁ R ₂ B ₃	-16.14	2.79	0.75	-12.60	1.99
	RR ₃₂ R ₂ B ₁	-15.81	2.46	1.20	-12.15	2.44
ffe	RR ₂₂ B ₃ B ₁	-18.34	2.49	1.26	-14.59	0.00
	RR ₂₁ B ₃ B ₁	-17.77	2.37	1.38	-14.02	0.57
fee	RL ₃₁ B ₃ B ₁	-16.99	2.22	1.66	-13.10	1.49
	RB ₂₂ B ₃ R ₃	-15.66	2.17	1.13	-12.36	2.23
eee	BL ₃₁ B ₃ B ₁	-16.47	2.01	1.98	-12.48	2.11
eef	BB ₁₁ R ₂ B ₃	-16.09	2.16	0.73	-13.19	1.40
	LB ₁₁ R ₂ B ₃	-15.77	2.15	1.13	-12.49	2.10
eff	BR ₂₁ R ₂ B ₃	-15.30	2.21	0.78	-12.31	2.28
	BR ₁₁ R ₂ B ₃	-14.91	2.44	0.85	-11.62	2.97
efe	BR ₂₁ B ₃ B ₁	-16.61	1.97	1.01	-13.62	0.97
	L R ₂₁ B ₃ B ₁	-15.55	2.21	1.42	-11.92	2.67
fef	RB ₁₁ R ₂ B ₃	-17.01	2.14	0.88	-13.98	0.61
	RB ₁₁ RR ₃	-16.39	2.40	1.16	-12.83	1.76

Table 3. Energy distribution of optimal conformations of *N*-end tetrapeptide fragment of *Leu*-gallatostatine-3 molecule.

№	shape	Energy interval E _{rel} (kcal/mol)					
		0 ÷ 1	1 ÷ 2	2 ÷ 3	3 ÷ 4	4 ÷ 5	> 5
1.	effe	1	4	2	2	5	15
2.	ffff	6	5	5	9	5	15
3.	eeffe	-	6	5	8	6	40
4.	feffe	-	-	3	7	18	21
5.	fffe	-	2	7	15	17	34
6.	eeee	-	-	1	2	5	23
7.	feee	-	-	-	2	4	16
8.	ffee	-	-	-	8	9	25
9.	efee	-	-	5	8	3	5
10.	efff	-	-	-	1	1	12
11.	eeff	-	-	2	4	-	32
12.	feff	-	-	-	1	3	26
13.	feef	-	-	-	-	1	16
14.	eeef	-	-	2	2	-	20
15.	ffef	-	13	3	1	7	19
16.	efef	-	-	1	3	8	4

Table 4. Energy parameters of more optimal conformations of different structural types of *C*-end pentapeptide fragment of *Leu*-gallatostatine-3 molecule.

shape	Conformation	Energy contributions (kcal/mol)				
		E _{nv}	E _{el}	E _{tors}	E _{tot}	E _{rel}
ffff	B ₂ PR ₂ RR ₂₁	-23.68	4.42	2.16	-17.10	0.00
	R ₂ RB ₁ PB ₂₁	-23.20	3.87	2.24	-17.09	0.01
	B ₁ PB ₁ PB ₂₁	-23.01	4.34	2.33	-16.34	0.76
effe	B ₃ RB ₂ PR ₃₂	-22.18	2.15	3.25	-16.78	0.32
	B ₃ RB ₂ PR ₃₁	-21.80	2.18	3.72	-15.90	1.20
	R ₃ PR ₂ BB ₂₁	-20.91	2.53	3.10	-15.27	1.83
	R ₃ PB ₂ PR ₂₁	-20.88	2.49	3.20	-15.19	1.91
eeffe	B ₂ BB ₁ LB ₃₂	-21.54	3.59	2.36	-15.60	1.56
	R ₂ LB ₃ LB ₃₂	-21.40	4.09	1.96	-15.36	1.74
	R ₂ LR ₃ BR ₃₂	-20.75	4.02	1.41	-15.32	1.78
	B ₂ BB ₁ LR ₃₂	-21.27	3.74	2.26	-15.28	1.82
efef	R ₁ PR ₁ PR ₃₂	-20.43	3.34	2.14	-14.94	2.16
efee	R ₂ PB ₃ BR ₃₂	-21.46	3.62	2.14	-15.71	1.39
	R ₃ PR ₁ LR ₂₁	-20.75	3.77	1.72	-15.26	1.84
	R ₂ PR ₁ LB ₂₁	-20.01	3.45	2.50	-14.97	2.13
ffef	B ₁ PR ₁ PR ₂₁	-21.26	3.15	2.04	-16.07	1.03
	B ₂ PR ₁ PB ₂₁	-21.27	3.12	2.10	-16.05	1.05

LEU-GALLATOSTATINE-3 NEUROPEPTIDE SPACE STRUCTURE

Table 5. The low-energy conformations of *Leu*-gallatostatine-3 molecule.

shape	Conformation	Energy contributions (kcal/mol)				
		E _{nv}	E _{el}	E _{tors}	E _{tot}	E _{rel}
<i>ffeffef</i>	<i>RR₂₂B₃B₁PR₁PR₃₂</i>	-40.99	5.91	3.33	-31.75	0.00
	<i>RR₂₁B₃B₁PR₁PR₃₂</i>	-40.67	5.95	3.27	-31.44	0.31
	<i>RR₂₂B₃B₁PR₁PB₂₁</i>	-40.78	5.84	3.69	-31.26	0.49
	<i>RR₃₂B₃B₁PR₁PR₃₂</i>	-39.95	5.66	3.25	-31.04	0.71
<i>ffefffff</i>	<i>RR₁₁B₁B₃PR₂RR₂₁</i>	-39.88	5.89	2.99	-31.00	0.75
	<i>RR₁₁B₁B₃PR₂RR₃₂</i>	-40.63	6.06	3.72	-30.85	0.90
	<i>RR₁₁B₁B₃PB₂PB₃₂</i>	-39.56	5.76	2.97	-30.84	0.91
<i>fefffff</i>	<i>RB₁₁R₂B₃PB₂PB₂₁</i>	-39.55	5.44	2.66	-31.45	0.30
	<i>RB₂₁R₂B₃PR₂RR₂₁</i>	-39.66	5.72	2.99	-30.95	0.80
<i>fffefff</i>	<i>RR₁₁R₂R₃PB₂PB₃₂</i>	-42.41	6.20	5.12	-31.09	0.66
	<i>RR₁₁R₂R₃PB₂PB₃₁</i>	-42.56	6.29	5.51	-30.76	0.99
<i>feeffef</i>	<i>RL₃₁B₃B₁PR₁PR₃₂</i>	-39.34	5.89	4.05	-29.40	2.35
	<i>RL₃₁B₃B₁PR₁PB₂₁</i>	-37.86	5.77	3.89	-28.19	3.56
<i>efeffef</i>	<i>BR₂₁B₃B₁PR₁PB₃₂</i>	-37.27	5.54	3.15	-28.58	3.17
	<i>BR₂₁B₃B₁PR₁PR₃₂</i>	-36.64	5.47	3.06	-28.11	3.64

Table 6. Energy contributions (kcal/mol) of inter-and intra-residual interactions of *Leu*-gallatostatine-3 molecule.

<i>Ala</i>	<i>Asn</i>	<i>Arg</i>	<i>Tyr</i>	<i>Gly</i>	<i>Phe</i>	<i>Gly</i>	<i>Leu</i>	
1.06	-0.55	-0.62	-1.88	0.00	0.00	0.00	0.00	
1.07	-1.11	-0.25	-0.03	0.01	-0.04	0.00	-0.01	<i>Ala</i>
1.04	-1.18	-0.79	-0.47	-0.88	0.01	0.00	-0.07	
	-0.11	-2.51	-3.35	-0.02	-0.29	-0.38	-0.10	
	0.40	-1.63	-3.29	-0.48	-4.47	-0.19	-0.30	<i>Asn</i>
	-0.39	-1.00	-0.75	-0.23	0.00	0.00	0.01	
		0.30	-0.80	-0.22	-0.38	-2.21	-3.71	
		-0.09	-4.95	-0.20	-0.19	-0.03	-0.43	<i>Arg</i>
		0.07	-5.31	-0.43	-0.10	0.02	-0.16	
			-0.71	-1.28	-2.69	-2.63	0.07	
			0.00	-0.51	-1.15	-0.07	-4.51	<i>Tyr</i>
			-0.28	-0.48	-1.30	-0.12	-4.77	
				1.28	-1.11	-0.76	-0.02	
				1.22	-1.06	-0.39	-1.85	<i>Gly</i>
				1.18	0.89	-0.35	-0.73	
					0.30	-1.05	-3.31	
					0.00	-1.17	-1.83	<i>Phe</i>
					0.19	-1.33	-1.82	
						1.26	-1.54	
						1.30	-0.91	<i>Gly</i>
						1.29	-1.60	
							-0.75	
							-1.20	<i>Leu</i>
							-0.75	

***Note** The data for low-energy conformations of *ffeffef* ($E_{rel.} = 0.00$ kcal/mol), *fefffff* ($E_{rel.} = 0.30$ kcal/mol) and *fffefff* ($E_{rel.} = 0.66$ kcal/mol) shapes correspondingly are given in 1-3 lines.

The structures of other two types are stabilized mainly by intramolecular atomic interactions in limits di-, tri- and other types of inter-residual contacts (table 6).

Summarizing the investigation results one can conclude that there are two functionally important fragments of *Leu*-gallatostatine-3 neuropeptides. This is α -spiral pentapeptide realized in all energetically

preferable neuropeptides conformations and labile *N*-end fragment playing the hinge role for supplying of ligand molecule steric correspondence to its receptor.

The obtained results agree with data of numerous experimental investigations by the fact that glycine residual has the big flexibility and promotes to polypeptide chain swerving in compact structure.

- [1] *H. Duve, A.H. Johnsen, A.G. Scott, C.G. Yu, K.J. Yagi, S.S. Tobe, and A. Thorpe.* Proc.Natl.Acad. Sci. USA, 1993, **90**, 2456- 2460.
- [2] *H. Duve, A.H. Johnsen, J.L. Maestro, A.G. Scott, P.D. East, A. Thorpe.* Regul.Pept., 1996, **67**, 11-19.
- [3] *H. Duve, A. Thorpe.* Cell Tissue Res., 1994, **276**, 367-379.
- [4] *F.A. Momany, R.F. McGuire, A.W. Burgess, H.A. Scheraga.* J. Phys.Chem., 1975, **79**, 2361-2381.
- [5] *E.M. Popov.* The Structural Organization of Proteins Nauka, Moscow, 1989, 352 pp. (In Russian)
- [6] *IUPAC-IUB Commision on Biochemical Nomenclature Abbreviations and symbols for description of conformation of polypeptide chains (1974) Pure Appl. Chem., 40, 291-308.*

Received: 06.02.2015

HIGGS BOSON DECAY CHANNELS $H \rightarrow \gamma\gamma$, $H \rightarrow \gamma Z$, $H \rightarrow gg$

S.Q. ABDULLAYEV, M.S. GOJAYEV, F.A. SADDIGH

Baku State University, AZ-1148, Z.Khalilov, 23, Baku, Azerbaijan
s_abdullayev@mail.ru, m_qocayev@mail.ru, f_seddig@yahoo.com

In the framework of Standard Model the process of scalar Higgs boson decay channels $H \rightarrow \gamma\gamma$, $H \rightarrow \gamma Z$, $H \rightarrow gg$ are investigated. It is shown that the processes $H \rightarrow \gamma\gamma$ and $H \rightarrow \gamma Z$ suppressed than the process $H \rightarrow gg$.

Keywords: Standard Model, Higgs boson, left and right coupling constants, spirality, Weinberg's parameter.

Pacs: 12.15-y; 12.15. Mm; 14.70. Hp.

The Weinberg-Salam unified theory of Electromagnetic and weak interaction (Standard Model – SM) has achieved great success [1]. It includes the production of neutral weak current, discovery of W^\pm - and Z^0 -gauge bosons and some of its claims are investigated successfully in experiments. One of the important acclaims of SM is the prediction for the existence of scalar Higgs boson. Some experiments are carried out for the discovery of Higgs boson in different Experimental Labs.

Finally in LHC new information are received concerning the existence of Higgs boson with the mass of 125 GeV [2-5]. So the Higgs boson decay channels which give rise to Higgs bosons have got more attentions [6-9].

In this work we have investigated the channels of Higgs boson decaying to two gamma quanta, one gamma and one Z^0 -boson, and to two gluon:

$$H \rightarrow \gamma + \gamma, \quad (1)$$

$$H \rightarrow \gamma + Z^0, \quad (2)$$

$$H \rightarrow g + g. \quad (3)$$

1. Higgs Decay to Two Photons.

Since photons are massless particles, they do not couple to the Higgs boson directly. Nevertheless, the $H\gamma\gamma$ vertices can be generated at the quantum level with loops involving massive particles which couple to the Higgs boson. The $H\gamma\gamma$ couplings are mediated by charged fermions and W boson loops.

The Feynman for the Higgs boson decay to photons with fermions loops are shown in the Fig. 1 the 4-momentum of particles are shown over the diagram).

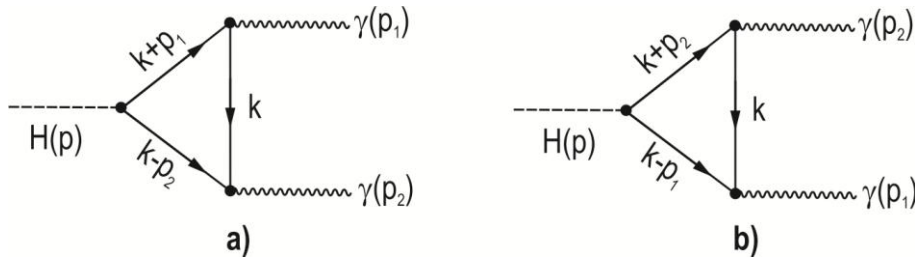


Fig. 1. The Feynman diagrams for the processes $H \rightarrow \gamma\gamma$

It is known that the interaction of Higgs boson with massive fermion is stronger, so we will calculate the diagram containing t-quark loop.

The matrix element for the first Feynman diagram could be written as follow:

$$M_a(H \Rightarrow \gamma\gamma) = -ie^2 Q^2 \frac{m}{\eta} a_\mu^{*(1)} a_\nu^{*(2)} \int \frac{d^4 k}{(2\pi)^4} \frac{\text{Tr}[\gamma_\mu (\hat{k} + \hat{p}_1 + m)(\hat{k} - \hat{p}_2 + m)\gamma_\nu (\hat{k} + m)]}{(k^2 - m^2)[(k + p_1)^2 - m^2][(k - p_2)^2 - m^2]}. \quad (4)$$

Here m and Q are the mass and charge of the fermion, $a_\mu^{*(1)}$ and $a_\nu^{*(2)}$ – are the 4-polarization vector of the fotons, $\eta = (\sqrt{2}G_F)^{-1/2} = 246 \text{ GeV}$ – is the vacuum expectation value of the Higgs boson field, G_F – signifies the Fermi constant of weak interaction.

For the sake of simplification of the matrix element, first we calculate the trace of Dirac matrices:

$$\begin{aligned} \text{tr}[\gamma_\mu (\hat{k} + \hat{p}_1 + m)(\hat{k} - \hat{p}_2 + m)\gamma_\nu (\hat{k} + m)] &= 4m\{g_{\mu\nu}[m^2 - k^2 - (p_1 \cdot p_2)] + \\ &+ 4k_\mu k_\nu - 2k_\mu p_{2\nu} + 2k_\nu p_{1\mu} - p_{1\mu} p_{2\nu} + p_{2\mu} p_{1\nu}\} \equiv 4mT_{\mu\nu}. \end{aligned} \quad (5)$$

Now by using Feynman integral techniques we calculate the integral in equation (4)

$$\frac{1}{ABC} = \int_0^1 dx \int_0^1 dy \int_0^1 dz \delta(x+y+z-1) \frac{2}{[Ax + By + Cz]^3}. \quad (6)$$

We have $A = k^2 - m^2$, $B = (k + p_1)^2 - m^2$ and $C = (k - p_2)^2 - m^2$ and we can simplify the denominator:

$$\begin{aligned} D = Ax + By + Cz &= (k^2 - m^2)x + [k^2 + 2(k \cdot p_1) - m^2]y + [k^2 - 2(k \cdot p_2) - m^2]z = \\ &= (k^2 - m^2)(x + y + z) + 2(k \cdot p_1)y - 2(k \cdot p_2)z = (k^2 - m^2) + 2(k \cdot p_1)y - 2(k \cdot p_2)z = \\ &= (k + p_1y - p_2z)^2 - m^2. \end{aligned} \quad (7)$$

We will consider here the case of $p_1^2 = p_2^2 = 0$ and $x + y + z = 1$. We define $b^2 = m^2 - 2(p_1 \cdot p_2)yz$, therefore, we can write D in the simplified form:

$$D = (k + p_1y - p_2z)^2 - b^2. \quad (8)$$

Following this we can show that the integral in (4) becomes:

$$I_{\mu\nu} \equiv \int \frac{d^4k}{(2\pi)^4} \int_0^1 dy \int_0^{1-y} dz \frac{8mT_{\mu\nu}}{[(k + p_1y - p_2z)^2 - b^2]^3}. \quad (9)$$

Let's change the variables under the integral by

$$k \Rightarrow k - p_1y + p_2z.$$

Then the integral (9) will be:

$$I_{\mu\nu} \equiv \int \frac{d^4k}{(2\pi)^4} \int_0^1 dy \int_0^{1-y} dz \frac{8mT'_{\mu\nu}}{(k^2 - b^2)^3}. \quad (10)$$

At this case tensor $T'_{\mu\nu}$ will be equal to:

$$\begin{aligned} T'_{\mu\nu} &\equiv g_{\mu\nu}(m^2 - (p_1 \cdot p_2)) - g_{\mu\nu}(k - p_1y + p_2z)^2 + 4(k - p_1y + p_2z)_\mu \times \\ &\times (k - p_1y + p_2z)_\nu - 2(k - p_1y + p_2z)_\mu p_{2\nu} + 2p_{1\mu}(k - p_1y + p_2z)_\nu - p_{1\mu}p_{2\nu} + p_{2\mu}p_{1\nu}. \end{aligned} \quad (11)$$

It should be noted that the terms are – linear in k vanish when integrated (k is an odd function). Besides this the polarization vector for gamma quanta fulfill the following condition:

$$a_{\mu}^{*(1)} p_{1\mu} = 0, \quad a_{\nu}^{*(2)} p_{2\nu} = 0.$$

As result the $T'_{\mu\nu}$ tensor will take a simpler forms:

$$T'_{\mu\nu} \equiv 4k_\mu k_\nu - k^2 g_{\mu\nu} + p_{2\mu} p_{1\nu} (1 - 4yz) + g_{\mu\nu} [m^2 - (p_1 \cdot p_2)(1 - 2yz)]. \quad (12)$$

Now by integrating over k we will get

$$\begin{aligned} \int \frac{d^4k}{(2\pi)^4} \cdot \frac{4k_\mu k_\nu - k^2 g_{\mu\nu}}{(k^2 - b^2)^3} &= \frac{i}{32\pi^2} g_{\mu\nu}, \\ \int \frac{d^4k}{(2\pi)^4} \cdot \frac{1}{(k^2 - b^2)^3} &= -\frac{i}{32\pi^2} \frac{1}{b^2}. \end{aligned} \quad (13)$$

So we will have the following formula for the $I_{\mu\nu}$ tensor:

$$I_{\mu\nu} = \frac{im}{4\pi^2} [p_{2\mu} p_{1\nu} - (p_1 \cdot p_2) g_{\mu\nu}] I, \quad (14)$$

Here I represents the following integral

$$I = \int_0^1 dy \int_0^{1-y} dz \frac{1-4yz}{2(p_1 \cdot p_2)yz - m^2} = \frac{1}{M_H^2} \int_0^1 dy \int_0^{1-y} dz \frac{1-4yz}{yz - m^2/M_H^2} = \frac{1}{M_H^2} \cdot I_0, \quad (15)$$

and we have considered that in the center of mass system $2(p_1 \cdot p_2) = M_H^2$.

Now we can write the matrix element for the Feynman diagram (a) as follow:

$$M_a(H \rightarrow \gamma\gamma) = \frac{e^2 Q^2}{4\pi^2} \cdot \frac{m^2}{\eta M_H^2} \cdot a_{\mu}^{*(1)} a_{\nu}^{*(2)} [p_{2\mu} p_{1\nu} - (p_1 \cdot p_2) g_{\mu\nu}] I_0. \quad (16)$$

Following the same rule we can calculate also the Feynman diagram (b). Calculations show that the amplitude of the b) diagram is exactly the same as the first one $M_a = M_b$. The total amplitude is given by:

$$M(H \rightarrow \gamma\gamma) = \frac{e^2 Q^2}{2\pi^2} \cdot \frac{m^2}{\eta M_H^2} [(a^{*(1)} \cdot p_2)(a^{*(2)} \cdot p_1) - (p_1 \cdot p_2)(a^{*(1)} \cdot a^{*(2)})] I_0. \quad (17)$$

Let's now calculate the square of matrix element for $H \rightarrow \gamma\gamma$.

$$\begin{aligned} |M(H \rightarrow \gamma\gamma)|^2 &= \left(\frac{e^2 Q^2}{2\pi^2} \right)^2 \cdot \left(\frac{m^2}{\eta M_H^2} \right)^2 \cdot |I_0|^2 [(a^{*(1)} \cdot p_2)(a^{*(2)} \cdot p_1) - (p_1 \cdot p_2)(a^{*(1)} \cdot a^{*(2)})] \times \\ &\quad \times [(a^{(1)} \cdot p_2)(a^{(2)} \cdot p_1) - (p_1 \cdot p_2)(a^{(1)} \cdot a^{(2)})]. \end{aligned} \quad (18)$$

The 4-polarization vector of gamma quanta with circular polarization $a = (0, \vec{a})$ could be written as follow:

$$\vec{a} = \frac{1}{2} (\vec{\beta} + il[\vec{n}\vec{\beta}]).$$

Here \vec{n} is the unit vector along the photon momentum, $\vec{\beta}$ is the unit vector perpendicular to photons momentum:

$\vec{\beta} \perp \vec{n}$ and $l = +1 (-1)$ signifies the right (left) polarization of the photon.

By integration with respect to phase volume in the center of mass frame we obtain the following expression for the total probability:

$$\Gamma(H \rightarrow \gamma\gamma) = \left(\frac{\alpha}{2\pi} \right)^2 \frac{Q^4}{64\pi M_H} \left(\frac{m^2}{\eta} \right)^2 |I_0|^2 (1 + l_1 \cdot l_2). \quad (19)$$

Here $l_1 = \pm 1$ and $l_2 = \pm 1$ – are the circular polarizations of photons. We can see from (19) that the gamma quanta should have right ($l_1 = l_2 = +1$) or left ($l_1 = l_2 = -1$) polarization.

The right polarization of one photon and left polarization of the other is being prohibited and this is due to the conservation of total momentum in the $H \rightarrow \gamma\gamma$

reaction.

After summing over the polarization states of photon, the probability for the $H \rightarrow \gamma\gamma$ reaction gets the following form:

$$\Gamma(H \Rightarrow \gamma\gamma) = \left(\frac{\alpha}{\pi} \right)^2 \frac{Q^4}{64\pi M_H} \left(\frac{m^2}{\eta} \right)^2 |I_0|^2. \quad (20)$$

2. Higgs Decay to photon and Z boson.

This process also fulfill two Feynman diagrams depicted in figure 2.

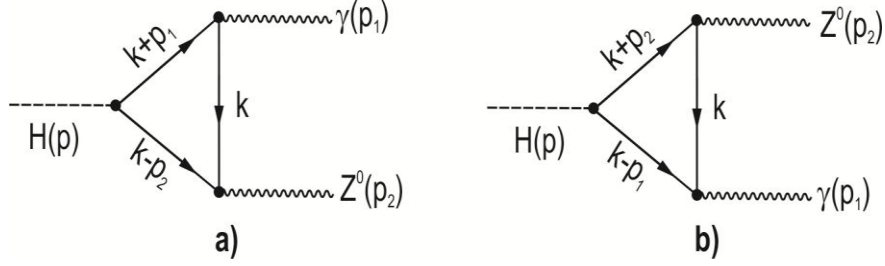


Fig. 2. Feynman diagrams for the process $H \Rightarrow \gamma Z^0$

Let's write first the matrix element for the Feynman diagram (a)

$$M_a(H \Rightarrow \gamma Z^0) = -ieQ \frac{m}{\eta} \frac{e}{2 \sin \theta_w \cos \theta_w} a_\mu^* U_\nu \times \\ \times \int \frac{d^4 k}{(2\pi)^4} \frac{\text{Tr}[\gamma_\mu (\hat{k} + \hat{p}_1 + m)(\hat{k} - \hat{p}_2 + m) \gamma_\nu [g_L(1 + \gamma_5) + g_R(1 - \gamma_5)](\hat{k} + m)]}{(k^2 - m^2)[(k + p_1)^2 - m^2][(k - p_2)^2 - m^2]}. \quad (21)$$

Here a_μ^* and U_ν are the 4-polarization vectors of photon and Z boson and

$$g_L = \frac{1}{2} - \frac{2}{3} \sin^2 \theta_w, \quad g_R = -\frac{2}{3} \sin^2 \theta_w \quad (22)$$

are the right and left coupling constants of t-quark to Z boson and θ_w is the Weinberg angle.

The trace of Dirac matrices will give:

$$\text{Tr}[\gamma_\mu (\hat{k} + \hat{p}_1 + m)(\hat{k} - \hat{p}_2 + m) \gamma_\nu [g_L(1 + \gamma_5) + g_R(1 - \gamma_5)](\hat{k} + m)] = 4m(g_L + g_R) \times \\ \times [g_{\mu\nu}(m^2 - k^2 - (p_1 \cdot p_2)) + 4k_\mu k_\nu - 2k_\mu p_{2\nu} + 2p_{1\mu} k_\nu - p_{1\mu} p_{2\nu} + p_{2\mu} p_{1\nu}] \equiv 4m(g_L + g_R) T_{\mu\nu}. \quad (23)$$

While calculating the last relation the anti-symmetric term due to the indices μ and ν have been omitted because by summing over the polarization states of the Z^0 boson and photon the resulted tensor is symmetric. Like the case of $H \rightarrow \gamma\gamma$ we get the following expression for the matrix element:

$$M(H \rightarrow \gamma Z^0) = -2ieQ \frac{m}{\eta} \frac{e}{2 \sin \theta_w \cos \theta_w} a_\mu^* U_\nu (g_L + g_R) I_{\mu\nu}. \quad (26)$$

Let's now find the square of the matrix element and sum over the polarization of particles:

$$\sum M(H \rightarrow \gamma Z^0) = -2ieQ \left(\frac{m^2}{\eta} \right)^2 \frac{e^2}{x_w(1-x_w)} (g_L + g_R)^2 (p_1 \cdot p_2)^2 |I|^2, \quad (27)$$

Here $x_w = \sin^2 \theta_w$ is the Weinberg parameter.

The total probability of the process $H \rightarrow \gamma Z$:

$$\Gamma(H \rightarrow \gamma Z^0) = \left(\frac{\alpha}{\pi} \right)^2 Q^4 \left(\frac{m^2}{\eta} \right)^2 \cdot \frac{(g_L + g_R)^2}{32\pi M_H x_w (1-x_w)} \cdot |I_0|^2. \quad (28)$$

It should be mentioned that diagrams for the processes $H \rightarrow \gamma\gamma$ and $H \rightarrow \gamma Z^0$ could be occurred by W-boson loops. The calculation for such diagrams will be considered in another work.

3. Higgs Decay to Two Gluons.

One of the other interesting decay channel for Higgs boson is the process of converting to two gluons. The diagrams for this are shown in fig. 4.

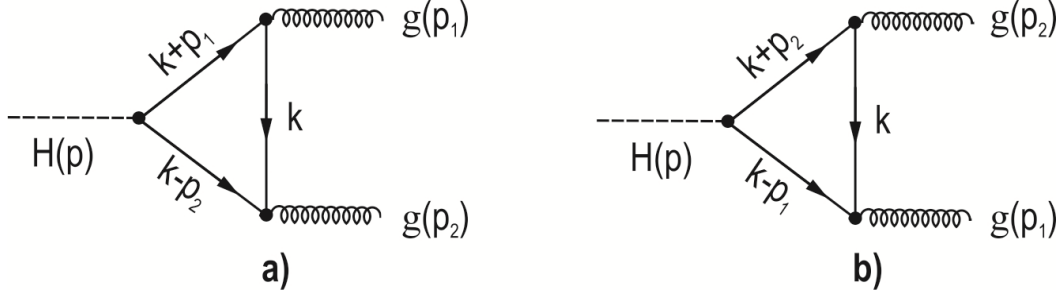


Fig. 3. Feynman diagrams for the process $H \rightarrow gg$.

Let's first write the matrix element for the diagram a:

$$M_a(H \rightarrow gg) = -ig_s^2 \frac{m}{\eta} \varepsilon_\mu^a \varepsilon_\nu^b \text{Tr} \left(\frac{\lambda_a}{2} \cdot \frac{\lambda_b}{2} \right) \int \frac{d^4 k}{(2\pi)^4} \frac{\text{tr}[\gamma_\mu (\hat{k} + \hat{p}_1 + m)(\hat{k} - \hat{p}_2 + m)\gamma_\nu (\hat{k} + m)]}{(k^2 - m^2)[(k + p_1)^2 - m^2][(k - p_2)^2 - m^2]}, \quad (29)$$

Here g_s is the constant for the quark-gluon interaction, ε_μ^a and ε_ν^b are the polarization vectors for gluons and λ_a are the Gell-Mann matrices.

We first find the trace of Gell-Mann matrices:

$$\text{Tr} \left(\frac{\lambda_a}{2} \cdot \frac{\lambda_b}{2} \right) = \frac{1}{4} \text{tr}(\lambda_a \lambda_b) = \frac{1}{2} \delta_{ab}.$$

Now we carry on the summation over the color and polarization of the gluons:

$$\sum_{a,b} \delta_{ab} \delta_{ab} = \sum_a \delta_{aa} = 8, \quad \sum_{pol} \varepsilon_\mu^a \varepsilon_\rho^{*a} \varepsilon_\nu^b \varepsilon_\sigma^{*b} = g_{\mu\rho} g_{\sigma\nu}. \quad (30)$$

Other calculations are carried like the case of the $H \rightarrow \gamma\gamma$. As result the square of the transition amplitude for the case of $H \rightarrow gg$ is:

$$\sum_{pol} |H \rightarrow gg|^2 = 4 \left(\frac{\alpha_s}{\pi} \right)^2 \left(\frac{m^2}{\eta} \right)^2 |I_0|^2. \quad (31)$$

Here $\alpha_s = \frac{g_s^2}{4\pi}$ is the constant for the strong interaction.

So, we find here the total probability of the decay of scalar Higgs boson to two gluons:

$$\Gamma(H \rightarrow gg) = \frac{1}{8\pi} \left(\frac{\alpha_s}{\pi} \right)^2 \left(\frac{m^2}{\eta} \right)^2 \frac{|I_0|^2}{M_H}. \quad (32)$$

Let's now compare the probability of the decay of Higgs boson to two gluon over the decay to two photons:

$$\frac{\Gamma(H \rightarrow gg)}{\Gamma(H \rightarrow \gamma\gamma)} = \left(\frac{\alpha_s}{\alpha} \right)^2 \cdot \frac{8}{Q^4}. \quad (33)$$

The electric charge for the t-quark is 2/3, according to last calculations when we take the value of $\alpha_s(M_z) = 0.114 \pm 0.0007$ for the strong interaction and $1/\alpha(M_z) = 127.916 \pm 0.015$ for the case of electromagnetic interaction the following value will be derived for the ratio of probability which is quite high:

$$\frac{\Gamma(H \rightarrow gg)}{\Gamma(H \rightarrow \gamma\gamma)} \approx 8600.$$

The real reason for this is the fact that the coupling constant for the strong interaction is much bigger (stronger) than electromagnet interaction ($\alpha_s \gg \alpha$).

- [1] *S.Q. Abdullayev*. Lepton-lepton və lepton-hadron qarşılıqlı təsirlərdə zəif cərəyan effektləri. I Hissə. Bakı, «AM965 MMC» nəşr., 2012, 482 səh.
- [2] ATLAS Collaboration. Observation of a new particle in the search for the Standard Model Higgs boson with the ATLAS detector at the LHC. *Phys. Lett.*, 2012, B716, p.1-29.
- [3] ATLAS Collaboration. Combined search for the Standard Model Higgs boson in pp collision at $\sqrt{s} = 7 \text{ TeV}$ with the ATLAS detector. *Phys. Rev.*, 2012, D86, 032003-1-31.
- [4] The CMS Collaboration. Observation of a new boson at a mass of 125 GeV with the CMS experiment at the LHC. 2012, arXiv 1207.7235.
- [5] The CMS collaboration Combined of searches for the Standard Model Higgs boson in pp collision at $\sqrt{s} = 7 \text{ TeV}$, 2012, arXiv: 1202.1488, v1.
- [6] *W.J. Marciano, C. Zhang, S. Willenbrock*. Higgs Decay to two photons. arXiv: 1109.5304 V2, 2011.
- [7] *M. Shifman, A. Vainshtein, M.B. Voloshin, V. Zakharov*. Higgs decay into two photons through the W-boson loop; arXiv: 1109.1785, v3, 2011.
- [8] *Da Huang, Tang Y. Wu*. Note on Higgs Decay into two photons $H \rightarrow \gamma\gamma$: 2012, arXiv: 1109.4846, v2.
- [9] *S.Q. Abdullayev, F.A. Saddigh*. Bakı Universitetinin Xəbərləri, fizika-riyaziyyat elmləri seriyası, 2014, №1, s.142-151.

Received: 24.12.2014

PHASE TRANSITION IN FERROMAGNETIC SUPERLATTICE NANOWIRES

V.A. TANRIVERDIYEV, V.S. TAGIYEV

*Institute of Physics of the National Academy of Sciences of Azerbaijan, Baku Az -1143,
Baku, H.Javid ave.33,*

E-mail: Vahid_tanriverdi@yahoo.com

The critical behavior of a superlattice nanowires consisting of two different ferromagnets is examined within the framework of the molecular-field theory approach. The transition temperature T_c for the nanowires which is modeled as having a hexagonal cross section are calculated as a function of inter-and intralayer exchange constant by the transfer matrix method. The results are illustrated numerically for a particular choice of parameters.

Keywords: A. Nanowires, superlattice, spin-waves, phase transition.

PACS: 75.70. Ak

INTRODUCTION

The interesting phenomena and practical benefits discovered in the magnetic materials with magnetic properties modulated in the nanometer scale have led to considerable attention [1-3]. In the recent past many experimental and theoretical research have been focused on the properties of magnetic systems in the nanometer scale [4-6]. With the advance of modern vacuum science, it is possible to artificially fabricate such structures.

Theoretically, various superlattice and nanowires can be modeled as having a chosen shape and size cross section (in the x-y plane) with a finite number spins arranged [7-9]. At comparison of bulk systems one can see that both superlattice and nanowires systems show novel magnetic and electronic features. The critical behavior of magnetic films and superlattice have been examined, either experimentally or theoretically [10-12]. On the other hand, considerable effort has been recently devoted to phase transition in nanowires [13,14].

MODEL AND FORMALISM

As indicated in fig. 1. we consider (l,r) hexagonal ferromagnetic superlattice nanowire (SLNW) model in which the l atomic layers of material a alternate with r atomic layers of material b , having exchange constant J_a and J_b in intralayer, and Y_a and Y_b in interlayer, respectively. On the other hand corresponding exchange constants between spins at the surface shell are J_{as} and J_{bs} in intralayer, and Y_{as} and Y_{bs} in interlayer, respectively. The exchange interactions between neighboring spins on two adjacent a and b materials are Y and Y_s . Lattice constant of the SLNW is $(l+r)a$.

The Ising Hamiltonian of the system can be written in the form

$$H = - \sum_{n,\tau,\tau'} J_{n,n}^{\tau,\tau'} (S_n^\tau S_n^{\tau'}) - \sum_{n,\tau} \left(Y_{n,n-1}^{\tau,\tau} (S_n^\tau S_{n-1}^\tau) + Y_{n,n+1}^{\tau,\tau} (S_n^\tau S_{n+1}^\tau) \right) \quad (1)$$

$$(\tau \neq \tau')$$

where the first term describes exchange interactions inside atomic layer, the second term describes exchange interactions between neighboring atomic layers. The external magnetic field is neglected for simplicity. Here, n is the index of atomic layer, τ describes the position of a

lattice site in this layer. The axis z of the coordinate system is along the nanowires under study.

According to the molecular-field model the mean spins $m_n^\tau = \langle S_n^\tau \rangle$ ($\tau = 1, 2, \dots, 7$) are determined by the set of equations

$$m_n^{(\tau)} = B_S \left[\left(\sum_{\tau'} J_{n,n}^{\tau,\tau'} m_n^{(\tau')} + Y_{n,n+1}^{\tau,\tau} m_{n+1}^{(\tau)} + Y_{n,n-1}^{\tau,\tau} m_{n-1}^{(\tau)} \right) / kT \right] \quad (2)$$

where k is Boltzmann constant, $B_S(x)$ is the Brillouin function

$$B_S(x) = \frac{2S+1}{2S} \coth \left(\frac{2S+1}{2S} x \right) - \frac{1}{2S} \coth \left(\frac{1}{2S} x \right) \quad (3)$$

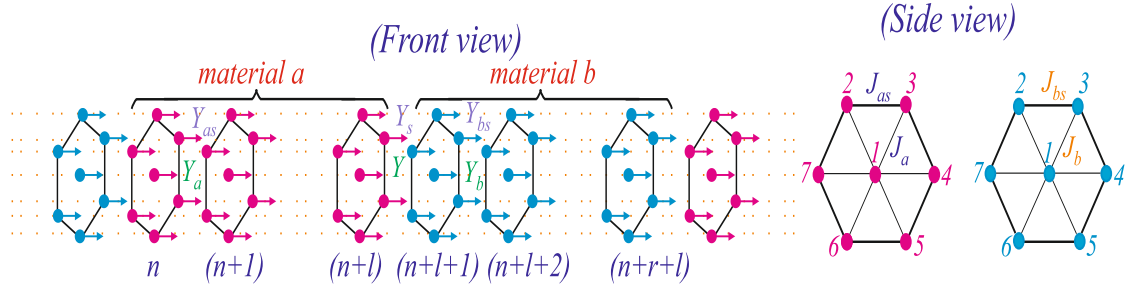


Fig.1. Model of hexagonal ferromagnetic nanowires in which the l atomic layers of material a alternate which r atomic layers of material b . The nanowires are infinite in the direction perpendicular to the axes z .

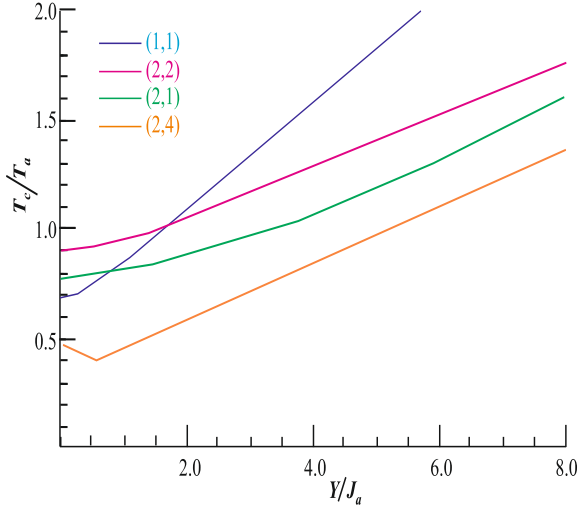


Fig.2. Critical temperatures as a function of Y/J_a for $J_{as}/J_a = 1$, $Y_a/J_a = 1$, $Y_{as}/J_a = 1$, $J_b/J_a = 1.5$, $J_{bs}/J_a = 1.5$, $Y_b/J_a = 1.5$, $Y_s/Y = 1$, $Y_{bs}/J_a = 1.5$.

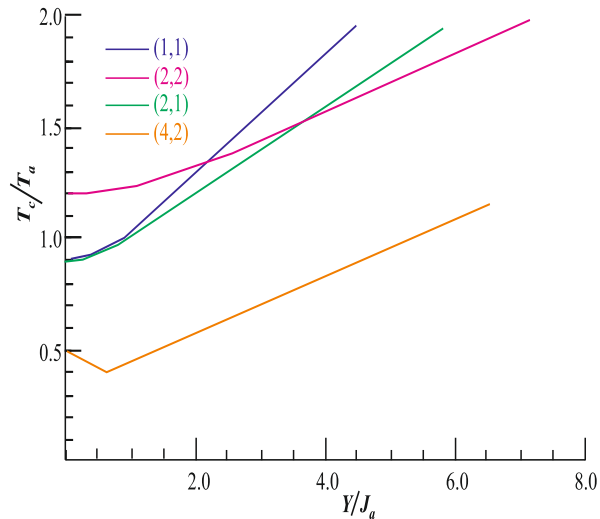


Fig.3. Critical temperatures as a function of Y/J_a for $J_{as}/J_a = 1.2$, $Y_a/J_a = 1$, $Y_{as}/J_a = 1.5$, $J_b/J_a = 2$, $J_{bs}/J_a = 2.2$, $Y_b/J_a = 1.8$, $Y_s/Y = 1.2$, $Y_{bs}/J_a = 2.1$.

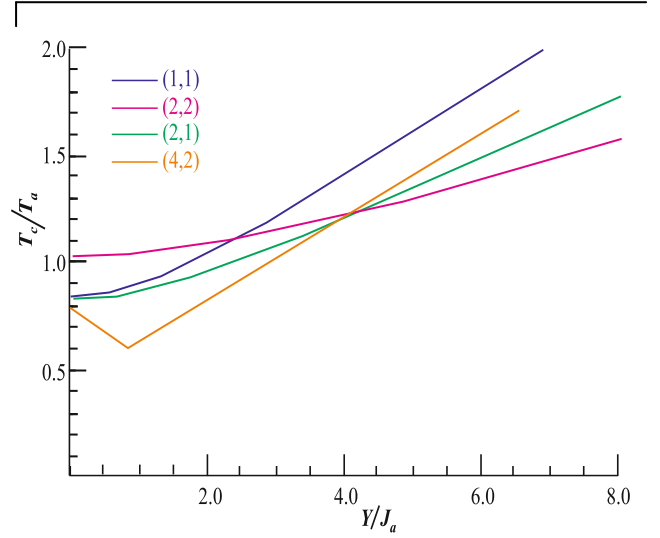


Fig.4. Critical temperatures as a function of Y/J_a for $J_{as}/J_a = 0.7$, $Y_a/J_a = 1.2$, $Y_{as}/J_a = 0.5$, $J_b/J_a = 2$, $J_{bs}/J_a = 1.5$, $Y_b/J_a = 1.8$, $Y_s/Y = 0.5$, $Y_{bs}/J_a = 1.3$.

As the temperature becomes higher than the critical temperature T_c the whole system becomes demagnetized and the mean atomic magnetization approaches zero. Near the critical temperature T_c mean spins m_n^r become small. For small arguments of Brillouin function all terms order higher than linear can be neglected, and one has the expansion:

$$B_S(x) \approx \frac{S+1}{3S} x \quad (4)$$

It is necessary to take into account that all six spins are in the same orientation according to the spin labeled by 1, therefore

$$m_n^{(2)} = m_n^{(3)} = m_n^{(4)} = m_n^{(5)} = m_n^{(6)} = m_n^{(7)}$$

in intralayer. Using (4) the system of equations (2) can be solved by recurrence relation technique [12] to relate the different spins at the first and second atomic layer of elementary unit cell

$$\begin{pmatrix} m_{n+l+2}^{(1)} \\ m_{n+l+2}^{(2)} \\ m_{n+l+1}^{(1)} \\ m_{n+l+1}^{(2)} \end{pmatrix} = D_{ab} D_a^{l-2} \begin{pmatrix} m_{n+1}^{(1)} \\ m_{n+1}^{(2)} \\ m_n^{(1)} \\ m_n^{(2)} \end{pmatrix} = R^{(a)} \begin{pmatrix} m_{n+1}^{(1)} \\ m_{n+1}^{(2)} \\ m_n^{(1)} \\ m_n^{(2)} \end{pmatrix} \quad (5)$$

the matrixes D_a and D_{ab} have the form:

$$D_a = \begin{pmatrix} d_a & -E \\ E & 0 \end{pmatrix}, \quad d_a = \begin{pmatrix} Tk_a/Y_a & -6J_a/Y_a \\ -J_a/Y_{as} & (Tk_a - 2J_{as})/Y_{as} \end{pmatrix}, \quad D_{ab} = \begin{pmatrix} d_{ab}^{(11)} & d_{ab}^{(12)} \\ d_{ab}^{(21)} & d_{ab}^{(22)} \end{pmatrix} \quad (6)$$

$$\begin{aligned} d_{ab}^{(11)} &= \begin{pmatrix} (6YJ_a J_b + Y_s(T^2 k_a k_b - Y^2))/YY_b Y_s & 6(YJ_b k_a T + Y_s J_a k_b T - 2YJ_{as} J_b)/YY_b Y_s \\ (YJ_a(2J_{bs} - k_b T) - Y_s J_b k_a T)/YY_{bs} Y_s & (Y(2J_{bs} - k_b T)(2J_{as} - k_a T) + 6J_a J_b Y_s - YY_s^2)/YY_{bs} Y_s \end{pmatrix}, \\ d_{ab}^{(12)} &= \begin{pmatrix} -Y_a k_b T/YY_b & 6Y_{as} J_b/Y_s Y_b \\ Y_a J_b/YY_{bs} & Y_{as}(2J_{bs} - k_b T)/Y_{bs} Y_s \end{pmatrix}, \quad d_{ab}^{(21)} = \begin{pmatrix} k_a T/Y & -6J_a/Y \\ -J_a/Y_s & (k_a T - 2J_{as})/Y_s \end{pmatrix}, \\ d_{ab}^{(22)} &= \begin{pmatrix} -Y_a/Y & 0 \\ 0 & -Y_{as}/Y_s \end{pmatrix} \end{aligned}$$

where $k_{a(b)} = 3kS_{a(b)}/(S_{a(b)} + 1)$ and E is two-dimensional unit matrix. The matrices D_a^{l-2} can be expressed by D_a using similarity transformation [15].

$$D_a^{l-2} = \begin{pmatrix} C_{l-2} & 0 \\ 0 & C_{l-2} \end{pmatrix} D_a - \begin{pmatrix} C_{l-3} & 0 \\ 0 & C_{l-3} \end{pmatrix} = \begin{pmatrix} C_{l-1} & -C_{l-2} \\ C_{l-2} & -C_{l-3} \end{pmatrix}. \quad (7)$$

$$C_n^{(a)} = u \begin{pmatrix} \alpha_n^{(1)} & 0 \\ 0 & \alpha_n^{(2)} \end{pmatrix} u^{-1}, \quad \alpha_n^{(j)} = \sin(n\theta_a^{(j)})/\sin(\theta_a^{(j)}), \quad j = 1, 2.$$

$$u_{11} = Y_{as}(2\cos\theta_a^{(2)} + k_a T/Y_a)/J_a, \quad u_{12} = Y_{as}(2\cos\theta_a^{(1)} + k_a T/Y_a)/J_a, \quad u_{21} = u_{22} = 1.$$

Here, $\theta_a^{(1)}$ and $\theta_a^{(2)}$ are defined from the following expression with the minus and plus sign, respectively.

$$2\cos\theta_a^{(1,2)} = \left[k_a T(Y_a + Y_{as}) - 2Y_a J_{as} \pm \sqrt{4Y_a Y_{as}(6J_a^2 - k_a T(k_a T - 2J_{as})) + ((k_a T - 2J_{as})Y_a + k_a T Y_{as})^2} \right] / 2Y_a Y_{as} \quad (8)$$

The 4x4 matrix $R^{(a)}$ is given by following expression

$$R_{11}^{(a)} = [6J_a(YJ_b \rho_{n-1} - k_b T Y_s \varphi_{n-1}) + 6YJ_b(\varphi_{n-1}(2J_{as} - k_a T) + Y_{as} \varphi_{n-2}) - Y_s(Y_a k_b T \rho_{n-2} + (Y^2 - k_a k_b T^2)\rho_{n-1})] / YY_b Y_s,$$

$$\begin{aligned} R_{21}^{(a)} &= [J_b Y_s(Y_a \rho_{n-2} - k_a T \rho_{n-1}) + Y((2J_{as} - k_a T)(2J_{bs} - k_b T) - Y_s^2)\varphi_{n-1} + YY_{as}(2J_{bs} - k_b T)\varphi_{n-2} + \\ &\quad + J_a(6J_b Y_s \varphi_{n-1} + Y(2J_{bs} - k_b T)\rho_{n-1})] / YY_{bs} Y_s, \end{aligned}$$

$$R_{31}^{(a)} = [k_a T \rho_{n-1} - Y_a \rho_{n-2} - 6J_a \varphi_{n-1}] / Y, \quad R_{41}^{(a)} = [(k_a T - 2J_{as})\varphi_{n-1} - J_a \rho_{n-1} - Y_{as} \varphi_{n-2}] / Y_s,$$

$$\begin{aligned}
 R_{12}^{(a)} &= R_{11}^{(a)} \{ \rho \rightarrow \gamma, \varphi \rightarrow \psi \}, & R_{13}^{(a)} &= -R_{11}^{(a)} \{ n \rightarrow n-1 \}, \\
 R_{14}^{(a)} &= -R_{11}^{(a)} \{ \rho \rightarrow \gamma, \varphi \rightarrow \psi, n \rightarrow n-1 \}, \\
 R_{22}^{(a)} &= R_{21}^{(a)} \{ \rho \rightarrow \gamma, \varphi \rightarrow \psi \}, & R_{23}^{(a)} &= -R_{21}^{(a)} \{ n \rightarrow n-1 \}, \\
 R_{24}^{(a)} &= -R_{21}^{(a)} \{ \rho \rightarrow \gamma, \varphi \rightarrow \psi, n \rightarrow n-1 \},
 \end{aligned}$$

Where

$$\begin{aligned}
 \rho_{n-1} &= (u_{11}\alpha_{n-1}^{(1)} - u_{12}\alpha_{n-1}^{(2)}) / (u_{11} - u_{12}), & \gamma_{n-1} &= Y_{as} u_{11} u_{12} (\alpha_{n-1}^{(2)} - \alpha_{n-1}^{(1)}) / J_a (u_{11} - u_{12}), \\
 \varphi_{n-1} &= J_a (\alpha_{n-1}^{(1)} - \alpha_{n-1}^{(2)}) / Y_{as} (u_{11} - u_{12}), & \psi_{n-1} &= (u_{11}\alpha_{n-1}^{(2)} - u_{12}\alpha_{n-1}^{(1)}) / (u_{11} - u_{12}).
 \end{aligned}$$

The matrices $R^{(a)}$ and $R^{(b)}$ combine to yield a transfer matrix $R = R^{(b)} R^{(a)}$, which relate spins of left hand first and second atomic layers of neighbor elementary unit cell:

$$\begin{pmatrix} m_{n+l+r+2}^{(1)} \\ m_{n+l+r+2}^{(2)} \\ m_{n+l+r+1}^{(1)} \\ m_{n+l+r+1}^{(2)} \end{pmatrix} = R \begin{pmatrix} m_{n+1}^{(1)} \\ m_{n+1}^{(2)} \\ m_n^{(1)} \\ m_n^{(2)} \end{pmatrix} \quad (9)$$

The matrix elements of $T^{(b)}$ are obtained from the elements of $T^{(a)}$ when $a \rightarrow b$ and $b \rightarrow a$. Note that determinant of the transfer matrix R is equal to unit.

There is a symmetry in the system under study, which allows us write $m_{n+l+r+2}^{(1,2)} = m_{n+1}^{(1,2)}$ and $m_{n+l+r+1}^{(1,2)} = m_n^{(1,2)}$. Then the following equation can be obtained to derive transition temperature

$$\text{Det}(R - E) = 0 \quad (10)$$

where E is 4x4 unit matrix.

RESULTS AND DISCUSSION

The formalism of transition temperature derivation obtained above is universal and can be used various number atomic layers of SLNW under study. In Fig.2- 4, we have shown the results for the (1,1), (2,1), (2,2) and (2,4) SLNWs. The transition temperature (in unit $T_a = 8J_a/k_a$) is plotted as function of Y/J_a . In Fig. 2, the curves, corresponding to all exchange constants for each material, are same. These are $J_a = J_{as} = Y_a = Y_{as}$, $J_b = J_{bs} = Y_b = Y_{bs}$, $J_b = 1.5J_a$ and $Y = Y_s$. When $Y/J_a < 1.5$, then critical temperature for all cases $T_c/T_a < 1$. Fig. 3 shows the curves when exchange constants between surface shell spins are smaller than between once and core spins. Fig. 4 shows the case when these are greater, respectively. Analysis shows that critical temperature increases with the layer number in one elementary unit cell increases and it decrease when the difference of numbers of atomic layers, belonging to deferent materials, increases.

-
- [1] V.S. Tkachenko, V.V. Kruglyak, A.N. Kuchko. Phys.Rev. B 81, (2010) 024425.
 - [2] A.L. Gonzalez, P. Landeros, Alvaro S. Nunez. Journal of Magnetism and Magnetic Materials 322, (2010) 530-535.
 - [3] Z.K. Wang, M. H. Kuok, S. C. Ng, D. J. Lockwood, M.G. Cottam, K. Nielsch, R.B. Wehrspohn and U. Gösele. Phys. Rev. Lett. v.89, n.2, (2002) 027201.
 - [4] O.A. Tretiakov and Ar. Abanov. Phys. Rev. Lett. 105, (2010) 157201.
 - [5] Ghaddar, F. Gloaguen, J. Gieraltowski. J. of Physics: Conference Series 200, (2010) 072032.
 - [6] H. Leblond, V. Veerakumar, M. Manna. Physical Review B 75, (2007) 214413.
 - [7] V.V. Kruglyak, R.J. Hicken, A.N. Kuchko, V.Yu. Gorobets. Journal of Applied Physics 98, (2005) 014304.
 - [8] T.M. Nguyen and M.G. Cottam. Phys.Rev. B 71, (2005) 094406.
 - [9] T.M. Nguyen and M.G. Cottam. Journal of Magnetism and Magnetic Materials 272-276, (2004) 1672.
 - [10] Y.M. Seidov and G.R. Shaulov. J.Phys.: Condens. Matter 6 (1994) 9621.
 - [11] T. Hai. Journal of Magnetism and Magnetic Materials 97, (1991) 227-234.
 - [12] Xiao-Guang Wang, Shao-Hua Pan, Guo-Zhen Yang. Solid State Commun. 113 (2000) 59-62.
 - [13] Hyun-Jung Kim and Jun-Hyung. Cho Phys. Rev. Lett. 110, (2013) 116801.
 - [14] Luis Sandoval and Herbert M Urbassek. Nanotechnology. 2009, v. 20, № 32, 325704.
 - [15] V.A. Tanriverdiyev, V.S. Tagiyev, S.M. Seyid-Rzaeva. Phys.Stat. Sol. (b) 2003, 240.

Received: 06.02.2015

ELECTRO-OPTIC CHARACTERISTICS OF LIQUID CRYSTALLINE MIXTURE H-37 DOPED BY FERROELECTRIC PARTICLES

T.D. IBRAGIMOV^a, A.R. IMAMALIYEV^a, G.M. BAYRAMOV^{a,b}

Institute of Physics of Azerbaijan National Academy of Sciences^a,

131 H.Javid Avenue, Baku, AZ1143, Azerbaijan, E-mail:tdibragimov@mail.ru

Baku State University^b. 23 Z.Khalilov Street, AZ1148. Baku, Azerbaijan

Influence of barium titanate particles on electro-optic properties of the nematic liquid crystalline (LC) mixture H-37 consisting of 4-methoxybenzylidene-4'-butylaniline and 4-ethoxybenzylidene-4'-butylaniline was investigated.

It was shown that the occurrence of barium titanate particles into H-37 decreases clearing temperature, increases the threshold of the Fredericksz effect and decreases the voltage of the electrohydrodynamic instability formation. A rise time increases and a decay time decreases in comparison with the pure H-37. First of all, experimental results are explained by appearance of local electric fields near the polarized ferroelectric particles at application of external electric field and also a change of viscosity and elastic properties of LC, existence of the additional obstacles (particles) by ions.

Keywords: liquid crystal, Fredericksz effect, electrohydrodynamic instability, small particles, barium titanate.

PACS: 42.70.Df; 47.20.Cn; 47.32.Cd; 61.30.Gd.

1. INTRODUCTION

One of directions of modern technology and physics of liquid crystals (LC) is development of hybrid systems, in particular, consisting of small particles embedded in a LC matrix. Even through at sufficient large particles (an order of wavelength of incident radiation) there is an optical effect of transmission of the system in a narrow spectral region, a maximum of which is shifted by action of electric field [1-5]. Besides, particles influence on electro-optical effects in LC, causing changes of their parameters [6-7].

It has been shown in the work [8] that there is no disturbance of the director of LC molecules if anchoring parameter of LC molecules with the particle surface is less than 1 and at their small concentration. This parameter depends on the particle sizes, elastic properties of LC, and also anchoring energy. At a certain combination of the specified parameters, the colloid behaves as a pure LC but with changed characteristics. Particularly, there is an increase of the order parameter of LC, reduction of clearing temperature [9], and also a decrease of threshold voltages.

There can appear additional effects if a particle substance is ferromagnetic or ferroelectric material. It was shown in one of the first works [10] that an additive of ferromagnetic particles in a LC matrix at small concentration leads to an increase of LC sensitivity to magnetic fields.

Authors of the work [11] obtained stable colloids based on of iron oxide particles in a liquid crystal 5CB and showed that their electro-optic properties slightly differed from the pure LC but possessed a property of a magnetic liquid. Recent years similar researches have started to be carry out with a system of ferroelectric particles in a LC.

It has been shown that at additive of ferroelectric particles increases dielectric response of LC and changes its conductivity [12-13], and also produces the photorefractive effect [14]. The memory effect in an isotropic phase of the liquid crystal 5CB doped by barium titanate particles was also observed [15].

One of the most used electro-optic effects in liquid crystal (LC) with negative dielectric anisotropy is electrohydrodynamic instability (EHDI). It is electric-induced phenomenon that is caused by the flow of a liquid crystal. Due to the flow distortion of the director alignment, the instability is usually accompanied by characteristic optical pattern. Among the instabilities in LC the most known are the Carr-Helfrich instability which is arises in a homogeneously oriented LC layer in a sandwich cell between transparent electrodes [16]. It is caused by a low-frequency electric field and occurs in the form of elongated vortices with their axis perpendicular to the original director alignment. The vortices cause a distortion of the director orientation, which is observed optically as a one-dimensional periodic pattern. They are called by Williams' domains.

In the present work, we have studied influence of embedded ferroelectric barium titanate particles on electro-optic characteristics of liquid crystalline mixture H-37 with negative dielectric anisotropy.

2. EXPERIMENTAL

We used liquid crystalline mixture consisting of 4-methoxybenzylidene-4'-butylaniline (MBBA) and 4-ethoxybenzylidene-4'-butylaniline (EBBA) with molar ratio of 1:1 (H-37) as a matrix. Selection of the present mixture is also based on following facts: a dielectric anisotropy is negative and conductive along the director is more than one perpendicular to the director for this LC. It was the opportunity for the EHDI study in nematic LC since the occurrence of field effects was excluded and it was only observed in planar sample of LC with negative dielectric anisotropy [8]. The monodisperse fraction of barium titanate particles with the average size of 600 nm was mixed with oleic acid and heptane in the ratio of 1:2:10 and ultrasonically dispersed for 1 hour. Then, the obtained mixture was added in the liquid crystal and kept at temperature 60 °C for 5 days till complete evaporation of heptane. The evaporation control of heptane was by weighing on analytic balance. The final composition was ultrasonically mixed. As a result, the colloid with weigh

percent 1% of particles was obtained. The image of the colloid under polarization microscope is represented in Fig.1.

The experiments were carried out in the electro-optic cell. The latter had a sandwich structure and consisted of two plane-parallel glass plates whose inner surfaces were coated with thin transparent and conductive layer ITO (Indium-Tin-Oxide). It was made from two glass substrates whose inner surfaces were coated with conducting indium-tin-oxide (ITO) layers. The cells' thickness was fixed with calibrated 17 μm polymer spacers. Either the colloid or the pure LC was filled into the cell by capillary action at isotropic state.

A setup for measurements of electro-optical parameters was assembled on the base of the polarization microscope of firm Carl Zeiss Jena. Impulses of the special form applied on the cell by the functional generator G6-28. A light passing through the cell fell on the photo diode and was registered by digital storage oscilloscope 6022BE of the firm HANTEK. Switching times and contrast were defined at application of unipolar rectangular impulses while threshold voltage was recorded using unipolar triangular impulses in quasi-static regime. Besides, value of threshold voltage was supervised under the polarization microscope. Frequency dependence of threshold voltage was registered at application of sinusoidal voltage. All measurements were carried out at temperature 21 $^{\circ}\text{C}$.

3. RESULTS

Results of measurements have shown that the used concentration of the additive of barium titanate particles inside the liquid crystal H-37 shifts the clearing point from 61.2 $^{\circ}\text{C}$ to 60.1 $^{\circ}\text{C}$.

Threshold voltage of Fredericksz effect increases from 2.8 V to up 3.1 V at addition of particles and remains practically constant up to the frequency of 700 kHz of the applied electric field then it drastically increases up to 3.4 V and 4.2 V near the frequency of 1 MHz for the pure LC and the colloid, accordingly (Fig. 1).

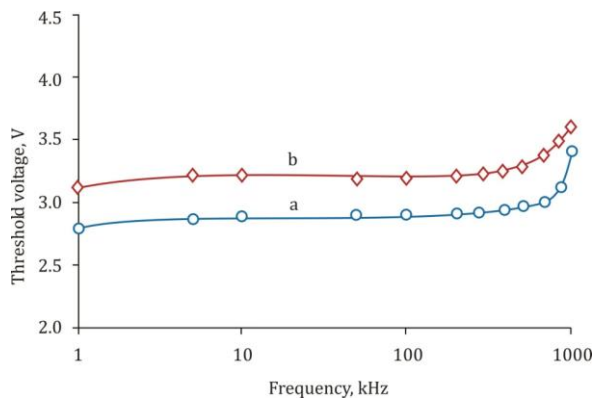


Fig.1. Frequency dependence of the threshold voltage of the Fredericksz effect: (a) pure H-37, (b) H-37 + BaTiO₃.

The threshold voltage of the Williams domain formation of the colloid equals to 3.7 V at application of quasi-static electric field while these domains begin to

form inside the cell with the pure LC at 6.3 V. Frequency dependence of threshold voltage of both pure H 37 and with an addition of particles is shown in Fig. 2.

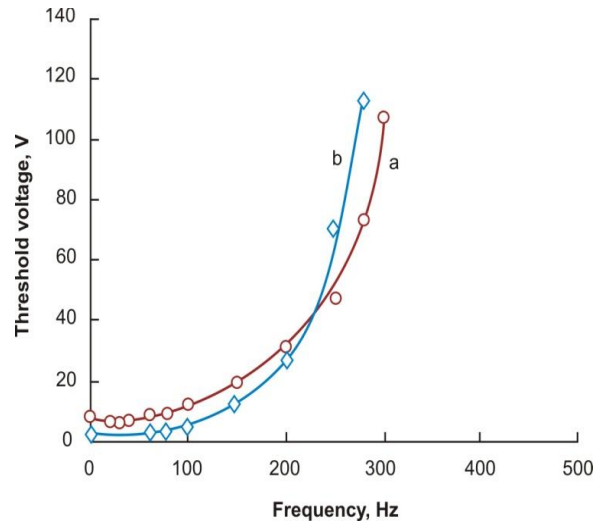


Fig.2. Frequency dependence of the threshold voltage of the Fredericksz effect: (a) pure H-37, (b) H-37 + BaTiO₃.

Indicated dependence is similar for both samples: with frequency increasing the threshold voltage increases and it aspires to infinity at some frequency, indicating on disappearance of the EHDI effect. The occurrence of barium titanate particles in LC reduces the threshold voltage of the EHDI formation in a quasi-static field and at low frequencies while it increases this threshold at high frequencies. At this case, we did not observe the disappearance of the instability in the colloid.

Time characteristics of the EHDI effect are resulted in Figs. 3 and 4.

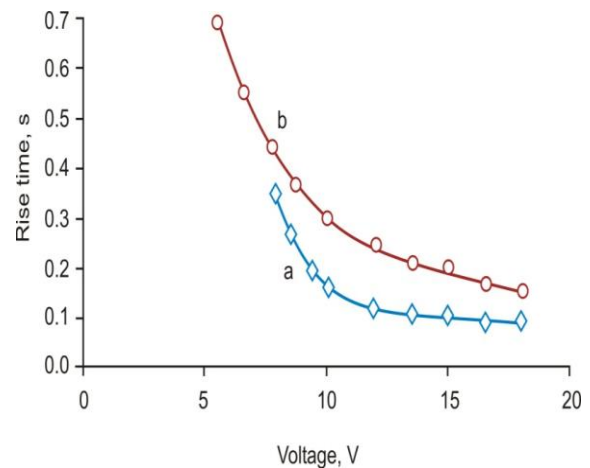


Fig.3. Dependence of rise time on quasi-static field voltage : (a) pure H-37, (b) H-37 + BaTiO₃.

Apparently, a rise time decreases with increasing of the applied voltage. An addition of particles into H-37 increases a rise time at all voltages. A decay time of the colloid less than for the pure LC at all applied voltages. At this case, a minimum is observed in corresponding dependence of the colloid at voltage 10 V. Observation under microscope shows chaotic motion of particles at this voltage.

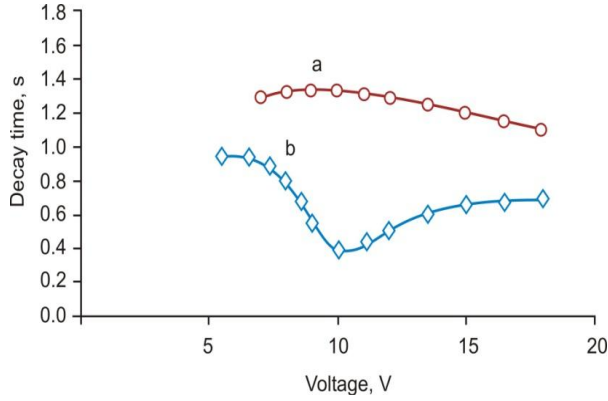


Fig.4. Dependence of decay time on quasi-static field voltage : (a) pure H-37, (b) H-37 + BaTiO₃.

Apparently, a rise time decreases with increasing of the applied voltage. An addition of particles into H-37 increases a rise time at all voltages. A decay time of the colloid less than for the pure LC at all applied voltages. At this case, a minimum is observed in corresponding dependence of the colloid at voltage 10 V. Observation under microscope shows chaotic motion of particles at this voltage.

4. DISCUSSION

According to [8], particles do not disturb the director of a LC, if the anchoring parameter $\zeta = WR/K_{11}$ is much smaller than 1, where W – anchoring energy of LC molecules with particle surfaces, $2R$ is particle size, K_{11} is the LC splay elastic constant. The values of anchoring energy is within 10^{-4} - 10^{-6} J/m², elastic constant of H-37 equals to $7.1 \cdot 10^{-12}$ N, and $2R$ has the size of 600 nm. Using oleic acid we reduce anchoring energy and simultaneously stabilize the colloid.

Besides, taking into account utilized concentration of particles, particle sizes, and particle density one can calculate that average distance between particles equal to 7.5 μ m which is about 10 times more than the particle sizes.

Thus, the overall disturbance of the director field by particles appears negligibly small. Hence, the obtained colloid can be considered as a homogeneous medium and it should behave as pure LC but with the modified parameters.

According to the calculations resulted in [17], at the spherical form and small concentration of particles, clearing temperature T_c of a colloid is defined by the formula

$$T_c = (1-f_v) T_{cp},$$

where f_v is volume concentration of particles, T_{cp} is clearing temperature of a pure LC.

Volume concentration of barium titanate particles equals to 0.002 but the total volume concentration of the filler inclusive of oleic acid amounts to 0.024. One can see, the calculations fairly well agree with the experimental value of clearing temperature.

At the sizes of particles greater than 100 nm with a lack of external electric field, the ferroelectric particles have a polydomain state [18], that is, there are the domains which polarization are oriented to various directions and fields of which compensate each other. Under the influence of external electric field inside the colloid, the dipole moments of domains are gradually established in the field direction. Herewith, they create around themselves the local electric field with a maximal value defined by the expression:

$$E = R^3 P_s / 3 \epsilon \epsilon_0 r^3.$$

here, $2R$ is particle size, P is spontaneous polarization, ϵ is dielectric permittivity of a LC, ϵ_0 is the electric constant, and r is distance from the center of a particle to the given point of the field. Considering the numerical values of the parameters ($R = 300$ nm, $P_s = 0.26$ C/m², $\epsilon \approx 10$, $\epsilon_0 = 8.85 \cdot 10^{-12}$ F/m) one can show, in particular, that the local field has of an order of 10^{10} V/m at the distance of 300 nm from a particle surface, which dramatically decreases in inverse proportion to a cube of distance from the particle center. This field orientates dipoles of LC molecules near the particles along electric-field lines. With further increase in the field intensity, the dipoles of particles together with the nearest LC molecules turn under the influence of the field in the aggregate.

Threshold voltage of the Fredericksz effect for a pure LC, and also a low-concentrated colloid is defined by expression [19]:

$$U_{th} = \pi (K_{33}/\epsilon_0 \Delta\epsilon)^{1/2},$$

where K_{33} is the bend elastic constant, ϵ_0 is the electric constant, $\Delta\epsilon$ is the dielectric anisotropy.

The larger value of threshold voltage of the colloid in comparison with the pure LC is connected with two competitive factors: presence of particles increasing the order parameter [18] and oleic molecules decreasing this parameter which affects on the dielectric anisotropy of the colloid. Most likely, the oleic acid molecules have more influence on the LC than particles.

Hence, the order parameter and, correspondingly, the dielectric anisotropy decrease. As a result, the threshold voltage increases.

There is a dispersion of $\epsilon_{||}$ at 750 kHz because of the LC molecules have no time to turn about a short axis at fast changes of the direction of the applied field while ϵ_{\perp} does not almost vary as it corresponds to turn of LC molecules around the long axis. Consequently, a dielectric anisotropy decreases and, accordingly, a threshold voltage increases.

The physical mechanism of the instabilities could be described as follows. A homogeneously oriented nematic LC is stabilized by the elastic torque due to anchoring of LC molecules with a substrate surface. Dielectric torque because of both external and space charge fields is stabilizing for LC with negative dielectric anisotropy. Owing to an electric field, the arising torque also is stabilizing. The ions are charge carriers in the nematic phase, whose mobility along long molecular axis is greater than the mobility perpendicular to this direction.

As a result, the electroconductivity is greater in one direction than in another. Therefore, nematic LC usually has positive anisotropy of electroconductivity. The space charge can be formed owing to this anisotropy because of ion division.

The applied field acts on charges, causing occurrence of the substance flow in reciprocal directions. It creates the unstable torque induced by the electroconductivity and acting on molecules. The EHDI effect arises if this torque exceeds all other torques. At low frequencies of an applied field, the instability mode is characterized by that a space charge oscillates with a field frequency. At the same time, so far as the threshold of the Williams domain occurrence is low, a reaction time of the director is sufficiently great. Thus, the threshold voltage sharply increases at approaching to the critical frequency f_c which is connected with a dielectric relaxation τ_c by the relationship [20]:

$$f_c = (\zeta^2 - 1)^{1/2} / \tau_c$$

where $\zeta^2 = \varepsilon_{II}^2 \eta_B (\varepsilon_{\perp} / \varepsilon_{II} - \sigma_{\perp} / \sigma_{II}) / \Delta \varepsilon \varepsilon_{\perp} \eta$ is called by Helfrich parameter; ε_{II} and ε_{\perp} are components of dielectric permittivity, $\Delta \varepsilon$ is dielectric anisotropy; η is the effective viscosity; σ_{II} and σ_{\perp} are electroconductivities along and normal to the director, respectively.

The threshold voltage for static and low frequency field in the case of planar configuration of nematic LC with negative dielectric anisotropy is defined by the formula:

$$U_{th} = -4\pi^3 \varepsilon_{II} K_{33} / \Delta \varepsilon \varepsilon_{\perp} (\zeta^2 - 1),$$

where η_B is the corresponding viscosity for bend deformation. A rise time of the instability is defined by the expression:

$$t_{rise} = \beta \eta_B d^2 / (U^2 - U_{th}^2),$$

while a decay time has the form:

$$t_{decay} = \alpha \eta_B d^2 / \pi^2 K_{33},$$

where α and β are the coefficients depending on LC parameters; d is the cell thickness; U is the voltage of applied static field.

Though the ionic current follows an external field, a separation process of a space charge phase lags on the phase from a field with frequency increasing. It leads to reduction of force influence on a space charge from an external field. The torque corresponding to conductivity,

decreases and it is required to raise an external voltage for instability achievement that is confirmed by the experiment (Fig. 5).

Inclusion of particles in LC feebly alters dielectric permeability and conductivity properties of LC in a static field. Probably, a change in the threshold voltage is connected with other reasons. Barium titanate particles in LC induce development of instability at lower threshold because they are the turbulence centers in LC. At the same time, with increasing of the external field frequency nonconducting particles prevent to a movement of ions and it is required greater voltage to maintain the instability. In connection with it, there is a sharper increase of threshold voltage with a frequency change.

According to the above mentioned expressions, a rise time decreases with voltage increasing that is proved by the experiment. In this case, a presence of particles increases a rise time in comparison with the pure LC. First of all, it is connected with an increase in effective viscosity and a reduction of elastic properties of LC and also with overcoming the additional obstacles (particles) by ions. Furthermore, at application of an external electric field, dipoles of LC molecules near the polarized ferroelectric particles are orientated along electric-field lines, namely, normal to the substrate surface, enhancing the initial homeotropic configuration of the LC molecules. Thereat, an additional torque is formed, which increases a rise time and decreases a decay time in comparison with pure LC at the same voltages. At this case, a minimum in voltage dependence of decay time is connected with polarization of areas near the particles existing an addition torque and promoting chaotic motion of particles.

CONCLUSIONS

It was shown that the occurrence of barium titanate particles in H-37 decreases clearing temperature increases the threshold of the Fredericksz effect, decreases the voltage of the EHDI formation. A rise time increases and a decay time decreases in comparison with the pure H-37. First of all, experimental results are explained by appearance of local electric fields near the polarized ferroelectric particles at application of external electric field and also a change of effective viscosity and elastic properties of LC, existence of the additional obstacles (particles) by ions.

ACKNOWLEDGMENT

This work was supported of the Science and Technology Center in Ukraine (grant no. 5821).

- [1] T.D. Ibragimov. Journal of Applied Spectroscopy. 2009, **76**, No5, 793-796.
- [2] T.D. Ibragimov, E.A. Allahverdiyev, G.M. Bayramov, and A.R. Imamaliyev. Journal of Applied Spectroscopy, **78** (2011) 445-449.
- [3] T. D. Ibragimov, G.M. Bayramov. Infrared Physics and Technology. **55**, No1 (2012) 56-59.
- [4] T.D. Ibragimov, G.M. Bayramov. Optika. **124** (2013) 6666-6668.
- [5] T.D. Ibragimov, N.J. Ismailov, E.A. Allahverdiyev. Tunable liquid crystalline filter. Eurasian patent No 016161 (2012).
- [6] T.D. Ibragimov, G.M. Bayramov, A.R. Imamaliyev. Optika. **124**, 2013, 343-346.
- [7] T.D. Ibragimov, G.M. Bayramov. Optika. **124** (2013) 3004-3006.
- [8] Yu. Reznikov. Ferroelectric colloids in liquid crystals. (In Liquid Crystals Beyond Displays:

- Chemistry, Physics, and Applications, Edited by Quan Li.) John Wiley and Sons, Inc. 2012, 403-427.
- [9] *M. Gorkunov, M. Osipov. Soft Matter* **7** (2011) 4348-4356.
- [10] *F. Brochard, P.G. de Gennes. J. de Physique.* **31** (1970) 691-706.
- [11] *O. Buy, E. Guskova, Yu. Reznikov, P. Litvin. Ukr. J. Phys.* **49**, A12 (2004) A48-A50.
- [12] *O. Buchnev, E. Ouskova, and Yu. Reznikov, V. Reshetnyak H. Kresse. Mol. Cryst. Liq. Cryst.,* **422** (2004) 47 [317]–55 [325].
- [13] *E. Quskova, O. Buchnev, V. Reshetnyak, Yu. Reznikov, H. Kresse. Liquid Crystal,* **30**, No. 10 (2003) 1235–1239.
- [14] *O. Buchnev, A. Dyadyusha, M. Kaczmarek, V. Reshetnyak, Yu. Reznikov. J. Opt. Soc. Am. B,* **24**, No. 7 (2007) 1512-1516.
- [15] *R. Basu. Physical Review E* **89** (2014) 022508-1-022508-5.
- [16] *E.F. Carr, R.W.H. Kozlowski, M. Shamsai, in: A.G. Griffin, J.F. Johnson (Eds.), Liquid Crystals and Ordered Fluids, Plenum Press, New York, 1984.*
- [17] *F. Haragushi, K. Inoue, N. Toshima, S. Kobayashi, and K. Tukato. Japanese Journal Applied Physics.* **46** (2007) L796-L797.
- [18] *Hsing-I Hsiang and Fu-Su Yen. Journal of the American Ceramic Society,* **79** (1996) 1053–1060.
- [19] *S.V. Pasechnik, V.G. Chigrinov, D.V. Shmelikova. Liquid Crystals. Viscous and Elastic Properties. (2009) Wiley-VCH Verlag GmbH and Co. KGaA, Weinheim, 438, p.181.*
- [20] *J.-F. Blach, S. Saitzek, C. Legrand, L. Dupont, J.-F. Henninot, and M. Warenghem. J. Appl. Phys.* **107** (2010) 074102-1 -7.
- [21] *W. Helfrich, J. Chem. Phys.* **51** (1969) 4092–4115.

Received: 29.01.2015

TRAPPING OF CLASSICAL PARTICLES BY A POTENTIAL WELL DEEPENING WITH TIME

AZAD Ch. IZMAILOV

Institute of Physics, Azerbaijan National Academy of Sciences, Javid av. 33, Baku, Az-1143, AZERBAIJAN

e-mail: azizm57@rambler.ru

The new trapping mechanism of sufficiently slow-speed particles by a potential well deepening with time is established from basic relations of classical mechanics. We consider situations when such particles are in high vacuum and external forces acting on given particles are not dissipative. Corresponding potential wells may be induced by a controllable electromagnetic field with nondecreasing strength and fixed spatial distribution. Detailed analysis of features of corresponding traps of particles is carried out on the visual example of the one-dimensional rectangular potential well. Obtained results may be used for motion control and high resolution spectroscopy of charged and neutral particles.

Keywords: electromagnetic traps, classical particles, rectangular potential well, high-resolution spectroscopy

PACS: 45.50.-j, 41.20.-q, 42.50.Wk, 42.62.Fi

1. INTRODUCTION

Electromagnetic traps for free charged and neutral particles without material walls allow to localize and observe these particles during a comparatively long period of time thereby creating conditions for detailed research of their properties [1]. In particular, such traps of microparticles in the high vacuum open new possibilities for contactless measurements of forces acting on given particles with extremely high accuracy and allow their micromanipulations [2].

In the present work we establish and analyze the sufficiently universal mechanism of trapping and localization of classical particles in a potential well, which is induced by an electromagnetic field with a nondecreasing strength and fixed spatial distribution. It is important to note that we consider situations when given particles move in a high vacuum without friction. Depending on whether particles have electric (magnetic) moment, it is possible to use the controllable electric (magnetic) field or nonresonance laser radiation for their analyzed trapping. We establish general conditions for such trapping of sufficiently slow-speed particles from basic relations of classical mechanics (section 2). Detailed analysis of features of corresponding electromagnetic traps of particles is carried out on the visual example of the one-dimensional rectangular well deepening with time (section 3). In conclusions we discuss possible generalizations and applications of obtained results for motion control and high-resolution spectroscopy of various microparticles (section 4).

2. BASIC RELATIONS

Let us consider a point particle with the mass m freely moving in a three-dimensional space before its entering to the region V of the potential well $U(\mathbf{r}, t)$, which explicitly depends not only on the coordinate \mathbf{r} but also on time t . The total energy of such a particle with the non-relativistic velocity \mathbf{v} is described by the known formula [3]:

$$E(\mathbf{r}, \mathbf{v}, t) = 0.5m\mathbf{v}^2 + U(\mathbf{r}, t). \quad (1)$$

Further we will consider the potential energy $U(\mathbf{r}, t)$ of the following form:

$$U(\mathbf{r}, t) = \sigma(\mathbf{r}) * \varphi(t), \quad (2)$$

where the coordinate function $\sigma(\mathbf{r}) \leq 0$ in the region V , and $\varphi(t) \geq 0$ is the nondecreasing function of time t . Such a potential well (2) for particles may be created by a controllable electromagnetic field with the growing strength (up to a certain time moment) but with a fixed spatial distribution [4]. In this case the motion equation [3] for the particle has the form:

$$m \frac{d^2 \mathbf{r}}{dt^2} = -\varphi(t) \frac{d\sigma(\mathbf{r})}{d\mathbf{r}}. \quad (3)$$

On the basis of relationships (1)-(3) we directly receive the following formula for the time derivative of the total energy $E(\mathbf{r}, \mathbf{v}, t)$:

$$\frac{dE}{dt} = \sigma(\mathbf{r}) \frac{d\varphi(t)}{dt} \leq 0. \quad (4)$$

Thus, according to (4), an increase of the function $\varphi(t)$ with time t leads to the decrease of the total energy $E(\mathbf{r}, \mathbf{v}, t)$ (1) of the particle in the region V of the potential well, where $\sigma(\mathbf{r}) < 0$. We see also from the formula (1) that the particle can not go beyond the potential well (where $U(\mathbf{r}, t) = 0$), when its energy E will be negative. It is important to note that such a classical particle will be localized in the region V of the potential well even after output of the nondecreasing function $\varphi(t)$ on a constant maximum value, when a negative total energy $E < 0$ of this particle will be conserved. It is obvious, that sufficiently fast particles will not be captured in the considered trap. Detailed analysis of dynamics of particles may be carried out for electromagnetic traps with definite spatial configurations. In the next section we will establish a number of important features of trapping and localization of sufficiently slow-speed non-relativistic particles on the visual example of the one-dimensional rectangular potential well.

3. ONE-DIMENSIONAL RECTANGULAR POTENTIAL WELL

Let us consider a point particle with the mass m freely moving with the velocity $v_0 > 0$ along the axis x (Fig.1) from the region $x < -L$ and in a certain moment t reaching the boundary $x = -L$ of the following potential well:

$$U(x, t) = -J_0 * \varphi(t) * \eta(L^2 - x^2), \quad (5)$$

where $J_0 > 0$ is the constant value with the energy dimension, $1 \geq \varphi(t) \geq 0$ is the nondecreasing function of time t , $\eta(y)$ is the step function ($\eta(y) = 1$ for $y \geq 0$ and $\eta(y) = 0$ if $y < 0$). From (3) we receive the motion equation of the particle for the potential well (5):

$$m \frac{d^2x}{dt^2} = J_0 * \varphi(t) * [\delta(x + L) - \delta(x - L)], \quad (6)$$

where $\delta(y)$ is the Dirac delta-function. According to Eq.(6), an abrupt increase of the particle velocity occurs from the initial value v_0 to $v \geq v_0$, when this particle falls into the well (5) in the moment t . Connection between given values v_0 and v is determined from the formula (1) for the total energy of the classical particle in this moment t :

$$E(-L, t) = 0.5mv_0^2 = 0.5mv^2 - J_0 * \varphi(t), \quad (7)$$

According to Eq.(6), the considered particle further will move inside the rectangular well (5) with the constant velocity v and will reach the opposite well boundary (with the coordinate $x = L$) in the moment $(t + 2L/v)$. However this particle will not be able to overcome the potential well if its total energy E (1) will become negative because of an increase of the function $\varphi(t)$ (7) with time t , that is at the following condition:

$$0.5mv^2 - J_0 * \varphi(t + 2L/v) < 0. \quad (8)$$

Under condition (8), the particle is reflected from the well boundary with the coordinate $x = L$ and will move in the reverse direction with the constant velocity $(-v)$ up to arrival to the opposite well boundary (with the coordinate $x = -L$) in the moment $(t + 4L/v)$. Because of the relationship $\varphi(t + 4L/v) \geq \varphi(t + 2L/v)$, the similar motion of the particle with the velocity v from the boundary $x = -L$ of the potential well up to $x = L$ will be repeated and so on.

Thus, according to condition (8), the maximum possible speed $v_{max}(t)$ of particles, captured in the considered trap (5) in the moment t , is determined by the equation:

$$0.5mv_{max}^2 = J_0 * \varphi(t + 2L/v_{max}). \quad (9)$$

After finding of the value $v_{max}(t)$ from Eq.(9), we obtain from formula (7) the maximum speed $\tilde{v}_0(t)$ of a free particle, which, after falling into the potential well (5) in the moment t , will be localized in this well:

$$\tilde{v}_0(t) = \sqrt{v_{max}^2(t) - \frac{2J_0 \varphi(t)}{m}}. \quad (10)$$

The minimum speed $v_{min}(t)$ of particles, captured in the considered trap in the moment t , is determined from formula (7) at the value $v_0 = 0$:

$$v_{min}(t) = \sqrt{\frac{2J_0 \varphi(t)}{m}} \quad (11).$$

Let us assume, that the function $\varphi(t)$ in (5) increases up to the maximum value 1 during the period from 0 to T and then will be constant, that is $\varphi(t) = 1$ if $t \geq T$. In this connection we introduce following characteristic values for the potential well (5) with dimensions of speed and energy:

$$w = 2L/T, \quad K = 0.5mw^2. \quad (12)$$

In case of the comparatively shallow well (5), when $J_0 \leq K$, we receive from Eq.(9) the maximum speed $v_{max}(t)$ of particles captured in the trap, which is constant during the period $0 \leq t \leq T$ of growth of the function $\varphi(t)$:

$$v_{max}(t) = v^* = \sqrt{\frac{2J_0}{m}} = w * \sqrt{\frac{J_0}{K}}. \quad (13)$$

Then we obtain the corresponding allowed initial speed of a free particle from (10):

$$\tilde{v}_0(t) = \sqrt{\frac{2J_0}{m} [1 - \varphi(t)]}, \quad (0 \leq t \leq T). \quad (14)$$

In case of a sufficiently large depth of the potential well (5), when $J_0 > K$, according to Eq.(9), the speed $v_{max}(t)$ of particles, captured in the trap, reaches the constant maximum value v^* (13) in the time period $t^* \leq t \leq T$, where

$$t^* = T - 2L * \sqrt{\frac{m}{2J_0}} = \left(1 - \sqrt{\frac{K}{J_0}}\right) T. \quad (15)$$

Further, for definiteness, we consider the following time dependence $\varphi(t)$ of the potential (5):

$$\varphi(t) = \left(\frac{t}{T}\right)^n \eta(T - t) + \eta(t - T), \quad (n > 0, t \geq 0). \quad (16)$$

According to formula (16), the depth of the potential well (5) increases from 0 to J_0 during the period $0 \leq t \leq T$, and will have the maximum constant value J_0 when $t > T$.

Fig.2 presents dependences of speeds $\tilde{v}_0(t)$, $v_{max}(t)$ and $v_{min}(t)$ (9)-(11) of trapped particles on time t for 2 parameters $n=0.5$ and 2 of the given function $\varphi(t)$ (16). We see that the considered potential well (5) carries out

trapping and localization of free particles, whose speeds $|v_0|$ in a moment t of its falling in the well is restricted by the value $\tilde{v}_0(t) > |v_0|$ from relationships (9), (10). Then the speed $|v|$ of given captured particles inside the well is between values $v_{max}(t)$ and $v_{min}(t)$ (Fig.2) determined by (9), (11). Trapping of new particles in the potential well (5), (16) stops after the moment T , when this well will be stationary (Fig.2). However classical particles, captured in the given electromagnetic trap before the moment T , will remain there also in following time $t > T$. Possible speeds $|v|$ of these particles, remained inside the potential well, will be between 0 and $\sqrt{2J_0/m}$. According to Fig.2, speed intervals of particles, captured in such an electromagnetic trap in fixed moments $t < T$,

essentially depend on the parameter n of the function $\varphi(t)$ (16), that is on increase rate of the well depth with time t . At the sufficiently shallow potential well (5), when $J_0 \leq K$, corresponding speeds of particles in Fig.2a,b are described by simple formulas $v_{min}(t)$ (11), $v_{max}(t) = v^*$ (13) and $\tilde{v}_0(t)$ (14). In case $J_0 > K$, increase of the speed $v_{max}(t)$ occurs in the time period $0 \leq t \leq t^*$ (15) and the constant value $v_{max}(t) = v^*$ (13) establishes after the moment t^* (Fig.2c,d). In particular, for the given function $\varphi(t)$ (16), speeds $\tilde{v}_0(t)$ and $v_{max}(t)$ coincide in the initial moment $t = 0$ and, according to (9), (10), have the following form when $J_0 \geq K$:

$$v_{max}(t=0) = \tilde{v}_0(t=0) = \left(\frac{2J_0}{m}\right)^{\frac{1}{(n+2)}} \left(\frac{2L}{T}\right)^{\frac{n}{(n+2)}} = \left(\frac{J_0}{K}\right)^{\frac{1}{(n+2)}} w. \quad (17)$$

According to (17), available speeds of trapped particles increase with growth of the length $2L$ and the depth J_0 of the potential well (5), (16) and also with decrease of the characteristic time T of its deepening.

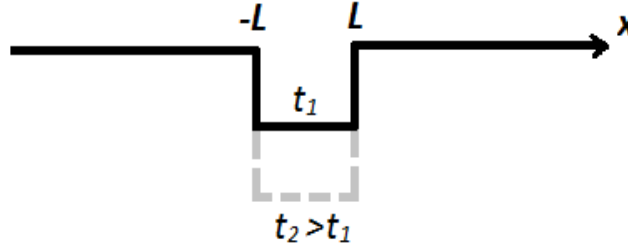


Fig.1. Scheme of the one-dimensional rectangular potential well deepening with time t .

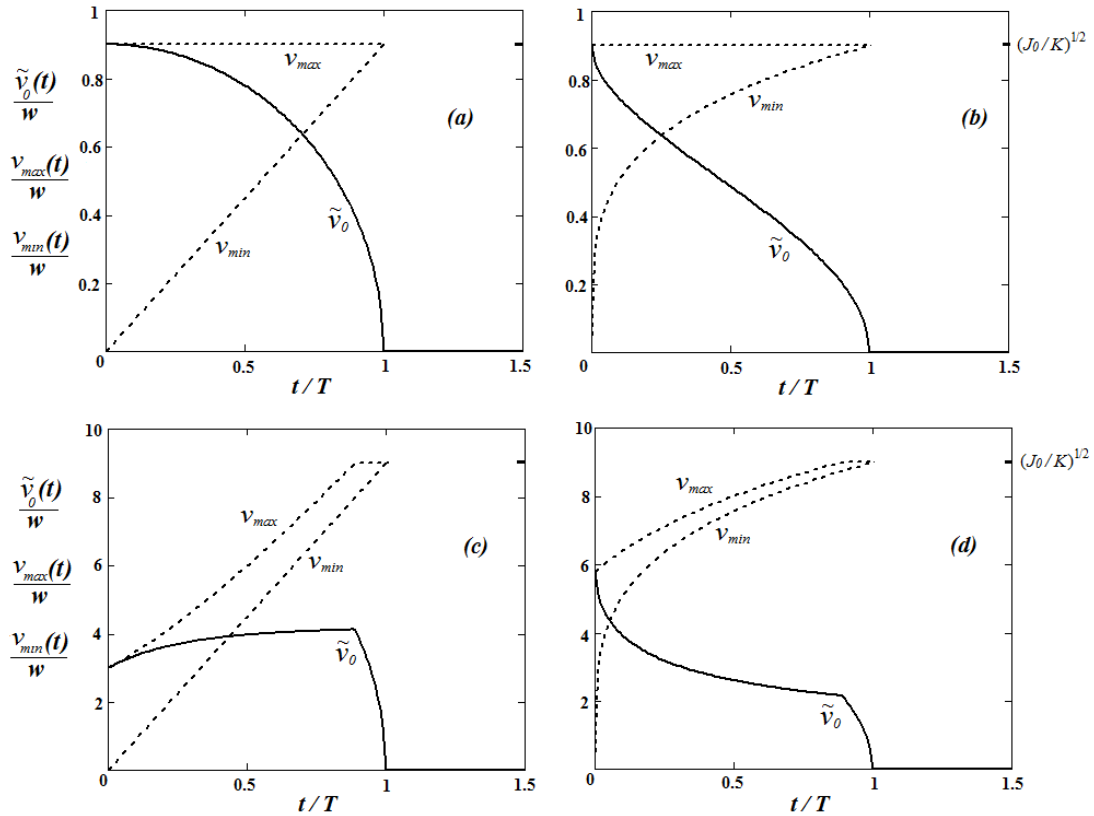


Fig.2. Speeds $\tilde{v}_0(t)$, $v_{max}(t)$ and $v_{min}(t)$ of trapped particles versus time t of their getting into the one-dimensional rectangular potential well (5) with the value $J_0 = 0.81K$ (a, b) and $81K$ (c, d) for the parameter $n=2$ (a, c) and 0.5 (b, d) of the function $\varphi(t)$ (16).

4. CONCLUSIONS

From basic relations of classical mechanics, we have shown possibility of trapping and localization of sufficiently slow-speed particles by a potential well deepening with time, which is described by the general formula (2). Such universal traps may be created in practice for various charged and neutral classical particles (having electric or magnetic moments) by means of the controllable electric or magnetic field with strength increasing during a certain period but at a fixed spatial field distribution. Similar potential wells may be induced also by amplifying nonresonance laser beams of definite spatial configurations.

In section 3 we have established a number of interesting features of given electromagnetic traps on the visual example of the one-dimensional rectangular potential well. Such a well may be created in practice by the controllable local homogeneous electric (or magnetic) field on the propagation path of a collimated beam of classical particles having electric (or magnetic) moment. During the definite time of growth of the given field strength (up to a certain maximum value), such an electromagnetic well will capture sufficiently slow-speed particles from the beam. Characteristic speeds of these trapped particles may be estimated on the basis of relations obtained in the present work.

Author have carried out numerical calculations also for some other potential wells of the type (2), including

cases of two- and three-dimensional wells with cylindrical and spherical symmetries. These calculations confirmed following qualitative results (a), (b) and (c) of given work.

(a) Even a highly shallow but deepening with time potential wells of the type (2) will continuously capture sufficiently slow-speed particles.

(b) Such trapped classical particles will remain inside the potential well even after going out of the corresponding nondecreasing electromagnetic field on a stationary value. However this stationary well already will not capture new particles.

(c) Trapped particles will carry out nondamped oscillatory motions within a corresponding potential well because such wells are based on nondissipative forces in the high vacuum.

Of course, results obtained in the present work are valid only in the absence of an interaction between particles travelling through a potential well. However such an interaction may be essential at a sufficiently high concentration of captured particles in a comparatively small volume of an electromagnetic trap.

Considered electromagnetic traps will extend possibilities for motion control and high resolution spectroscopy of such noninteracting microparticles which move without friction in the high vacuum under action of the controllable electric (magnetic) field or nonresonance laser radiation.

-
- [1] *W. Paul*. 1990, "Electromagnetic traps for charged and neutral particles" (Nobel Lecture), *Angewandte Chemie*, International Edition in English, **29**(7), pp. 739-748.
 - [2] *A. Ashkin*. 2006, *Optical Trapping and Manipulation of Neutral Particles Using Lasers*. World Scientific Publishing.
 - [3] *J.R. Taylor*, 2005, *Classical Mechanics*, University Science Books.
 - [4] *M. Mansuripur*, 2011, *Field, Force, Energy and Momentum in Classical Electrodynamics*, Bentham e Books.

Received: 07.02.2014

INVESTIGATION Of YAG:Ce LUMINESCENCE PROPERTIES AND MANIPULATION OF PHOSPHOR CONVERTED WHITE LED's COLOR CHARACTERISTICS

T.Y. ORUJOV¹, S.A. MAMMADOVA¹, S.H. ABDULLAYEVA^{1,2},
N. N. MUSAYEVA^{1,2}, R.B. JABBAROV^{1,2}

*G.M. Abdullayev Institute of Physics, Azerbaijan National Academy of Sciences, Baku, Azerbaijan¹
Research and Development Center of High Technologies²,
Ministry of Communications and High Technologies²*

Ce³⁺ activated yttrium aluminum garnet (Y₃Al₅O₁₂:Ce, YAG:Ce) powder as luminescent phosphor was synthesized by the solid-state reaction method. The phase identification, microstructure and photoluminescent properties of the products were investigated by X-ray diffraction (XRD), scanning electron microscopy (SEM), photoluminescence (PL) analysis.

Then high power phosphor converted white LEDs with different CCTs were fabricated with the use of blue InGaN dies and YAG:Ce phosphor and their light characteristics were measured and compared. The LEDs generated white light with the CCTs of 6444 K, 4624 K and 8825 K. Their optical parameters were measured in an integrating sphere at various driving currents, and the LEDs showed a luminous efficiency of 96 (81, 69) lm/W at 0.5 (2, 3.5) A.

Keywords: Light emitting diode; Luminescence; Phosphor

PACS: 33.50.-j, 33.50.D

1. INTRODUCTION

Light emitting diodes are bound to replace traditional light sources such as incandescent and fluorescent lamps in the nearest future, and the phosphor converted light white emitting diodes (pcLED) technology is the most promising one. There are a few ways to get white light with pcLEDs. One of them is to combine a UV LED with red, green and blue phosphors. But probably the most effective method of all is to use a blue LED covered with yellow emission phosphor, which will be discussed in this paper.

There are a lot of phosphors that can be used to convert LEDs blue emission into visible white light, but yttrium aluminum garnet- Y₃Al₅O₁₂ doped with small amounts of cerium Ce³⁺ seems to be the most practical among all of them because of its low price and ease of preparation. Yttrium aluminum garnet (Y₃Al₅O₁₂) doped with Ce³⁺ is not a new material, it has been widely used throughout the decades in such devices as cathode-ray tubes and field emission displays, and now has found a new application in lighting industry [1].

The quantum efficiency of YAG:Ce is usually very high reaching the value of 90% or even higher. Y₂O₃-Al₂O₃ system is known to have three different crystal phases: YAlO₃ (YAP) with a perovskite structure, Y₄Al₂O₉ (YAM) with a monoclinic structure and Y₃Al₅O₁₂ (YAG) with a cubic garnet structure [2], with the last one being more difficult to obtain compared to the other two. Pure phase YAG is synthesized by solid-state diffusion reaction methods, requiring sintering at high temperatures above 1550°C.

The phosphor coating is by far the most important step in LED packaging process as it is set side by side with such factors as amount of phosphor covering the LED dies, thickness of phosphor layer and phosphor coating technique. All these factors have an influence on the final light characteristics of an LED and its quality. The most important parameters of a pcLED are correlated color temperature (CCT), color rendering index (CRI) and luminous efficiency (lm/W).

2. EXPERIMENTAL SECTION

2.1 Phosphor synthesis

There are different synthesis methods of crystalline powders of YAG:Ce. Four methods are described by Pan et al. [3]. We used solid-state reaction method to prepare crystalline powder samples of YAG:Ce with 2% Ce³⁺ concentration. The reactants such as Y₂O₃, Al₂O₃ and CeO₂ were mixed in a stoichiometric amounts at 1500°C for 2 hour (5% H₂, 95% N₂ reducing atmosphere). To obtain uniform size the grinded samples were passed through different sieves. X-ray diffraction patterns were recorded using a Bruker 5000 diffractometer in standard θ -2 θ geometry with CuK α radiation. All investigated samples turned out to be single-phase ones.

Photoluminescence (PL) excitation and emission spectra were recorded between 77 and 350 K on the FS 920 fluorescent spectrometer (Edinburgh Instruments) equipped with a Hamamatsu R928P red-sensitive photomultiplier (wavelength range from 200 to 850nm). An Oxford Optistat CF cryostat was used to cover a measurement temperature range from 4 to 500K and to record the TL properties.

The morphology of the samples was observed using the secondary electron detector of the S-3400N series type II scanning electron microscope (SEM) from HITACHI Company.

2.2 PcLED fabrication

PcLED arrays were fabricated on the basis of analyzed YAG:Ce phosphor and blue InGaN dies. They were manufactured by the chip on board technology. The advantage of such technology is that the dies are mounted directly onto the board, allowing heat to sink much better than in SMD type packages.

To assemble the LED package the Metal Core Printed Circuit Board (MCPCB) was used. First the dies were attached to the substrate using Delvotek's A1die placing equipment. 100 dies, 1 watt each, formed a matrix of 10×10, connected in series and in parallel. The dies

used were 1×1 mm blue dies manufactured by MOCVD process. The dies were attached to the substrates by means of epoxy glue, to harden the glue the substrates were placed in a heater and kept there at 150°C for about an hour (fig. 1a,b). After that the samples were sent to the plasma-ion cleaning system where their surface was

polished in ionized Ar for 3 minutes to make it free of dust and small particles. At the next stage the dies were electrically connected to each other, and the arrays were connected to the contact pads closing the circuit. The dies were bonded with the golden wire 25µm in diameter using a Delvotec G5 ultrasonic bonding machine (fig. 1c).

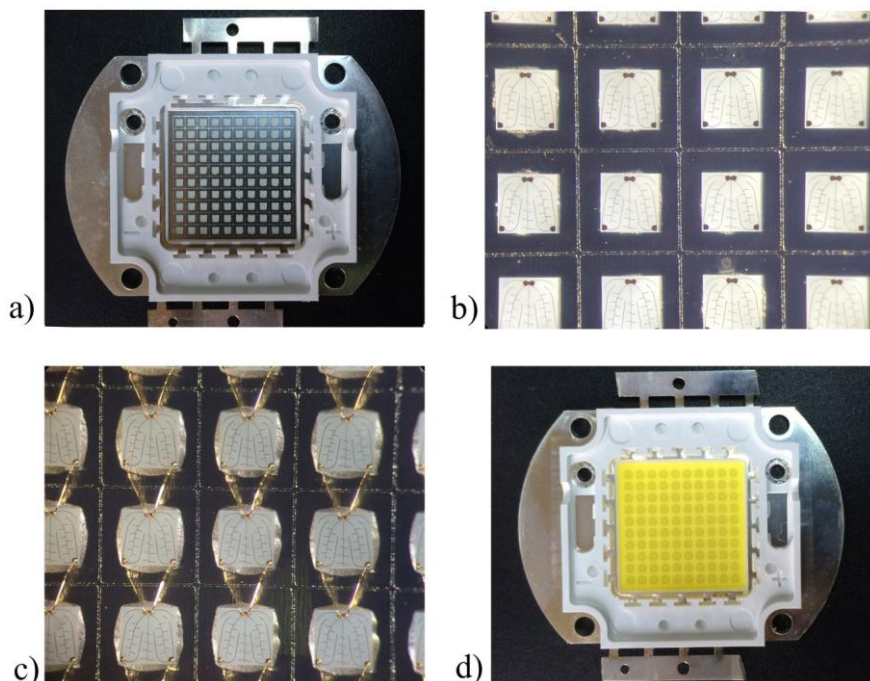
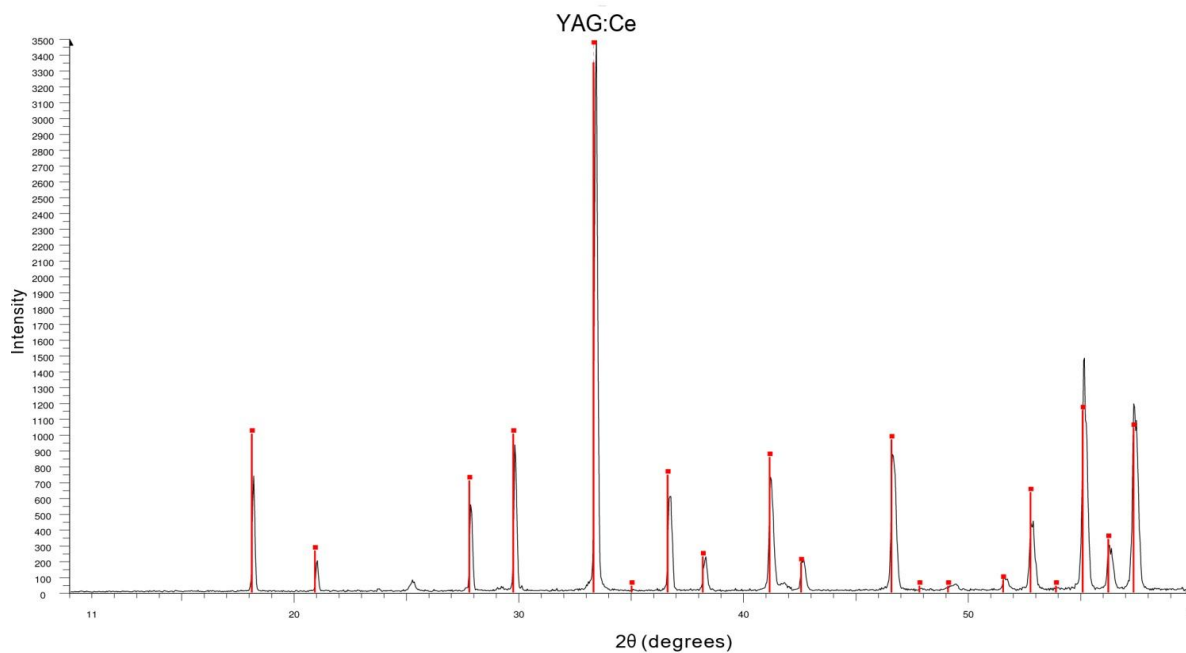


Fig. 1. a) Substrate with attached dies, b) dies on the substrate (enlarged), c) dies bonded with gold wire (25µm), d) LED coated with phosphor.



YAG:Ce -raw. Start: 10.000° - End: 60.000° -step: 0.040° -step time 1.2 s -Tem: 25°C (room temp.)- Time started: 17s- 2θ: 10.000° - θ: 5.000° C

Aluminum Yttrium -Oxide - $\text{Al}_5\text{Y}_3\text{O}_{12}$ -Y: 105.49%-dx by: 1.-WL:1.5406 -Cubic -a 12.00890- b 12.00890- c 12.00890 -alpha 90.000-beta 90.000-gamma 90.000-Body centered-Ia3d(230)

Fig.1. XRD for YAG:Ce.

And at the last step the LED arrays were covered with YAG:Ce phosphor to convert the blue LED light into white light (fig. 1d). Epoxy resin was used as an encapsulating material, and was mixed with YAG:Ce powder in three different ratios. The concentrations of phosphor in 1 gr of epoxy were made: 7%, 10%, 16%, while the thickness of the encapsulating layer remained constant. This mixture was dispensed on top of the dies using a dispenser to achieve a uniform layer of phosphor throughout the substrate. Then the LEDs were baked in the binder at the temperature of 90°C for about 10 minutes to provide some hardening of the encapsulating material, but at the same time not long enough to keep it viscous. Then whole LEDs were covered with a second transparent layer of epoxy to protect the phosphor and the wires from damage. After that the LEDs were placed into the binder heater to give it the final bake at 120°C, at this temperature both layers fully hardened.

For the measurement of their optical and electrical parameters the LEDs were placed into the Everfine's PMS-80 optical integrating sphere and tested at various currents: 0.5 A, 2A, 3.5 A. The forward voltage drop of a single die is 3 volts, and the whole array is powered by 30 volts, so at 3.5A the LED was pushed to 100 watts of electrical power.

3. RESULTS AND DISCUSSION

3.1 X-ray Diffraction (XRD) analysis of YAG:Ce

XRD is a non-destructive analytical method used for identification and quantitative determination of the various crystalline forms (known as phases) present in samples. The phase identification is important because the properties of the phosphorescent powder are strongly dependent on the structure. The diffractogram shows the phases present (peak position), phase concentrations (peak heights), and crystalline size/strain (peak width).

Figure 1 shows the XRD analysis of YAG:Ce, we observed the product to be a single-phase one.

3.2 SEM analysis of YAG:Ce

The morphology analysis of the samples was conducted on the new Hitachi S-3400N Variable Pressure SEM. It is equipped with a Secondary Electron Detector High Sensitivity Semiconductor BSE Detector, and is capable of giving a resolution of 10 nm at 3 kV and 3 nm at 30 kV. Fig. 2 shows the photo taken by the SEM at the WD=10.7 mm, the voltage on the gun -15 kV. It is evident from the figure that particles are of spherical shape and have various micron sizes and lengths.

3.3 PL properties of YAG:Ce

Figure 3 shows the energy levels of a Ce^{3+} ion, as well as the processes that take place when it's located in a host lattice. A free Ce^{3+} ion in its fundamental state has a 4f electron configuration which is split into two multiplets: $^2F_{5/2}$ and $^2F_{7/2}$, and in excited state it has a 5d electron configuration. When the Ce^{3+} ion gets to its excited state, the 5d electrons form a 2D term, which is split into $^2D_{3/2}$ and $^2D_{5/2}$ multiplets by spin-orbit coupling [4]. $^2D_{5/2}$ is an unstable level, and its electrons tend to relax to $^2D_{3/2}$ level when they meet a photon. When a Ce^{3+} ion is placed in a host crystal such as YAG as an activator ion, its 5d electrons are influenced by the host crystal's atoms and two effects act on the 5d configuration: the centroid shift and crystal field splitting. The 4f configuration on the other hand is not much affected by these effects. Both of these effects lower the energy gap between 5d and 4f levels (red shift). In YAG:Ce, the Ce^{3+} ions occupy the dodecahedral sites in the host lattices, and in this case the energy gap between the fundamental and excited states becomes $22,000\text{ cm}^{-1}$, which is equivalent to blue light.

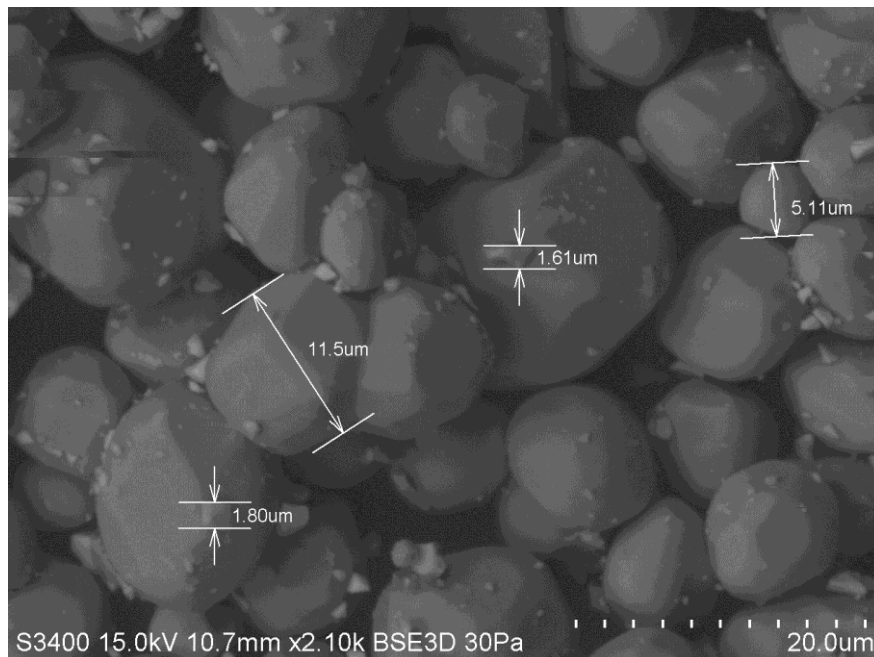


Fig. 2. SEM analysis of YAG:Ce.

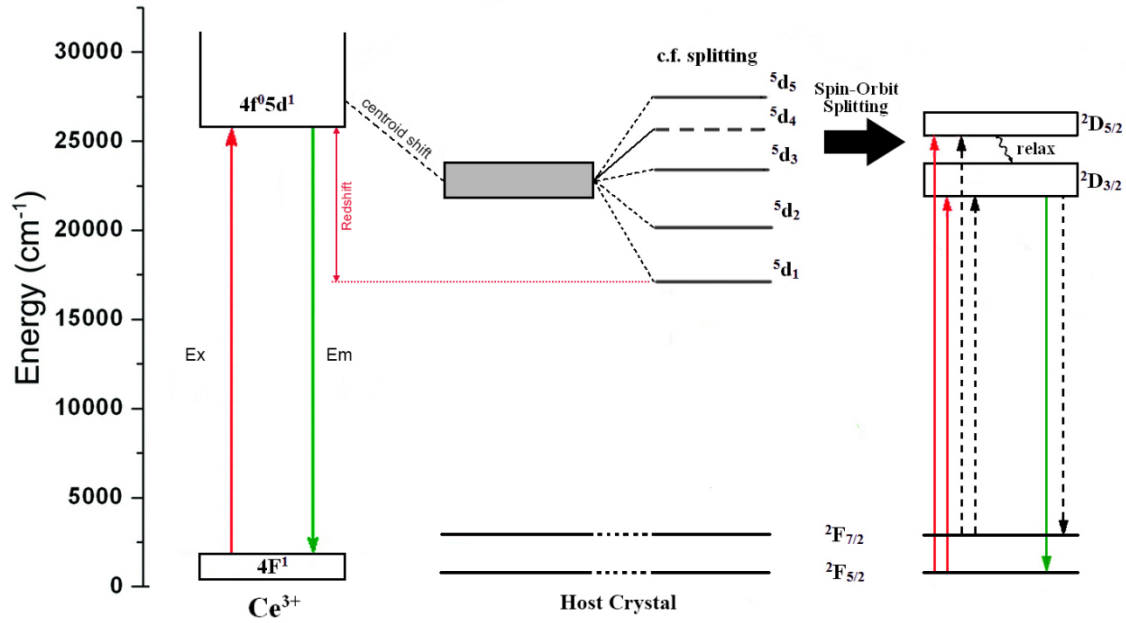


Fig. 3. A schematic energy level diagram for Ce^{3+} showing its excitation (Ex) and emission (Em) processes and the effects of a host crystal A.

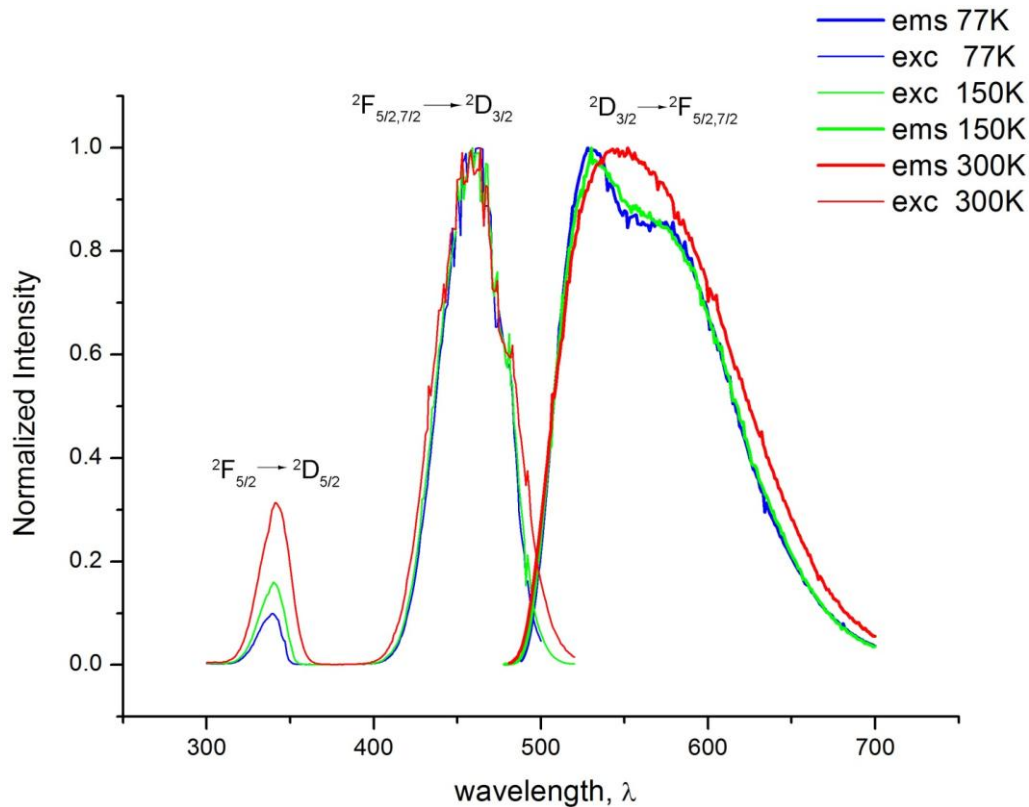


Fig. 4. The excitation and emission spectra of YAG:Ce at different temperatures.

3.3 PL properties of YAG:Ce

Figure 3 shows the energy levels of a Ce^{3+} ion, as well as the processes that take place when it's located in a host lattice. A free Ce^{3+} ion in its fundamental state has a $4f$ electron configuration which is split into two multiplets: $2F_{5/2}$ and $2F_{7/2}$, and in excited state it has a $5d$ electron configuration. When the Ce^{3+} ion gets to its

excited state, the $5d$ electrons form a $2D$ term, which is split into $2D_{3/2}$ and $2D_{5/2}$ multiplets by spin-orbit coupling [4]. $2D_{5/2}$ is an unstable level, and its electrons tend to relax to $2D_{3/2}$ level when they meet a photon. When a Ce^{3+} ion is placed in a host crystal such as YAG as an activator ion, its $5d$ electrons are influenced by the host crystal's atoms and two effects act on the $5d$ configuration: the centroid shift and crystal field splitting. The $4f$

configuration on the other hand is not much affected by these effects. Both of these effects lower the energy gap between 5d and 4f levels (red shift). In YAG:Ce, the Ce^{3+} ions occupy the dodecahedral sites in the host lattices, and in this case the energy gap between the fundamental and excited states becomes $22,000 \text{ cm}^{-1}$, which is equivalent to blue light.

Fig. 4 presents the photoluminescence spectra of YAG:Ce at different temperatures: 77, 150, 300K, where two excitation bands with the peaks at 341 and 460 nm (at room temperature) can be discerned, which should be attributed to $^2\text{F}_{5/2} \rightarrow ^2\text{D}_{3/2}$ ($^2\text{D}_{5/2}$) and $^2\text{F}_{3/2} \rightarrow ^2\text{D}_{3/2}$ ($^2\text{D}_{5/2}$) transitions. The emission spectra at room temperature ($T=300\text{K}$) is a broadband spectra with a peak at 553 nm excited by 460 nm which occurs by the $^2\text{D}_{3/2} \rightarrow ^2\text{F}_{7/2}$ ($^2\text{F}_{5/2}$) transitions. Apparently at 77K and 150K the excitation spectrum is found to be asymmetrical, stemming from the $5\text{D} \rightarrow ^2\text{F}_{5/2}$ and $5\text{D} \rightarrow ^2\text{F}_{7/2}$ transitions. It also becomes clear from the graph that the emission spectra changes with the increase of temperature from 77 K to 300 K, shifting from 528 nm to 533 nm. In theory this shift occurs on account of the increasing number of non-radioactive transitions, which also leads to phosphor's efficiency drop too.

3.4 Measurement of pcLED's optical parameters

Fig. 5 shows how the EL spectra of the blue InGaN LED matches the photoluminescence excitation spectrum of YAG:Ce phosphor, and also its emission spectrum. The LED dies that were used for the fabrication of the LED arrays emitted light with a peak wavelength of about 447 nm. It can be observed on the graph that the phosphor's excitation and blue LED's emission bands overlap with each other.

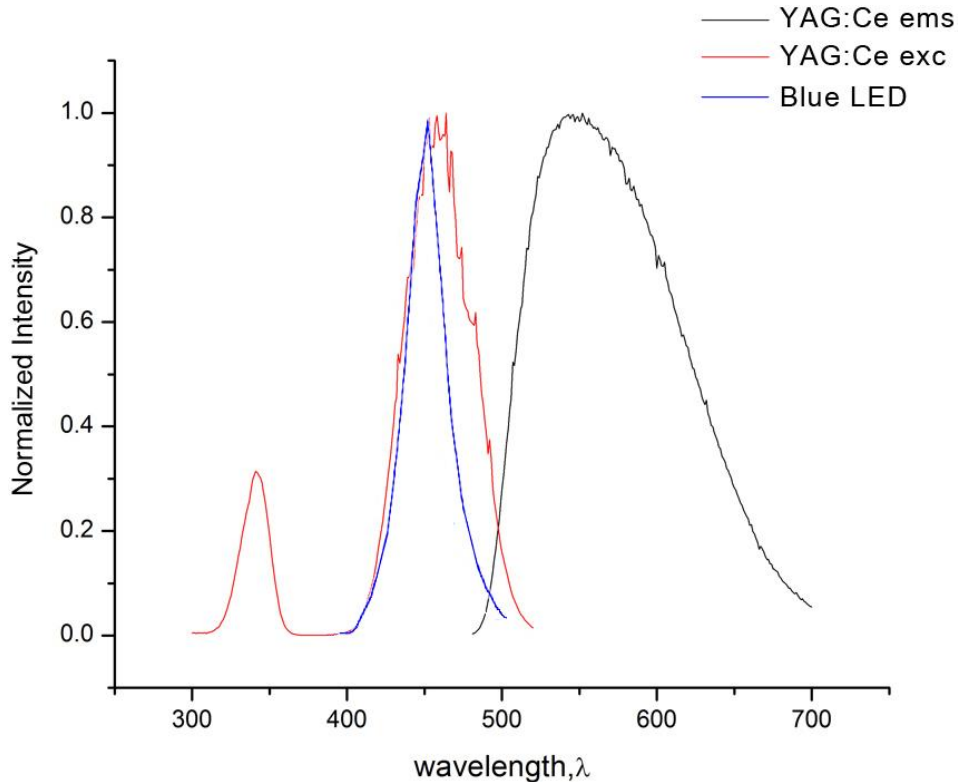


Fig. 5. PL and PLE spectra of YAG:Ce and EL spectra of blue LED.

Fig. 6 shows the EL spectra of the blue LED coated with the YAG:Ce phosphor driven at the various forward currents: 0.5 A, 2 A and 3.5 A. The graph shows an arrow peak which is created by the blue LED. The rest of the spectrum is YAG:Ce phosphor's broadband emission spectra ranging from green 500 nm up to red 650 nm wavelengths. The luminous efficiency of the pcLED was 96 lm/W at 0.5 A, 81 lm/W at 2 A and 69 lm/W at 3.5 A, so it's obviously decreasing with increasing current. This effect is partially due to InGaN LED's luminous efficiency droop with current growth, as well as phosphor's luminous efficiency droop. One of the reasons to this is that the heat generated by the LED dies is transferred to the phosphor, raising its temperature, and as a result we see a drop in phosphor's quantum efficiency η_e .

Fig. 7 shows the Commission Internationale de l'Eclairage (CIE 1931) color coordinates of three pcLED's with different amounts of YAG:Ce phosphor. The LEDs with the 1) 7%, 2) 10%, 3) 16% concentrations of phosphor in 1 gr of epoxy are depicted on the diagram as Δ , \square and \diamond , respectively. So by varying the phosphor concentration it is possible to control the correlated color temperature of the emitted light, which goes down with the increase of phosphor amount. The color coordinates of the LED with the 10% phosphor concentration are located right on the Planckian Locus near to the D65 point, and it gives pure white light with the CCT $T_2=6444\text{K}$, while other two LEDs (Δ , \diamond) give warm ($T_1=4624\text{K}$) and cool ($T_3=8825\text{K}$) white light. The CRIs of three samples were: $R_1=61$, $R_2=67$, $R_3=72$. The color coordinates were overall stable and changed only marginally when applied current was increased.

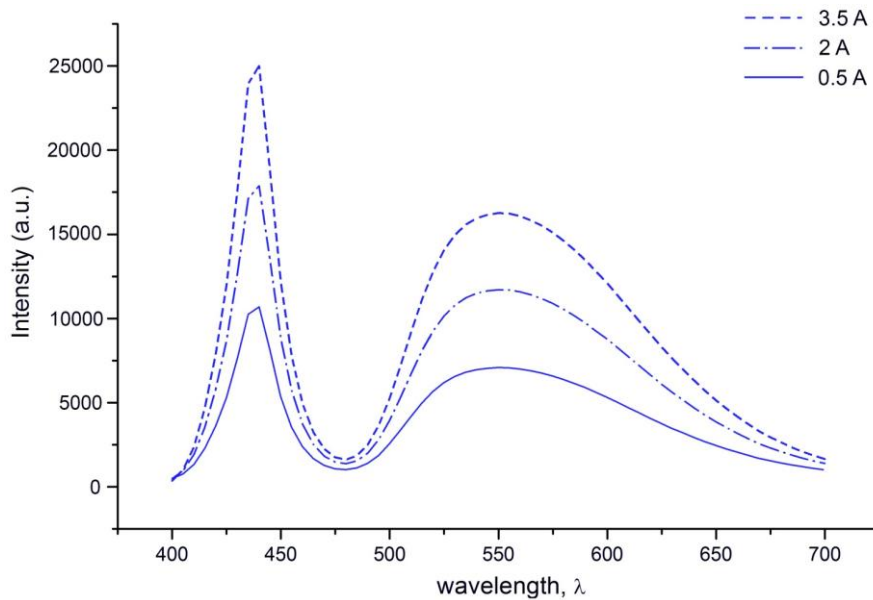


Fig. 6. EL spectra of the pcLED at various driving currents: 0.5A, 2A, 3.5A.

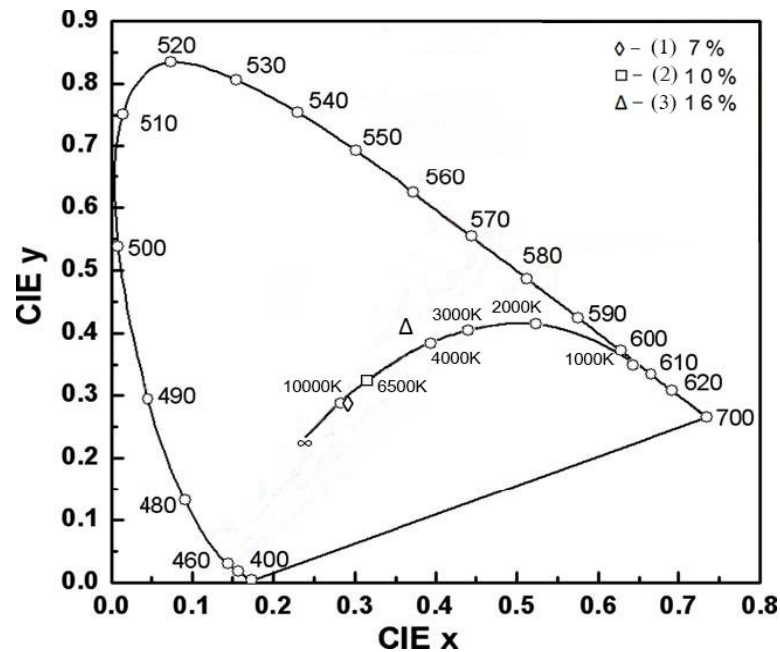


Fig. 7. The Chromaticity diagram color coordinates of pcLEDs with various phosphor concentrations: 1) 7%, 2) □- 10%, 3) ◇- 16%.

Fig. 7 shows the Commission Internationale de l'Eclairage (CIE 1931) color coordinates of three pcLED's with different amounts of YAG:Ce phosphor. The LEDs with the 1) 7%, 2) 10%, 3) 16% concentrations of phosphor in 1 gr of epoxy are depicted on the diagram as Δ , \square and \diamond , respectively. So by varying the phosphor concentration it is possible to control the correlated color temperature of the emitted light, which goes down with the increase of phosphor amount. The color coordinates of the LED with the 10% phosphor concentration are located right on the Planckian Locus near to the D65 point, and it gives pure white light with the CCT $T_2=6444\text{K}$, while other two LEDs (Δ , \diamond) give warm ($T_1=4624\text{K}$) and cool ($T_3=8825\text{K}$) white light. The CRIs of three samples were: $R_1=61$, $R_2=67$, $R_3=72$. The color coordinates were overall stable and changed only marginally when applied current was increased.

4. CONCLUSION

The yellow Yttrium Aluminum Garnet phosphor activated with Ce^{3+} ions has been analyzed and used to fabricated powerful pcLEDs on its basis. By varying the phosphor quantity in the epoxy covering the blue LED it is possible to manipulate the CCT, and we managed to get pure white light pcLED with the CCT of 6444K, the CRI of 67 and the efficiency of $\sim 80 \text{ lm/W}$. YAG:Ce phosphor produces an intense emission in the green and yellow wavelength band, however, it somewhat lacks the warm reddish spectra and the CRI is quite low because of it. Therefore, it is ideal for the manufacture of cool white light pcLEDs, which are suitable for use in street lighting and spotlighting.

- [1] *D. Hanatath, H. Chander, P.Sharma and S. Sigh.* Appl. Phys. Lett., 89 17 3118 /1-173 118/3. (2006).
- [2] *L. Chen, C.-C. Lin, C.-W. Yeh and R.-S. Liu.* Materials, 3, 2172-2195 (2010).
- [3] *Y. Matsui, H. Horikawa, M. Iwasaki and W. Park.* Journal of Ceramic Processing Research Vol. 12. № 3, p 348 -351 (2011).
- [4] *N.C. George, K.A. Denault and R. Seshadri.* Annual Review of Materials Research 43, p 481-501 (2013).
- [5] *Y. Pan, M. Wu and Q. Su.* Mat. Sci. Eng. B, 106.251. (2004).
- [6] *H.S. Jang, Y.-H. Won and D.Y. Jeon.* Appl. Phys, B 95: 715–720 (2009).
- [7] *S. Liu and X. Luo.* John Wiley Press, USA, (2011).
- [8] *N. Narendran, Y. Gu.* Third International Conference on Solid State Lighting, Proceedings of SPIE, 5187: 107-114 (2004).
- [9] *S.C. Huang, J. K. Wuand, W.-J. Hsu.* Int. J. Appl. Ceram. Technol., 6 ,465-469 (2009).
- [10] *I. Kebaili and M. Dammak.* Journal of Theoretical and Applied Physics, 6:21 (2012).

Received: 12.01.2015

THE INFLUENCE OF GAMMA IRRADIATION ON ELECTRIC PROPERTIES OF POLYVINYLIDENE FLUORIDE COMPOSITES WITH SILICON

A.M. MAGERRAMOV, I.M. NURUYEV, R.N. MEHDIYEVA, M.A. NURIYEV

Institute of Radiational Problems of ANAS
 AZ 1143, B.Vakhabzade 9, Baku, Azerbaijan
nuruyev_ibrahim@mail.ru

The influence of gamma irradiation up to dose 300K Gy on electric properties of polymer composites on the base of copolymer of polyvinylidene fluoride with tetrafluoroethylene P(VDF-TFE) and micro- and nano-particles of silicon is studied. It is shown that observable changes in electric properties of irradiated composites on the base of P(VDF-TFE) with micro- and nano-particles of silicon are connected with both processes of radical formation and oxidation with further cross-linking and destruction in heterogeneous system and redistribution of absorbed dose of radiation energy between components of composite.

Keywords: P(VDF-TFE), micro- and nano-particles of silicon, polymer composite, electric properties, gamma irradiation, temperature dependence of specific resistance, mobility, interface.

PACS: 61.80.x; 72.80.Tm

INTRODUCTION

The introduction of different fillers with specific properties in polymer materials is the one of effective methods of electric property modification of polymer materials to use in electronics. The composite materials obtained by such modification acquire the different active properties in dependence on filler type and properties [1-5]. Moreover, the composite acquired properties can be modified by external influences including the ionizing radiation [6-9]. The study of scientific literature shows that composites with semiconductor inclusions are of large interest. According to supposition of authors of these works, the current value in composites is defined by distance of interparticle isolating layer and VAC of samples forms because of electron tunneling through this composite interlayer. The influence of gamma irradiation on electric properties of composites on the base of copolymer of polyvinylidene fluoride with tetrafluoroethylene P(VDF-TFE) with different content of micro- and nano-particles of silicon (Si) is also investigated in the given work.

EXPERIMENTAL PART

The composites are obtained by hot pressing method of previously mixed powders in definite volume component ratios. The pressing is carried out at melting point of polymer matrix under pressure 10MPa during 5 minutes with further melt cooling by the deeping way in aquatic environment at ice temperature. The resistance measurement of composite samples is carried out by E6-13A teraohmmeter at heating rate 2K/min. The samples in "sandwich" form with plane-parallel electrodes from aluminum are used for measurement of ρ_v specific volume resistance.

RESULT DISCUSSION

The composite temperature dependences of ρ_v resistivity are investigated for study of kinetics change in conduction process taking place before and after

irradiation exposure in composites with different filler content. Temperature dependences $\lg \rho = f(1/T)$ of initial and irradiated polymer P(VDF-TFE) are shown in fig.1. It is seen that ρ_v values of initial and irradiated polymer monotonously decrease but some stabilization of ρ_v value with further decrease is observed in average temperature range (363-393K) for irradiated samples.

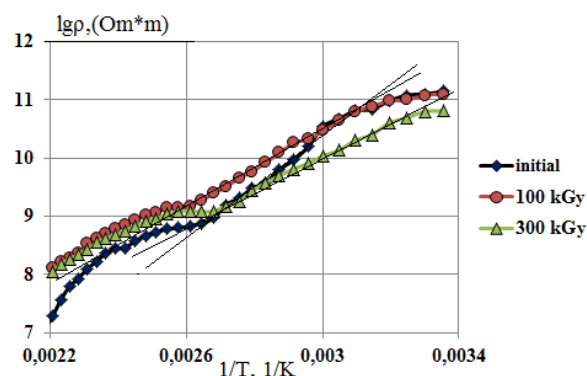
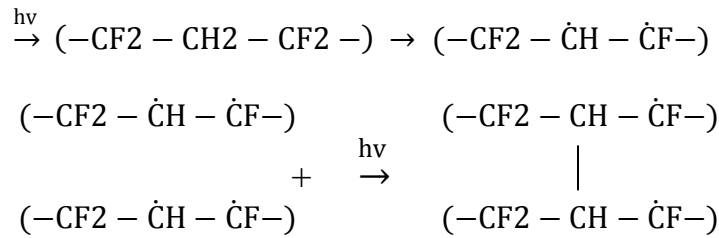


Fig.1. The temperature dependences of volume specific resistance of P(VDF-TFE) polymer irradiated by different dose.

The insignificant decrease of curve inclination angle in comparison with one of initial P(VDF-TFE) is observed in temperature dependence of irradiated polymer samples. We think that the decrease of P(VDF-TFE) polymer chain mobility as a result of carrying out cross-linking after gamma irradiation causes to fact above mentioned. Moreover, irradiation by high doses leads to shift of initial value increase of $\lg \rho = f(1/T)$ to the side of low temperatures connected with destruction beginning of some weakly bound molecular units of polymer chain. As it is known from [12,13] the ionizing irradiation of fluorine-containing polymers is accompanied by decrease of CF_2 group number which transform into polymer radicals $\dot{\text{C}}\text{H}$ and $\dot{\text{C}}\text{F}$. As a result, the part of radicals in polymer structure leads to formation of inter-chain cross-linking because of recombination on following scheme:



The intra-chain transversal cross-linking because of presented reaction is accompanied by increase of polymer matrix hardness and decrease of molecular chain mobility in interphase interlayer.

From comparison $lg\rho = f(1/T)$ dependence for composites with Si micro-particles (fig.2a) it is seen that inclination angle of curves in low-temperature region changes with radiation dose and filler content increasing. The some stabilization (1%Si) and increase with decrease (5 and 10%Si) of ρ_v value are observed in high-temperature dependence part in region below melting point of polymer matrix. We think that high volume contents and radiation doses (300kGy) lead to increase of radical relative concentrations and volume bound charge number in polymer matrix. At high temperatures the radical recombination taking place with volume free charges in matrix leads to relatively rapid decrease of composite ρ_v value. The further stabilization and decrease

of ρ_v are the result of saving properties structure of polymer-filler interface, which destroys at composite melting as a whole.

Stabilization of ρ_v for samples with 1% volume content observable in high-temperature part of $\lg \rho = f(1/T)$ composite dependence shifts to relatively wide maximum for composites with 3,5 and 10% filler volume content at radiation high doses ($\sim 300\text{KGy}$). The processes of free charge capture by radicals (defects and energy traps) together with cross-linking processes take place at irradiation of samples [14,15]. The inverse mechanism leading to charge release takes place at heating. Besides, radical oxidation can lead to radical trap destroy accompanying with charge release from them and increase of sample electric conduction. But values of accumulated charges aren't endless ones and the some ρ_v increase taking place after its minimum value at high temperatures is observed.

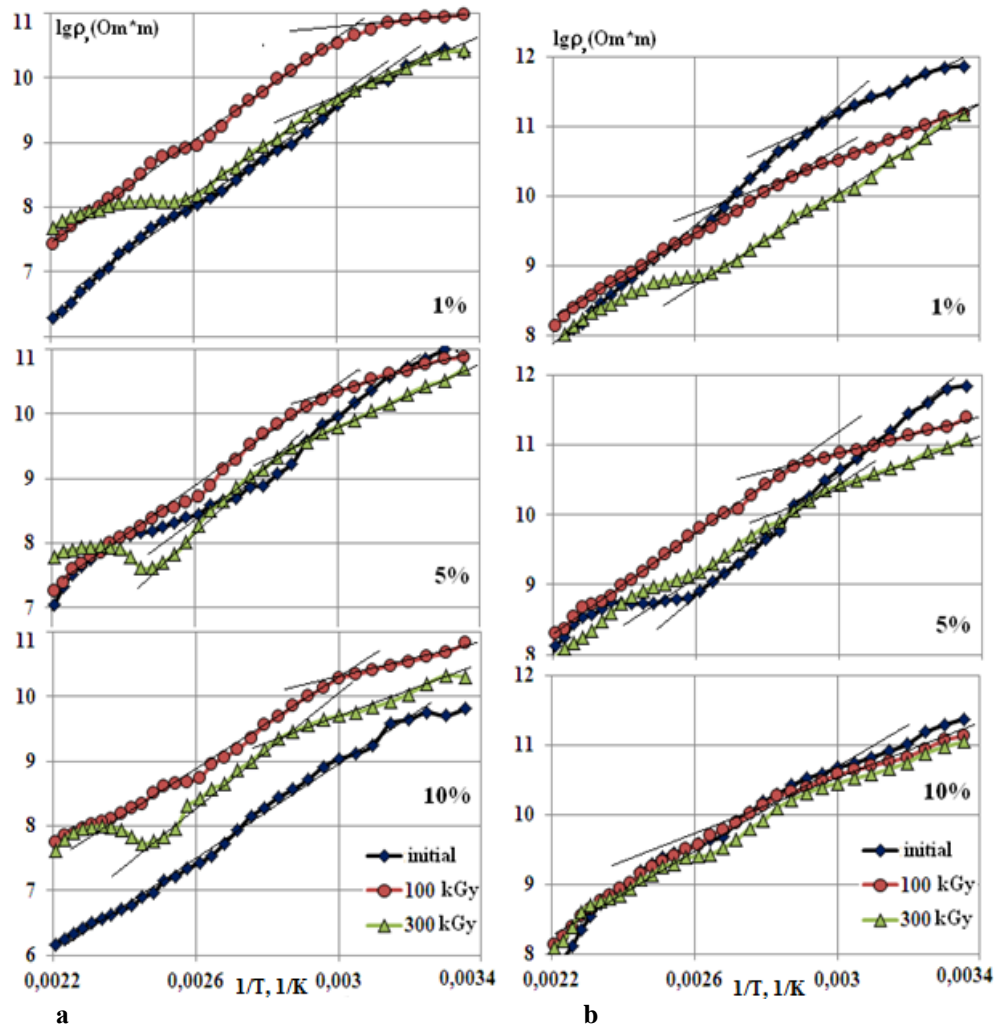


Fig.2. Temperature dependences of specific volume resistance of P(VDF-TFE) composites with micro-Si (a) and nano-Si (b) irradiated by different doses.

Table

The activation energy value of electric conduction of P(VDF-TFE) and P(VDF-TFE)/Si composites with micro- and nano-particles irradiated by different doses.

	Dose, KGy	Micro-Si		Nano-Si	
		ΔE_1 , eV	ΔE_2 , eV	ΔE_1 , eV	ΔE_2 , eV
100% P(VDF-TFE)	0	-	0,33	-	0,33
	100	-	0,298	-	0,298
	300	-	0,27	-	0,27
1%	0	-	0,36	0,2	0,387
	100	0,036	0,31	0,17	0,26
	300	0,15	0,324	-	0,258
5%	0	-	0,31	-	0,39
	100	0,13	0,33	0,1	0,31
	300	0,21	0,42	0,15	0,29
10%	0	-	0,32	0,18	0,25
	100	0,113	0,298	0,18	0,25
	300	0,165	0,36	0,18	0,25

We suppose that radicals and matrix oxidation appearing as a result of gamma radiation influence can lead to formation of oxygen bonds C-O-Si with filler surface in composite. Thus, the release of charges bound with surface of silicon particles becomes difficult in region below composite melting point because of relatively strong interaction and changes take place because of charges released from polymer matrix.

The some resistance stabilization region is observed only in samples irradiated by dose 300KGy in $\lg \rho = f(1/T)$ temperature dependences of P(VDF-TFE)/Si composites with silicon nano-particles (fig.2b). On the base of comparative analysis of these dependences one can say that radiation exposure up to dose 300KGy is accompanied by cross-linking in polymer matrix and increase of interphase layer interaction with oxidized active surface of nano-silicon filler in distinct from composites with micro-silicon filler. From temperature dependence of initial and irradiated composites with 10% silicon volume content it is seen that all three curves coincide with each other with some error. Using $\lg \rho_v = f(1/T)$ the activation energy values ΔE corresponding to each inclination of rectilinear part of curves are calculated. The observable curve step and comparison of ΔE activation energy values from table show that composites

with (10% volume content) nano-silicon are relatively stable to gamma irradiation exposure. The redistribution of radiation energy on volume takes place in P(VDF-TFE)/10%Si composites with nano-particles, energy part influencing on polymer matrix interface with nano-particles increases that leads to stable character of sample conductivity. Thus, at one and the same filler content the particle concentration in composites with nano-particles has the relatively high value. The transition from micro-particles to nano-particles is accompanied by increase of filler effective surface and concentrations of C-O-Si bonds with surface and this leads to mobility decrease and resistance increase that we experimentally observe. At introduction of micro-fillers the concentration of C-O-Si bonds becomes relatively low because of effective surface decrease, macro-molecule mobility increases and resistance decreases correspondingly that reflects on activation energy values [16]. In conclusion we can say that observable changes in electric properties of irradiated composites on P(VDF-TFE) base with micro- and nano-particles of silicon are connected by both processes of radical formation and oxidation with further cross-linking and destruction in heterogeneous system (polymer matrix and filler) and redistribution of absorbed radiation energy between components of composite.

- [1] P. Thomasa, S. Satapathy, K.Dwarakanath, K.B.R. Varma. Dielectric properties of Poly(vinylidene fluoride)/ CaCu₃Ti₄O₁₂ nanocrystal composite thick films, eXPRESS Polymer Letters Vol.4, No.10, 2010, pp.632-643.
- [2] S.N. Tkachenko, O.S. Qefle, S.M. Lebedev. Issledovanie svoystv polivinilidenftroida, modifichirovannoqo nanochastichami nikelya. Plasticheskie massi, №2, 2008, s.28-32. (In Russian).
- [3] Javier Arranz-Andres, Nuria Pulido-Gonzalez, Pilar Marin, Ana M. Aragon, Maria. L. Cerrada. Electromagnetic shielding features in lightweight pvdf-aluminum based nanocomposites, Progress In Electromagnetics Research B, 2013, Vol. 48, 175-196.
- [4] A.M. Magerramov, M.A. Nuriyev, I.A. Veliev, S.I. Safarova. Coronolectrets Based on Polypropylene Composites Dispersed by a TlIn_xCe_(1-x)Se₂ Semiconductor Filler, Surface Engineering and Applied Electrochemistry, 2010, Vol. 46, No. 2, pp. 169-172.
- [5] Houda Rekik, Zied Ghallabi, Isabelle Royaud, Mourad Arous, Gérard Seytre, Gisèle Boiteux, Ali Kallel. Dielectric relaxation behaviour in semi-crystalline polyvinylidene fluoride (PVDF)/TiO₂ nanocomposites, Composites: Part B 45, (2013), p. 1199-1206.
- [6] A.V. Suxinina. Razrabotka radiachionno-sshivaemix napolnennix kompozichiy na osnove sevilena dlya kabelnix termousajivaemix izdelyi. Avtoreferat dissertachii na soiskanie uchenoy stepeni kandidata fiziko-matemoticheskix nauk, 2009, 19 str. (In Russian).
- [7] Zelimir Jelcic, Franjo Ranogajec. High impact polystyrene modified by ionizing γ -radiation, POLIMERI, 31, (2010) 2, p.52-58.

- [8] S.A. Xatipov, E.M. Konova, N.A. Artamonov. Ros.khim.j. (J. Ros. khim. ob-va im. D.I. Mendeleeva), 2008, t. LII, № 5, s.64-72. (In Russian).
- [9] A.M. Magerramov, M.A. Nuriyev, F.I. Akhmedov, and I.M. Ismailov. Radiothermoluminescence of g-Irradiated Composites of Polypropylene and Dispersed Oxides, Surface Engineering and Applied Electrochemistry, 2009, Vol. 45, No. 5, pp. 437–440.
- [10] K.K. Ametov, B. Kaipov, S.M. Joldasova, A.Q. Lavrushko, N.M. Qalashina. Elektroprovodnost polimernix kompozitov na osnove polipropilena I kremniya, Preprint № R-9-308, 1987, 10s. (In Russian).
- [11] V.I. Fistul. FTP, 1993, tom 27, vip.11/12, s.1788-1794. (In Russian).
- [12] V.M. Morilova. Issledovanie karbonizachii polivinilidenftroida metodami emissionnoy I absorbtionnoy spektroskopii. Avtoreferat dissertachii na soiskanie uchenoy stepeni kandidata fiziko – matematicheskix nauk, 2014, 23 str. (In Russian).
- [13] T.S. Sapojnikov, A.A. Mirzoev. FTT, 2008, tom 50, vip.6, s.1143-1145. (In Russian).
- [14] A.P. Tyutnev, A.V. Vannikov, Q.S. Minqaleev, V.S. Senko. Elektricheskie yavleniya pri obluchenii polimerov. M. Energoatomizdat, 1985, 176 s. (In Russian).
- [15] L.N. Ignateva, V.Q. Kuryaviy, T.A. Kaydalova, V.M. Buznik, A.I. Korchagin. Jurnal Strukturnoy Ximii, 2005, Tom 46, № 5, s. 879 – 886. (In Russian).
- [16] D.V. Alyavdin, A.P. Klestov, A.A. Shestakov. Fazovie perexodi, uporyadochennye sostayaniya I novye materialy, 2012, №11, s.1-5. (In Russian).

Received: 14.01.2015

CONTENTS

1.	Influence of high pressures on electrical and thermoelectric properties of Cu-Ge-As-Se glasses N.V. Melnikova, A.Yu. Mollaev, O.L. Kheifets, L.A. Saypulaeva, P.P. Hohlachev, A.G. Alibekov, A.L. Filippov, A.N. Babushkin, K.V. Kurochka	3
2.	Temperature dependences of electric conduction and thermo-emf in CuFeS_2 and $(\text{CuFeS}_2)_{0.7}(\text{CuGaS}_2)_{0.3}$ solid solutions S.S. Ragimov, S.G. Asadullayeva, T. Sh. Ibragimova, K.O. Tagiyev	9
3.	<i>Leu</i> -gallatostatine-3 neuropeptide spatial structure L.I. Veliyeva, E.Z. Aliyev	12
4.	Higgs boson decay channels $H \rightarrow \gamma\gamma$, $H \rightarrow \gamma Z$, $H \rightarrow gg$ S.Q. Abdullayev, M.S. Gojayev, F.A. Saddigh	17
5.	Phase transition in ferromagnetic superlattice nanowires V.A. Tanriverdiyev, V.S. Tagiyev	23
6.	Electro-optic characteristics of liquid crystalline mixture H-37 doped by ferroelectric particles T.D. Ibragimov, A.R. Imamaliyev, G.M. Bayramov	27
7.	Trapping of classical particles by a potential well deepening with time Azad Ch. Izmailov	32
8.	Investigation of YAG:Ce luminescence properties and manipulation of phosphor converted white LED's color characteristics T.Y. Orujov, S.A. Mammadova, S.H. Abdullayeva, N.N. Musayeva, R.B. Jabbarov	36
9.	The influence of gamma irradiation on electric properties of polyvinylidene fluoride composites with silicon A.M. Magerramov, I.M. Nuruyev, R.N. Mehdiyeva, M.A. Nuriyev	43



www.physics.gov.az